PHOTOPRODUCTION OF CHARGED PION PAIRS FROM HYDROGEN AT PHOTON ENERGIES BETWEEN 800 AND 1500 MeV

Thesis by
Wesley Loren Shanks

In Partial Fulfillment of the Requirements
For the Degree of
Doctor of Philosophy

California Institute of Technology
Pasadena, California
1968
(Submitted August 25, 1967)

ACKNOWLEDGMENTS

This experiment was the result of a tremendous effort by many people at the Synchrotron Laboratory. The immediate experimental group consisted of Dr. James van Putten, Dr. Joe Mullins, Dr. Hans Kobrak, and Alan Moline, all of whom devoted a large amount of time and effort throughout the experiment. The cooperation of Dr. Eric Adleberger during the initial phases of the experiment is also appreciated.

The efforts of the technical crew are also acknowledged, with special thanks to Earl Emery and Dick Wileman. The success of the scanning and measuring operation is in large part due to the efforts of Mrs. Alan Moline and her helpfulness is greatly appreciated. Also the programming assistance of Robert Piccioni and Phyllis Nillson helped immeasurably.

The advice and counsel of my advisor, Dr. James van Putten, were invaluable and the experience of working with him has been very rewarding. Also the financial support of the California Institute of Technology is gratefully acknowledged.

The limitless patience and perseverence of my wife, Yvette, cannot be duly acknowledged. Her effort and sacrifice shall never be forgotten.

ABSTRACT

The reaction $\gamma + p \quad p + \pi^+ + \pi^-$ has been studied for photon energies between 800 and 1500 MeV and for dipion masses between 510 and 900 MeV. The bremsstrahlung beam from the Caltech synchrotron was passed through a liquid hydrogen target and spark chambers were used to detect the three final particles. In addition, the proton energy was determined by a range measurement. Approximately 40,000 photographs were taken, yielding 3018 acceptable events. The results were fit to an incoherent combination of the N*(1238) resonance, the ρ^o (750) resonance, and three-body phase space, with various models being tried for ρ^o production. The total cross section for ρ^o production is consistent with previous experiments. However, the angular dependence of the cross section is slightly more peaked in the forward direction, and the ratio of ρ^o production to phase space production is larger than previously observed.

However, since this experiment was only sensitive to the production angles $\cos\theta_{cm} \geq .75$, statistical fluctuations and/or an anisotropic distribution of background production have a severe influence on the ρ^o to background ratio. Of the ρ^o models tested, the results prefer ρ^o production by the one pion exchange mechanism with a very steep form factor dependence. The values of the mass and width of the ρ^o found here are consistent with previous experiments.

TABLE OF CONTENTS

LIST OF FIGURES

LIST OF TABLES

To Yvette

I. INTRODUCTION

The first observation of the reaction

$$\gamma + p \rightarrow p + \pi^+ + \pi^-$$

was made in 1954 by Peterson and Henry(1) using nuclear emulsions. Since then, many investigations of this reaction have been performed(2-23), with the more recent experiments naturally providing the most interesting answers to theoretical models. This thesis describes an investigation of the above reaction in the interval $800 < k < 1500$ MeV and $500 < m_{\pi\pi} < 900$ MeV, utilizing spark chambers and counter telescopes to detect the three outgoing particles.

Early experiments at photon energies below 700 MeV(2-5) indicated that the π^- tended to be produced with low kinetic energy. This was consistent with the model of Cutkosky and Zachariasen(24) who assumed a strong P wave interaction between one pion and the photon, S wave production of the other pion, and no π-π final state interaction. A subsequent experiment by Sellen et al(9) using a hydrogen diffusion chamber provided information over a larger range of angles. They found that at energies of $k < 700$ MeV there was a significant amount of $N^*(1238)^{++}$ production in agreement with the model of Cutkosky and Zachariasen.

The discovery of the ρ (750) dipion resonance(25) in the reactions

$$\pi^- + p \rightarrow p + \pi^- + \pi^0$$

$$\pi^- + p \rightarrow n + \pi^+ + \pi^-$$

naturally prompted a search for its existence in photoproduction. McLeod, Richert, and Silverman found that the ρ^0 resonance was indeed present in photoproduction but at a somewhat lower mass than that observed in production by pions. Del Fabbro et al(14,15) also found an indication of another π-π resonance at $m_{\pi\pi} = 380$ (the σ^0 meson) which had been previously suggested by Samios et al(13) on the basis of observations of $\pi^- p$ interactions.

More extensive experiments(17-23) have recently been completed to investigate various models of the production of these mesons and the N* isobar. The only information on σ^0 production comes from the data of Fretwell and Mullins(20) which give a slight indication of σ^0 production at low energies. However, all groups seem to agree reasonably on the N* production cross section, and find that the Drell (OPE) model(26) gives the correct angular distributions but gives a total cross section which is too small by a factor of 2-3. To explain this discrepancy, Stichel and Scholz(27) have calculated N* production in a gauge invariant manner and find agreement with the total cross-section measurements. In addition, CEA and DESY groups find that the decay distribution of the N* agrees with the calculations of Stichel and Scholz and not with the Drell model. On the other hand, all experiments, especially Hauser's, indicate that the Stichel-Scholz model gives a very bad fit to the angular dependence of the differential cross section. So as yet there is no entirely consistent model of N* production.

Production of the ρ^o (750) increasingly dominates this reaction at higher energies and several theoretical models are available for comparison. The OPE model for ρ^o production(28-30) gives a total cross section which decreases much too rapidly above 1.5 BeV and whose angular dependence is not as peaked in the forward direction as the results indicate. Several authors(31-33) have included vertex form factors or the effects of final state interactions in the OPE model and find that both the angular and energy dependence of the cross section are in reasonable agreement with the data if one inserts very steep form factors or if a large amount of absorption of the low partial waves is used. The diffraction model(34, 35) gives a slightly better agreement with existing results than the OPE absorption model, but the diffraction mechanism is only claimed to be applicable at higher energies (above 2 BeV) and at small angles.

This experiment was designed to avoid most of the N* production, so as to enhance the influence of ρ^o production in the final events. In particular it was hoped to provide information about the ρ^o resonance mass and the production mechanism.

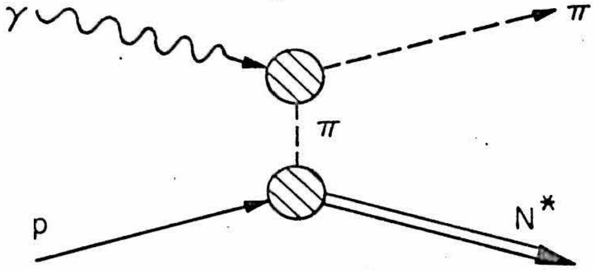

Drell model for N* production

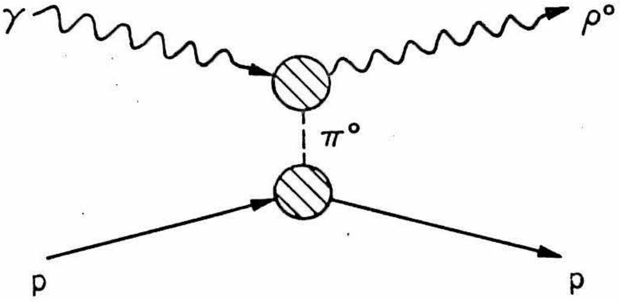

OPE model for ρ° production

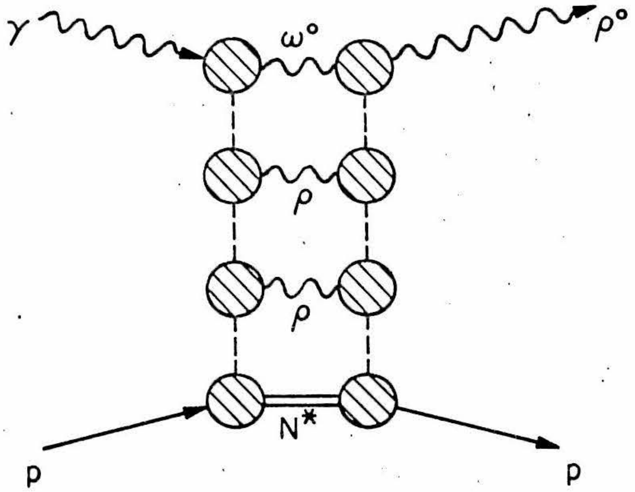

Diffraction model for ρ° production

Figure 1

II. EXPERIMENTAL METHOD

A. General Description

Previous results on the reaction $\gamma + p \rightarrow p + \pi^+ + \pi^-$ involved the use of either bubble chambers or magnetic spectrometers. The use of a bubble chamber has the disadvantage that no selective triggering is available, so to get reasonable statistics on this reaction one would have to take many more pictures than we were prepared to process. The use of magnetic spectrometers has exactly the opposite restriction. They provide very good selective triggering, but their use in this experiment would have made the data collection extremely lengthy. The experiment described here used sets of counters to detect the three outgoing particles, thin plate spark chambers to determine the particle directions, and a counter-spark chamber telescope to identify the proton and measure its energy (see Figure 2). Three separate runs were made with the central angle of the proton telescope at 24°, 20°, and 17°. The spark chambers were arranged in such a way as to avoid most of the N* (1238) production and thus hopefully to enhance the contribution of the ρ^0 (750) resonance in the results.

The kinematics of the reaction $\gamma + p \rightarrow p + \pi^+ + \pi^-$ are completely determined if one knows the angles of the three final particles, provided they have been identified correctly. In this experiment, however, the multiple scattering of the particles very often could make the kinematics completely meaningless in the sense that a solution for the proton energy would not exist

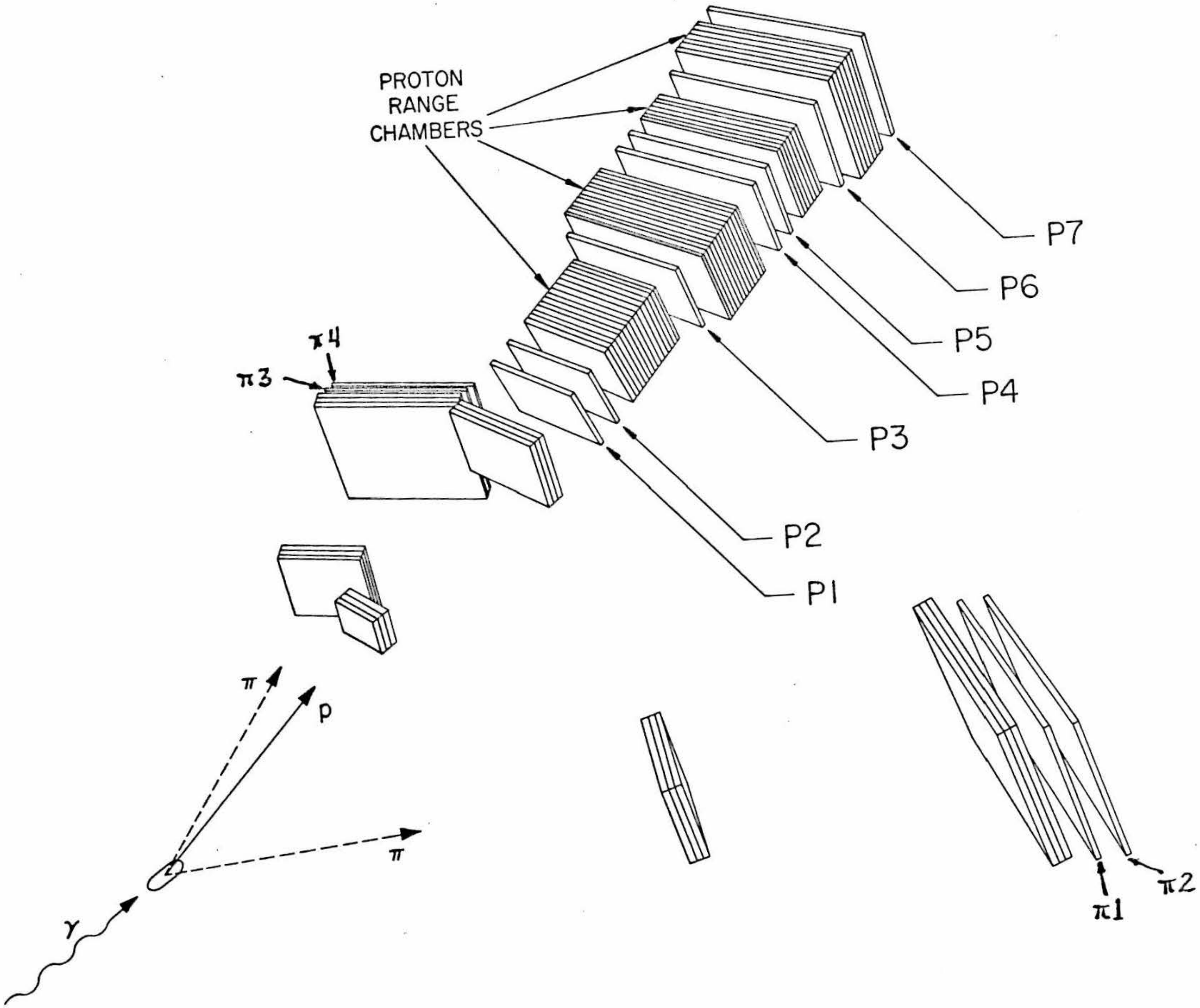

Figure 2

given the measured angles, and even when such a solution did exist, the errors involved would be huge. This was true despite the efforts to keep multiple scattering at a minimum. So the necessity of an overdetermination of the kinematics was compelling, not only to solve the kinematic problem, but also to reject background events. This overdetermination was provided by a measurement of the proton range in thick plate spark chambers.

Figure 2 shows the arrangement of the counters and spark chambers. The chambers were triggered on a coincidence between a charged particle from each telescope and the satisfaction of certain requirements on the pulses on the proton telescope. Figure 3 shows the triggering logic in more detail. The pion requirement was a simple fourfold coincidence ($C\pi$) between the two pairs of pion counters. The proton requirements depended on where the particle stopped. $C\pi 1$ was satisfied if the particle stopped before counter P4, and $C\pi 2$ was satisfied if it went at least into counter P5. For the $C\pi 2$ events, the chambers were triggered if the signal from P4 was merely greater than minimum ionizing, so for this type of event almost any particle could satisfy the requirements of the proton logic. As the analysis produced very few acceptable events in that range, this difficulty has no effect on the final results. For $C\pi 1$ events, the logic was divided into two parts depending on the pulse height in counter P2. If the pulse from P2 was large enough to look like a proton which stopped before P3, a discriminator (D1) was tripped and an "LD1" trigger was produced. If the pulse from P2 was not large enough to trigger D1, then it was allowed to satisfy a lower discrimination

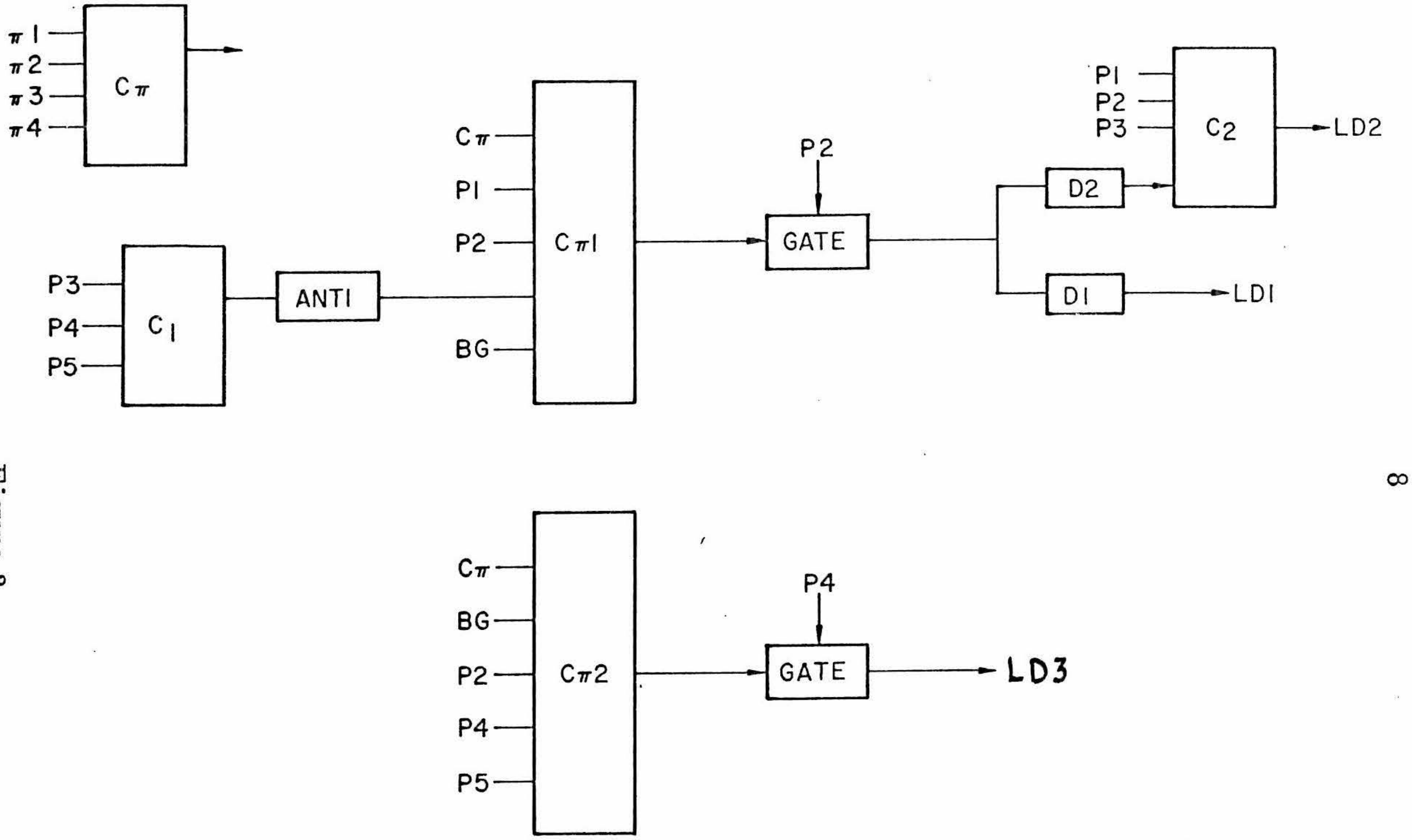

TRIGGERING LOGIC

Figure 3

(D2) if the particle had gone through counter P3. This produced an "LD2" trigger.

The heavy plate chambers shown in Figure 2 provided a measurement of the proton range. In addition, for an LD1 or LD2 trigger, the pulses from proton counters P1 and P2 were displayed on a dual beam oscilloscope, and for an LD3 trigger the pulse from counter P4 was displayed. A photograph of these pulses was used as part of the analysis of an event (see Appendices IB and IIA). The range of the particle in the heavy plate chambers was correlated with these pulse heights to provide a reliable rejection of pions entering the proton telescope. The discriminators D1 and D2 described above prevented the vast majority of pions from triggering the proton telescope logic, and the correlation of range and pulse height rejected essentially all those which managed to circumvent the triggering logic (see Appendix IB).

A 4' x 8' mirror suspended 10' above the apparatus reflected the image of the entire spark chamber arrangement to a camera located over the rear of the proton telescope. Figure 4 shows a view of the experiment looking at the main mirror from the camera position. A large tent was constructed over the apparatus, and a photograph of the spark chambers was taken every time the logic was triggered. A typical such frame is shown in Figure 5. A 45° mirror attached to each spark chamber was used to determine the depth of tracks in that chamber. A system of fiducials, some scribed on lucite plates over the chambers and others mounted on cement shielding blocks, was used to determine spark positions given the measurements of spark and fiducial images on the film (see Appendix IV). The accurate measurement of these fiducials

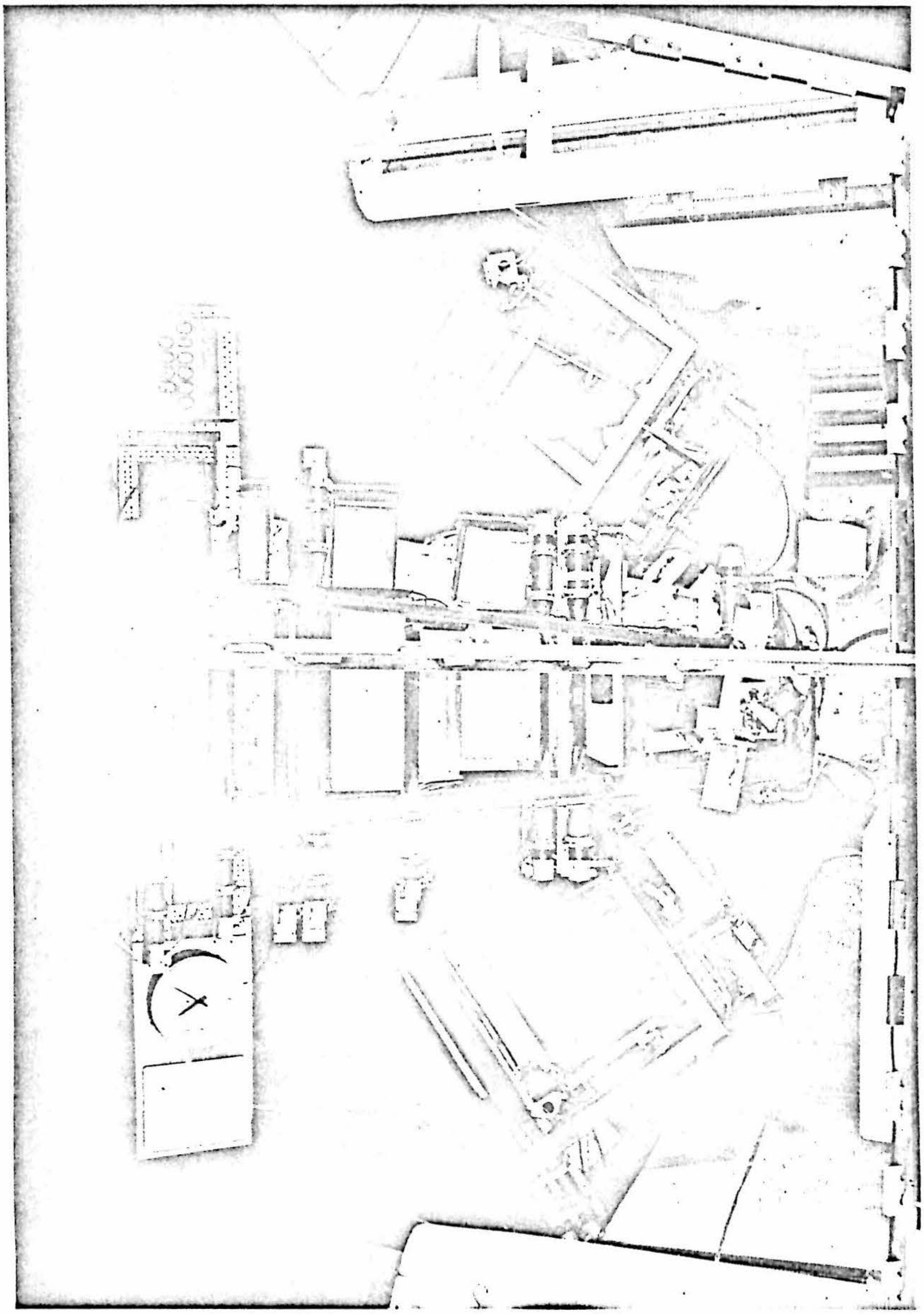

Figure 4

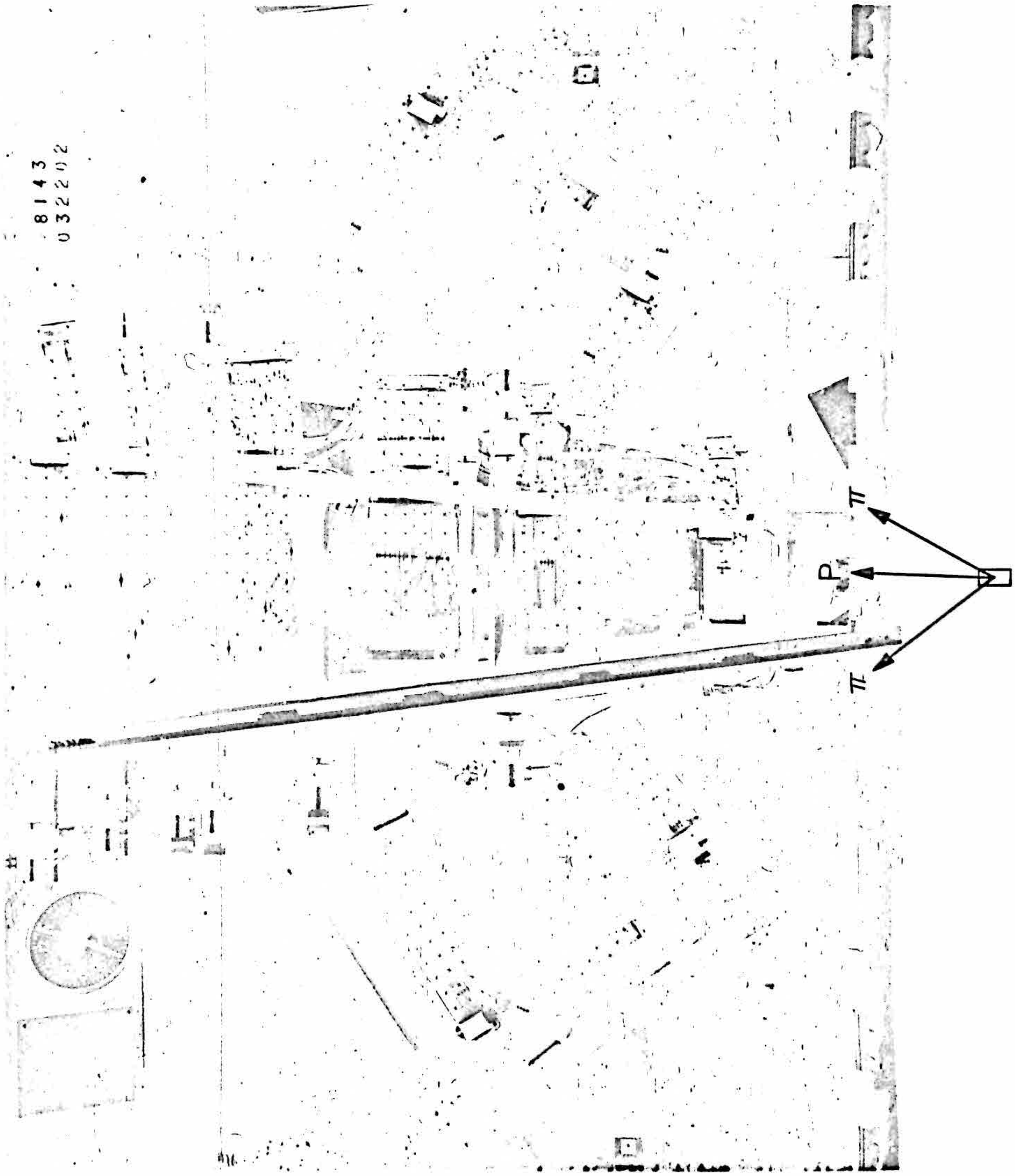

Figure 5

was an important part of this experiment and is described in detail in Appendix IV. Finally, a set of "logic lights" was displayed on each frame to indicate which section of the logic was responsible for triggering the event.

B. Beam Arrangement

The layout of the apparatus in the beam area is shown in Figure 6. The west beam from the synchrotron was passed through the various collimators and scrapers shown, and charged particles produced before the final scraper were eliminated by the sweep magnet. The beam diameter was approximately 1.6 cm at the hydrogen target and 3 cm at the beam catcher. The hydrogen target was 5 cm in diameter and 11.5 cm long and was centered accurately on the beam line. The direction of the beam was monitored during the experiment by photographing the shadow of a tungsten wire cross placed about 8 meters upstream from a film holder. The position of the wire cross and the image on the film were measured with respect to the other fiducials described above, so the incident photon direction is accurately known in our fiducial system.

The beam intensity was monitored by two independent methods. First, the output of a Wilson quantameter was integrated over the desired time to indicate the total beam energy during a run. Second, a counter telescope consisting of two scintillators was mounted 6' below the hydrogen target. The monitor counters were in a well shielded lead enclosure with an opening towards the target, so that essentially all the counts came from the target.

Figure 6

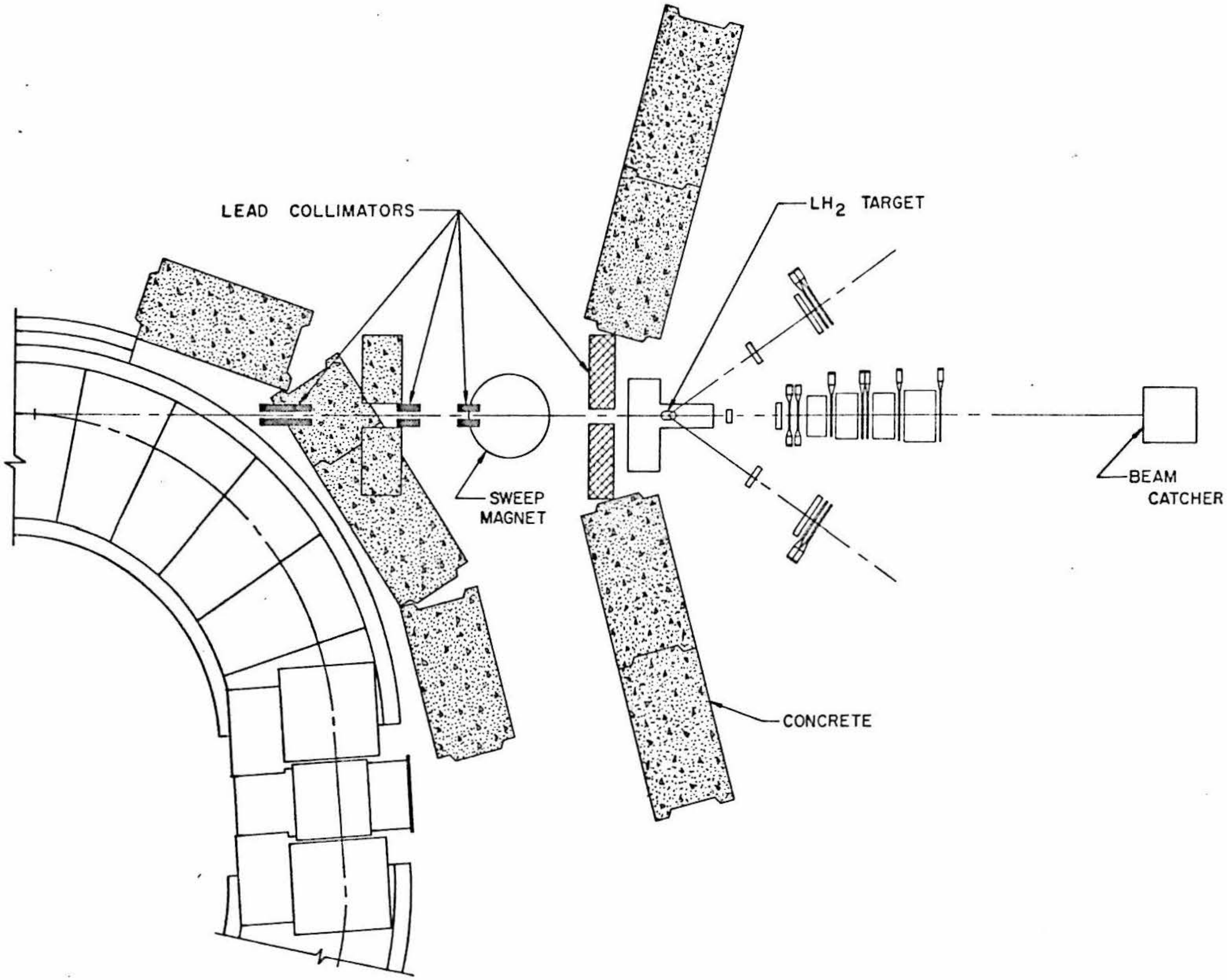

EXPERIMENTAL AREA

The gains of the monitor counters were kept constant (see Appendix IB) and the ratio of monitor counts to the quantameter output is shown in Figure 7. The slope of the monitors/BIP as a function of time is due to the fact that the quantameter had a slow leak. The quantameter calibration of October 1964 done during the experiment preceding outs$^{(36)}$ showed that the west quantameter calibration was .98 of the south quantameter, and also that the calibration was decreasing by approximately .01/month. The calibration of May 1966 performed by Rochester and Bloom$^{(37)}$ showed that the west/south calibration ratio was .78. Also, an experiment which ran from November 1964 to May 1965$^{(38)}$ suggested a 1%/month change in the quantameter. The difference between the October 1964 and the May 1966 calibrations gives an average change of 1.1%/month, which agrees with the rate of chance over shorter intervals. Therefore, it is assumed that the quantameter calibration was changing linearly. The normal west quantameter calibration is

$$Q = 1.06 \times 10^{13} \text{ MeV/BIP} .$$

The effective calibration used below was assumed to be Q/.86 at the beginning and Q/.84 at the end of our experiment.

Finally, to assist in determining the non target-associated background contamination, intermittent runs were made with the hydrogen target empty. The triggering rate was 7.5% of the normal triggering rate. This is consistent with the expected production of events from other material in the beam. The final analysis of the target empty runs produced ten acceptable events and was consistent with production from the residual gaseous hydrogen, so there is

Figure 7

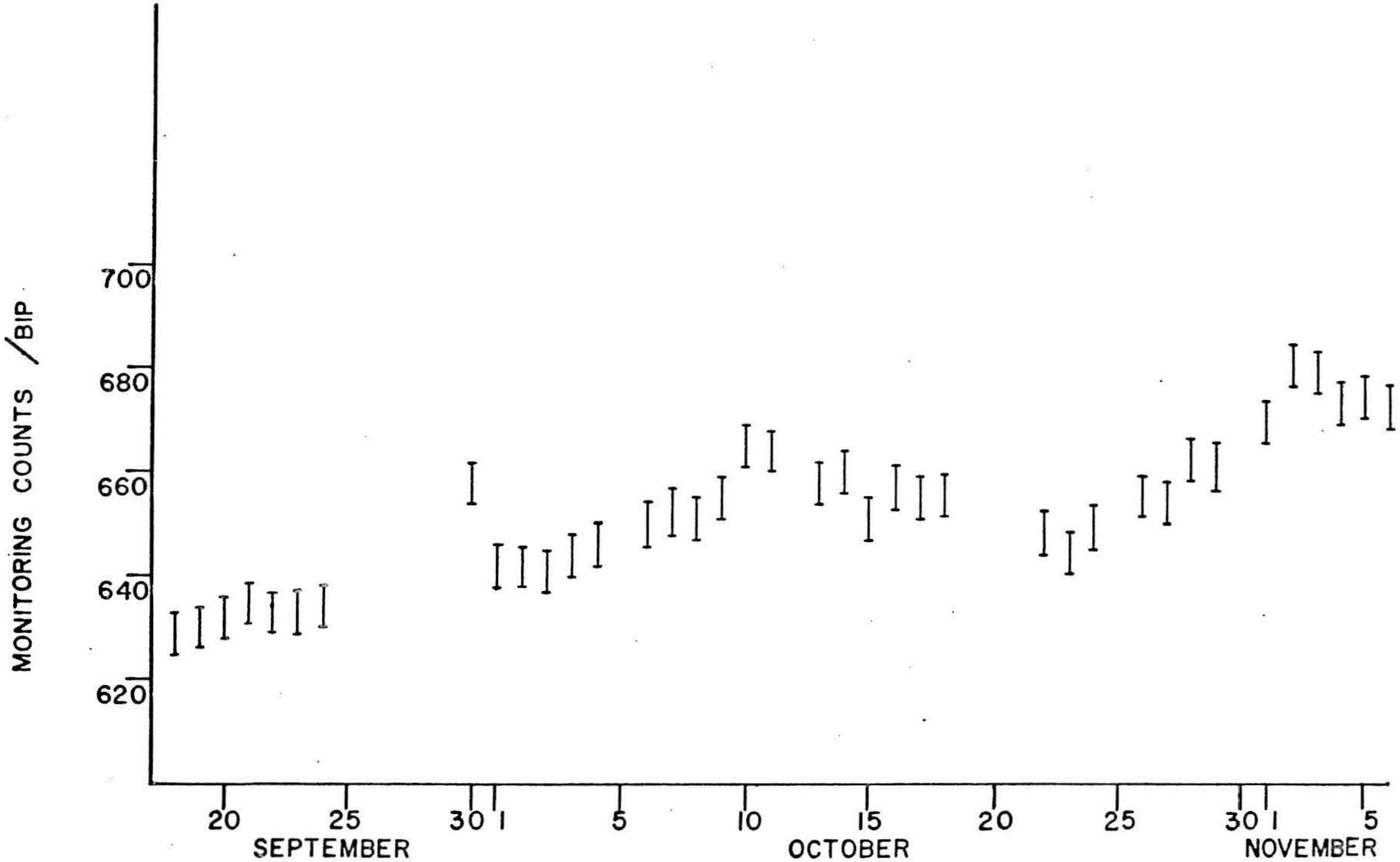

BEAM MONITORING

essentially no correction to the results from events originating on the surface of the target.

III. GENERAL SCANNING AND MEASURING OF FILM

The handling of the oscilloscope and spark chamber film started with the classification and measurement of the oscilloscope pulses. The scope pulse information served two main purposes. (The details of the procedure used to gather the information are in Appendix II). The first was to furnish pulse-height information used in final computer analysis. This was used as a consistency check against the measured proton range, or if there was no track in the range chamber, these pulses were used to determine the proton energy (see Appendix III). The second was to provide a requirement on the proton range called MINSTOP, used in the preliminary scanning of the spark chamber film to avoid measuring events in which the proton telescope logic was triggered by a pion. (See Appendix IIA). (MINSTOP was the minimum proton range which could be associated with the measured scope pulses for an event).

The purpose of the preliminary spark chamber film scanning (see Figure 8) was to save time in the film handling. Since the measurement of an event took 10-13 minutes and the preliminary scanning of an event required only three minutes, the preliminary scanning was used to classify an event as either good, questionable or bad (refer to Appendix II.B for the detailed procedures). The results of the scanning yielded 30% good, 10% questionable, and 60% bad. All of the good events and half of the questionable ones were measured. If a measurement of a frame contained any errors attributable to the measurer, it was slated for remeasurement - until a valid measurement of that event was

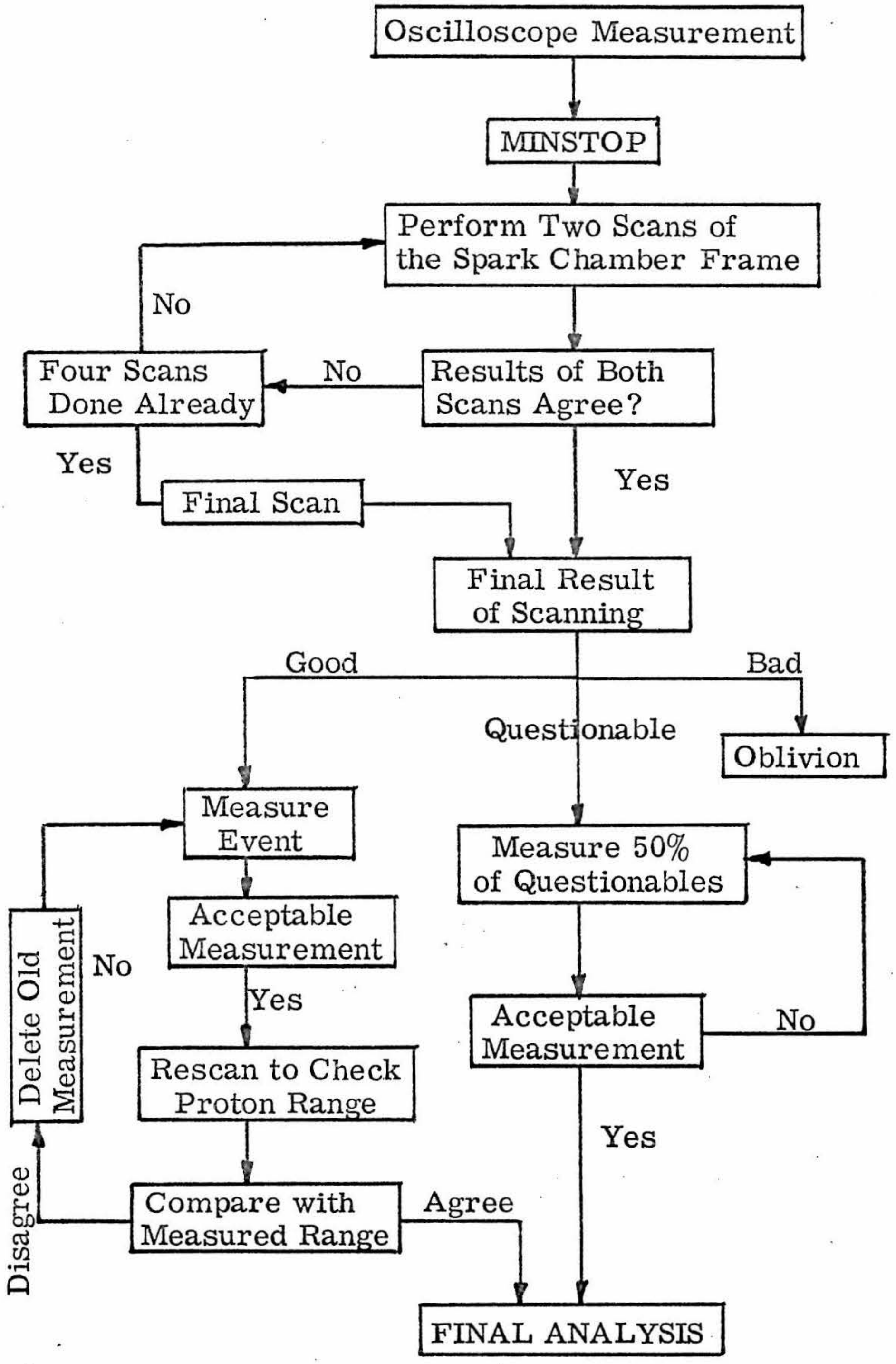
Oscilloscope Measurement
MINSTOP
Perform Two Scans of the Spark Chamber Frame
No
Four Scans Done Already
No
Results of Both Scans Agree?
Yes
Final Scan
Yes
Final Result of Scanning
Good
Bad
Questionable
Oblivion
Measure Event
Measure 50% of Questionables
Delete Old Measurement
No
Acceptable Measurement
Yes
Acceptable Measurement
No
Rescan to Check Proton Range
Yes
Compare with Measured Range
Agree
Disagree
FINAL ANALYSIS

Figure 8

obtained. For every good event, an additional scan of the heavy chambers was done, and its results compared with the measurement of that event. When there was a disagreement, the old measurement was discarded and a new measurement performed. The reason for the additional scan of the heavy chambers is that scanners sometimes missed short proton range tracks. Gradually, all the desired events to be run through the final computer analysis were accumulated on magnetic tapes.

IV. ANALYSIS OF MEASURED EVENTS

As stated in the previous section, all of the GOOD and half of the QUESTIONABLE events were measured on digitized measuring machines. The checks on a measurement of an event are discussed in Appendix II. C, and the process of determining the space location of sparks from their film measurements is discussed in Appendix IV.

The analysis can be considered in two sections. First, events were run through a program which weeded out the ones with gross deficiencies. This program then punched cards indicating whether or not an event was accepted and containing the final results for the acceptable events. Second, the cards containing the results from acceptable events were screened by looking at various indicators of the quality of an event and imposing predetermined standards of acceptability. In this way, one could readily see the influence of changing these standards without involving the large amount of computer time required for the first part of the analysis.

Figure 9 shows the flow diagram for the first part of the analysis described above. After an event was read and its sparks reconstructed, a track candidate was chosen from each particle telescope and the following requirements were imposed. 1) For each of the three telescopes, a single straight line was fit through its sparks in the thin plate chambers. If the spark farthest from this line was more than 5 mm off, then it was deleted and a new line was fit through the remaining sparks. Then if any chamber had only one remaining spark, the event was rejected. (For

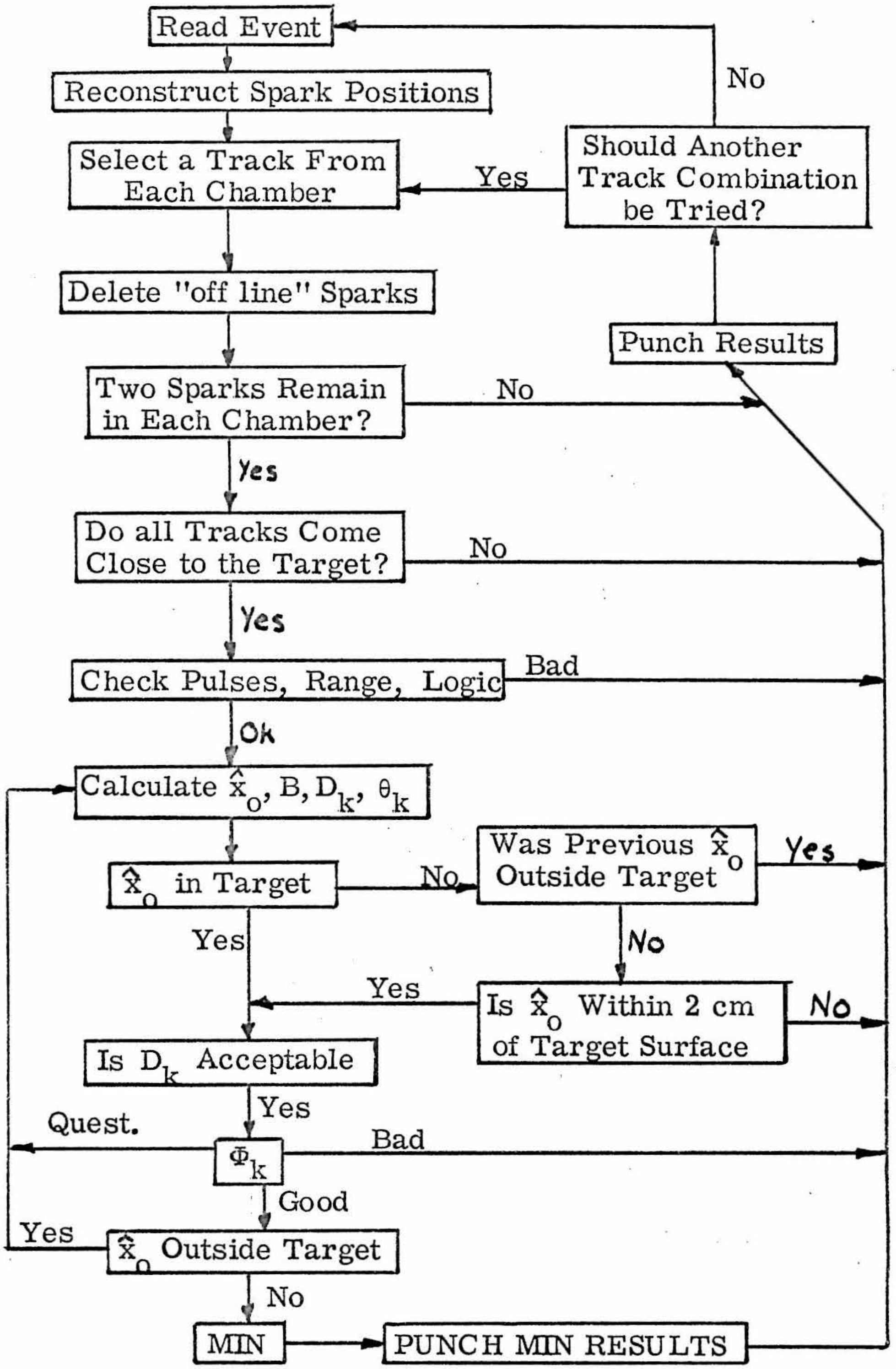
Read Event
Reconstruct Spark Positions
Select a Track From Each Chamber
Yes
Should Another Track Combination be Tried?
No
Delete "off line" Sparks
Punch Results
Two Sparks Remain in Each Chamber?
No
Yes
Do all Tracks Come Close to the Target?
No
Yes
Check Pulses, Range, Logic
Bad
Ok
Calculate $\hat{x}_o$, B, D_k, θ_k
Was Previous $\hat{x}_o$ Outside Target
Yes
$\hat{x}_o$ in Target
No
Yes
No
Yes
Is $\hat{x}_o$ Within 2 cm of Target Surface
No
Is D_k Acceptable
Yes
Quest.
Φ_k
Bad
Good
Yes
$\hat{x}_o$ Outside Target
No
MIN
PUNCH MIN RESULTS

Figure 9

questionable events this was not required.) 2) Using the three final straight lines defined above, the closest approach of each line to the center of the target was calculated. If any line missed by more than 10 cm, the event was rejected. 3) The compatibility of the measured scope pulses, the proton range, and the logic light configuration was tested. First, the measured range track (if any) had to line up with a line fit through the proton thin chamber sparks. If this alignment was bad, the range track was ignored and the event was treated under the hypothesis that the proton stopped in counter P2. Next, the logic light information had to agree with the proton range. Finally, the pulses from counter P1 and P2 had to be larger than the limits shown in Figure 14 to reject most of the pions (see Appendix I. B. 7 for further discussion). 4) An origin of the event ($\hat{x}_o$) was calculated, and if it was more than 2 cm outside the surface of the target, the event was rejected. If the origin was less than 2 cm from the target surface but yet not in the target, the event was processed further, and a later calculation of the origin was done with slightly adjusted angles. If the origin remained outside the target, the event was rejected. The distribution of the origins of events rejected for being outside the target was essentially uniform, except for a small clustering near the front surface of the target. This clustering can be explained almost exactly by production from the protons in the mylar surface and by the expected loss of events due to our resolution in $\hat{x}_o$. 5) Given the three straight lines from requirement 1) above, the closest approach, D_k, of each line to the origin ($\hat{x}_o$) was calculated. The pion tracks had to come within 1.5 cm and the proton track had to come within 2 cm of $\hat{x}_o$. The quantity D_k is the square of this distance. 6) Having a first approximation for the particle angles and the proton energy, a fit was made to the overdetermined kinematics. The kinematic constraint equation was

$$G\text{ (particle angles, proton energy)} = 0.$$

The particle angles and proton energy were then adjusted proportionally to their respective errors (multiple scattering on the angles and range straggling on the proton energy) until solution to the constraint equation was found. 7) A function Φ_k was calculated for each telescope to indicate the "goodness of fit". This function Φ_k was the logarithm of the probability that the particle could have been produced at $\hat{x}_o$ with the assumed initial angles and have had its sparks measured as they were (see Appendix III.A). If any of the three Φ's were bad, the event was rejected. The limit imposed here was extremely liberal in that less than 1/4% of all good events would be rejected. Also, the events which were rejected solely because of a bad Φ_k were examined to see if a slight extension of the limit would allow these events to be accepted. Such was not the case. If the event satisfied all the requirements above, it was sent to a subroutine called MIN(39) which calculated the best fit to the event in the following sense. An overall function F was concocted to describe the fit between the measured sparks and proton range on the one hand, and an assumed set of angles, proton energy, and origin on the other. Mathematically, this is

$$F(\theta_1, \theta_2, \theta_3, \phi_1, \phi_2, \phi_3, T_p, \hat{x}_o) = \sum_{k=1}^{3} \Phi_k(\theta_k, \phi_k, \hat{x}_o) + \frac{1}{2}\left(\frac{T_p - T_m}{\Delta_m}\right)^2$$

subject to the constraint equation

$$G(\theta_1, \theta_2, \theta_3, \phi_1, \phi_2, \phi_3, T_p) = 0$$

where

$$k = \begin{cases} 1 \text{ east pion} \\ 2 \text{ west pion} \\ 3 \text{ proton} \end{cases}$$

θ_k, ϕ_k are the angles of particle k

T_p is the proton energy

T_m is the measured proton energy

Δ_m is the expected r. m. s. error in T_m

$\hat{x}_o$ is the origin of the event .

The subroutine MIN found the set of $\theta_k, \phi_k, T_p,$ and $\hat{x}_o$ which minimized F, and this final set of variables was used to calculate all other quantities such as the photon energy, dipion mass, etc.

If there were other candidates measured in the various chambers, every combination of one track candidate from each chamber was sent through the program to determine which combination of tracks were acceptable. Approximately 4% of the frames contained more than one acceptable track combination, and in these cases the one with the best fit was used in the results.

The second part of the analysis involved inspecting the events which were run through MIN for final acceptability as follows:
1) The quantities calculated in 5) above (called D_k) were required to satisfy

$$D_k < \begin{cases} .80\ \mathrm{cm}^2 (k = 1) & \text{(east pion)} \\ .90\ \mathrm{cm}^2 (k = 2) & \text{(west pion)} \\ 1.90\ \mathrm{cm}^2 (k = 3) & \text{(proton)} \end{cases}$$

2) The final minimized fit to the event had to satisfy $F < 40$
3) A quantity B was calculated to indicate how much the measured θ_p had to be changed to fit kinematically with the other angles and the proton energy. Specifically, B was the difference between the θ_p given by a straight line fit to the proton sparks and the θ_p calculated by using the initial approximation to the proton energy and the other angles and solving the constraint equation. The requirement was $B < 2.4^{\circ}$
4) A quantity PULCHI (or P_x) was calculated as an indication of the fit between the pulses from counters P1 and P2 and the proton energy as it left the target (E_T). Specifically,

$$P_x = \left(\frac{P_1 - F_1(E_T)}{\sigma_1}\right)^2 + \left(\frac{P_2 - F_2(E_T)}{\sigma_2}\right)^2$$

where

$P_1(P_2)$ is the measured pulse height from counter P1(P2)

$\sigma_1(\sigma_2)$ is the total uncertainty in P1(P2)

$F_1(E_T)$ $(F_2(E_T))$ is the expected pulse height from counter P1(P2) for a proton leaving the target with energy E_T.

The limit $P_x < 16$ was required.

The limits on D_k, F, B, and P_x were determined by looking at the various distributions and setting a limit slightly below the point where the distribution differed significantly from background.

V. RESULTS

The major processes for dipion production in this energy region are normal three-body phase space, N*, and ρ^o. In general, the relative phases between these three amplitudes will vary with photon energy, so there may be relatively complicated interference effects distorting the cross sections. However, none of the experiments to date contains enough data to be able to determine the phases or their energy dependence. Therefore, the final event distribution will be fit to an incoherent sum of the three mechanisms described above with various models being tried for ρ^o production.

For each of the three experimental runs, the final accepted events were sorted into 20 MeV bins in $m_{\pi\pi}$ and 50 MeV bins in k (the photon energy). The indices k, m, and i will be used throughout this section to refer to the photon energy interval, dipion mass interval, and experimental run respectively. (Runs one, two, and three refer to the 24°, 20°, and 17° setups of the proton telescope respectively.) The experimental event distribution is shown in Table I. The effective number of BIPS accumulated during the experiment was 5380, 5277, and 3760 for the three setups respectively.

First, the event distribution expected from each of the three processes individually will be determined. Then the experimental event distribution will be fit to a combination of the three processes. Namely, if $N_{ps}(k, m, i)$, $N_{\rho}(k, m, i)$, and $N_*(k, m, i)$ are the appropriate event distributions, each normalized to

$$\sum_{k,m,i} N_{\alpha}(k, m, i) = 3018 \text{ events} \qquad (\alpha = ps,\ \rho^o,\ N^*)$$

where 3018 is the total number of experimental events, then the coefficients b_{ps}, b_{ρ}, and b_* will be chosen to minimize the function

	0.	0.	0.	0.	0.	0.	0.	0.	0.	0.	0.	0.	0.	0.	0.	0.	0.
	0.	1.0	0.	0.	0.	0.	0.	0.	0.	0.	0.	0.	0.	0.	0.	0.	0.
	0.	0.	0.	0.	0.	0.	0.	0.	0.	0.	0.	0.	0.	0.	0.	0.	0.
600 —	0.	0.	3.0	4.0	1.0	0.	0.	0.	0.	0.	0.	0.	0.	0.	0.	0.	0.
	0.	0.	1.0	3.0	3.0	0.	0.	0.	0.	0.	0.	0.	0.	0.	0.	0.	0.
	0.	0.	0.	0.	10.0	11.0	1.0	0.	0.	0.	0.	0.	0.	0.	0.	0.	0.
	0.	0.	0.	0.	1.0	16.0	15.0	0.	0.	0.	0.	0.	0.	0.	0.	0.	0.
	0.	0.	0.	0.	0.	5.0	24.0	19.0	3.0	0.	0.	0.	0.	0.	0.	0.	0.
700 —	0.	0.	0.	0.	0.	0.	7.0	29.0	33.0	4.0	0.	0.	0.	0.	0.	0.	0.
	0.	0.	0.	0.	0.	0.	0.	23.0	48.0	25.0	6.0	0.	0.	0.	0.	0.	C.
	0.	0.	0.	0.	0.	0.	0.	5.0	18.0	38.0	41.0	11.0	0.	C.	0.	0.	0.
	0.	0.	0.	0.	0.	0.	0.	0.	2.0	26.0	53.0	25.0	16.0	0.	0.	0.	C.
	0.	0.	0.	0.	0.	0.	0.	0.	0.	2.0	29.0	41.0	27.0	8.0	0.	0.	C.
800 —	0.	0.	0.	0.	0.	0.	0.	0.	0.	0.	2.0	25.0	37.0	11.C	2.0	0.	C.
	0.	0.	0.	0.	0.	0.	0.	0.	0.	0.	0.	6.0	16.0	12.0	0.	C.	C.
	0.	0.	0.	0.	C.	0.	0.	0.	C.	C.	0.	0.	4.0	7.0	1.C	C.	C.
	0.	0.	C.	0.	0.	0.	0.	0.	0.	0.	0.	0.	0.	5.C	2.0	0.	C.
	0.	0.	C.	0.	0.	0.	0.	0.	0.	0.	0.	0.	0.	2.C	1.0	0.	C.
900 —	0.	0.	0.	0.	0.	0.	0.	0.	0.	0.	0.	0.	0.	C.	0.	0.	C.
	0.	0.	C.	0.	0.	0.	0.	0.	C.	C.	0.	0.	0.	C.	0.	C.	C.
	0.	0.	0.	0.	0.	0.	0.	0.	0.	C.	0.	0.	0.	0.	0.	0.	C.
	0.	0.	0.	0.	0.	0.	0.	0.	0.	0.	0.	0.	0.	C.	0.	0.	C.
	0.	0.	C.	0.	C.	0.	0.	0.	0.	C.	0.	0.	0.	C.	0.	0.	C.
	0.	0.	0.	0.	0.	0.	0.	0.	0.	C.	0.	0.	0.	C.	0.	C.	C.
	0.	0.	0.	0.	0.	0.	0.	0.	C.	C.	0.	0.	0.	C.	0.	0.	C.
	0.	0.	0.	0.	0.	0.	0.	0.	0.	0.	0.	0.	0.	C.	0.	0.	C.

$m_{\pi\pi}$ ↓

RUN 1

	0.	0.	0.	0.	0.	0.	0.	0.	0.	0.	0.	0.	0.	0.	0.	0.	0.
	1.0	1.0	0.	0.	0.	0.	0.	0.	0.	0.	0.	0.	0.	0.	0.	0.	0.
	0.	1.0	0.	0.	0.	0.	0.	0.	0.	0.	0.	0.	0.	0.	0.	0.	C.
600 —	0.	0.	2.0	1.0	0.	0.	0.	0.	0.	0.	0.	0.	0.	0.	0.	0.	C.
	0.	0.	2.0	5.0	5.0	0.	0.	0.	0.	0.	0.	0.	0.	0.	0.	0.	C.
	0.	0.	0.	2.0	13.0	3.0	0.	0.	0.	0.	0.	0.	0.	0.	0.	C.	C.
	0.	0.	0.	0.	7.0	18.0	3.0	2.C	0.	0.	0.	0.	0.	0.	0.	0.	C.
	0.	0.	0.	0.	0.	20.0	27.0	9.0	2.0	0.	0.	0.	0.	0.	0.	0.	C.
700 —	0.	0.	C.	0.	0.	5.0	27.0	41.C	13.0	1.0	0.	0.	0.	C.	0.	C.	C.
	0.	0.	0.	0.	0.	0.	6.0	59.C	47.0	24.0	2.0	0.	0.	C.	0.	C.	C.
	0.	0.	0.	0.	C.	0.	0.	29.C	56.0	77.0	22.C	0.	0.	C.	0.	C.	C.
	0.	0.	0.	0.	0.	0.	0.	1.C	29.0	82.0	68.0	19.0	5.0	C.	0.	C.	C.
	0.	0.	0.	0.	0.	0.	0.	0.	3.0	35.0	89.C	65.0	22.0	C.	0.	C.	C.
800 —	0.	0.	C.	0.	0.	0.	0.	0.	0.	3.0	29.C	65.0	48.0	13.C	0.	C.	C.
	0.	0.	0.	0.	0.	0.	0.	0.	C.	0.	5.0	19.0	38.0	25.0	4.0	0.	C.
	0.	0.	C.	0.	0.	0.	0.	C.	0.	C.	1.0	6.0	12.0	17.0	4.0	0.	C.
	0.	0.	0.	0.	0.	0.	0.	0.	0.	C.	0.	1.0	2.0	6.0	2.C	C.	C.
	0.	0.	0.	0.	0.	0.	0.	0.	0.	C.	0.	0.	0.	5.0	3.0	0.	C.
900 —	0.	0.	0.	0.	0.	0.	0.	0.	0.	0.	0.	0.	0.	C.	0.	C.	C.
	0.	0.	0.	0.	0.	0.	0.	0.	0.	0.	0.	0.	0.	0.	0.	0.	C.
	0.	0.	0.	0.	0.	0.	C.	0.	0.	C.	0.	0.	0.	0.	0.	C.	C.
	0.	0.	C.	0.	0.	0.	0.	0.	0.	C.	0.	0.	0.	C.	0.	0.	C.
	0.	0.	0.	0.	0.	0.	0.	0.	0.	0.	0.	0.	0.	C.	0.	C.	C.
	0.	0.	0.	0.	0.	0.	0.	0.	0.	0.	0.	0.	0.	C.	0.	0.	C.
	0.	0.	0.	0.	0.	0.	0.	0.	0.	0.	0.	0.	0.	C.	0.	0.	C.
	0.	0.	C.	0.	0.	0.	0.	0.	0.	0.	0.	0.	0.	C.	0.	C.	C.

$m_{\pi\pi}$ ↓

RUN 2

	0.	0.	0.	0.	0.	0.	0.	0.	0.	0.	0.	0.	0.	0.	0.	0.	0.
	0.	0.	0.	0.	0.	0.	0.	0.	0.	0.	0.	0.	0.	0.	0.	0.	C.
	0.	0.	0.	0.	0.	0.	0.	0.	0.	0.	0.	0.	0.	0.	0.	0.	C.
600 —	0.	0.	0.	0.	0.	0.	0.	0.	0.	0.	0.	0.	0.	0.	0.	0.	C.
	0.	0.	3.0	3.0	0.	0.	0.	0.	0.	0.	0.	0.	0.	0.	0.	0.	C.
	0.	0.	2.0	3.0	9.0	0.	0.	0.	0.	0.	0.	0.	0.	0.	0.	0.	C.
	0.	0.	0.	0.	4.0	13.0	3.0	0.	0.	0.	0.	0.	0.	0.	0.	0.	C.
	0.	0.	C.	0.	4.0	20.0	13.0	5.C	0.	0.	0.	0.	0.	C.	0.	C.	C.
700 —	0.	0.	0.	0.	0.	9.0	32.0	22.C	4.0	0.	0.	0.	0.	0.	0.	0.	C.
	0.	0.	0.	0.	0.	1.0	16.0	41.C	32.0	4.0	0.	0.	0.	0.	0.	C.	C.
	0.	0.	0.	0.	0.	0.	2.0	25.0	52.0	23.0	11.0	3.0	0.	0.	0.	0.	C.
	0.	0.	0.	0.	0.	0.	0.	5.C	35.0	78.0	37.C	11.0	0.	C.	0.	C.	C.
	0.	0.	C.	0.	0.	0.	0.	0.	5.0	40.0	57.C	36.0	13.0	0.	0.	0.	C.
800 —	0.	0.	0.	0.	0.	0.	0.	0.	C.	9.0	46.0	36.0	28.0	9.C	1.C	0.	C.
	0.	0.	0.	0.	0.	0.	0.	0.	0.	1.0	7.0	33.C	25.0	21.C	3.C	0.	C.
	0.	0.	C.	0.	0.	0.	0.	0.	0.	C.	0.	6.0	23.0	23.C	7.C	C.	C.
	0.	0.	C.	0.	0.	0.	0.	0.	0.	C.	0.	2.0	5.0	8.C	6.0	0.	C.
	0.	0.	0.	0.	0.	0.	0.	0.	0.	C.	0.	0.	0.	9.0	1.C	C.	C.
900 —	0.	0.	0.	0.	0.	0.	0.	0.	0.	0.	0.	0.	0.	2.0	1.0	C.	C.
	0.	0.	0.	0.	0.	0.	0.	0.	0.	C.	0.	0.	0.	C.	0.	C.	C.
	0.	0.	C.	0.	0.	0.	0.	0.	0.	0.	0.	0.	0.	C.	0.	C.	C.
	0.	0.	C.	0.	0.	0.	0.	0.	0.	0.	0.	0.	0.	C.	0.	0.	C.
	0.	0.	0.	0.	0.	0.	0.	0.	0.	0.	0.	0.	0.	0.	0.	C.	C.
	0.	0.	0.	0.	0.	0.	0.	0.	0.	0.	0.	0.	0.	0.	0.	0.	C.
	0.	0.	C.	0.	0.	0.	0.	0.	0.	0.	0.	0.	0.	0.	0.	0.	C.
	0.	0.	0.	0.	0.	0.	0.	0.	0.	0.	0.	0.	0.	C.	0.	0.	C.

$m_{\pi\pi}$ ↓

1.0 1.2 1.4 k(BeV)

RUN 3

Experimental Event Distribution

TABLE I

$$\chi^2 = \left(\frac{N(k, m, i) - b_{ps} N_{ps}(k, m, i) - b_\rho N(k, m, i) - b_* N_*(k, m, i)}{\sigma_{kmi}} \right)^2$$

where

$$b_{ps} + b_\rho + b_* = 1$$

σ_{kmi} is the total r. m. s. uncertainty in the numerator.

In addition, since the detection efficiencies at a given k, m, and i are sharply peaked in the center-of-mass production angle θ, it is assumed that the events in the interval k, m, i give information on the cross sections only at one value of θ, namely $\theta(k, m, i)$ (see Table VIII).

A. Phase Space Production

The phase space production cross section is independent of the c. m. production angle θ, and is described by

$$g_{ps}(k, m) = \frac{pq}{W} \sigma_o$$

where

W = total c. m. energy

p = proton momentum in the c. m. system

q = pion momentum in the dipion c. m. system

σ_o = an unknown constant.

The phase space detection efficiency $E_{ps}(k, m, i)$ has been described in Appendix V. The event distribution expected from phase space production alone is then given by

$$N_{ps}(k, m, i) = C_{ps} H(k, i)\, E_{ps}(k, m, i)\, g_{ps}(k, m)$$

where

$H(k, i) = 4\pi\, \Delta m\, N_{\gamma}(k, i)\, N_H$

Δm = 20 MeV (the $m_{\pi\pi}$ mass interval)

$N_{\gamma}(k, i)$ = the number of incoming photons in a 50 MeV interval about k, for experimental run i

$N_H = 4.64 \times 10^{23}$ protons/cm^2

C_{ps} = is a normalization factor .

B. Rho Production

The cross section for ρ^{o} production by any model can be described by a function

$$g_{\rho}(k, m, i) = \frac{d^2\sigma}{d\Omega dm}(k, m, \theta_{kmi}) .$$

To properly determine the detection efficiency $E_\rho(k, m, i)$, one must first know the decay distribution of the ρ^o in its rest frame. This experiment was only sensitive to the decay angles $\theta_d = 90^o \pm 9^o$ and $\varphi_d = 90^o \pm 17^o$ (θ_d is the angle between the decay π^+ and the incoming photon in the ρ^o rest frame, and φ_d is the Trieman-Yang angle(40)). So if the ρ^o decay distribution is not changing with energy, the efficiencies $E_\rho(k, m, i)$ and $E_{ps}(k, m, i)$ may differ only by a multiplicative constant. Furthermore, since the decay distribution does not show an enhancement at $\theta_d = \pi/2$ and $\varphi_d = \pi/2$(12, 13), the efficiencies $E_\rho(k, m, i)$ and $E_{ps}(k, m, i)$ were assumed identical. If future experiments find that this is not true, then the ρ^o cross sections found below must be multiplied by the appropriate constant.

The event distribution expected from ρ^o production alone is

$$N_\rho(k, m, i) = C_\rho H(k, i)\, E_\rho(k, m, i)\, g_\rho(k, m, i)$$

where

$H(k, i)$ has been described above for phase space

C_ρ is a normalization constant.

For any of the theoretical models, the cross section is factored into

$$g_\rho(k, m, i) = P_\rho(m) \frac{d\sigma}{d\Omega}(k, m, \theta_{kmi})$$

where

$P_\rho(m)$ = the resonant factor

$$P_\rho(m) = A \frac{m\, m_\rho \Gamma(m)}{(m^2 - m_\rho^2)^2 + m_\rho^2 \Gamma(m)^2}$$

m_ρ = resonant mass of the ρ^0

$$\Gamma(m) = \Gamma_0 (q/q_0)^3 \frac{m_\rho}{m}$$

Γ_0 = central width of the ρ^0 resonance

q = momentum of the π^+ in the ρ^0 rest frame

q_0 = the value of q for $m = m_\rho$

θ_{kmi} = the c.m. production angle at which the efficiency $E_\rho(k, m, i)$ is peaked

A = normalization constant such that $\int P(m)dm = 1$.

The form for $\Gamma(m)$ is given by Jackson$^{(41)}$ using first order perturbation theory. Throughout the fitting procedure, Γ_0 and m_ρ will be variable and their values for any particular ρ^0 model will be determined by minimizing the χ^2 defined at the beginning of this section.

The following models for ρ^o production will be tried.

1. The unmodified one pion exchange (OPE) model(18, 19) gives

$$\left(\frac{d\sigma}{d\Omega}\right)_{\substack{OPE\\ Lab}} = \left(\frac{g^2_{\pi NN}}{4\pi}\right)\left(\frac{\Gamma_{\rho\pi\gamma}}{m}\right)\frac{t}{m^2}\left(\frac{3p^2}{2k^2}\right)\left(\frac{t+m^2}{t+m_\pi^2}\right)^2\frac{1}{m_p^2 B}$$

where

$g_{\pi NN}$ is the π-N coupling constant

$\Gamma_{\rho\pi\gamma}$ is the width for the process $\rho \rightarrow \pi + \gamma$

t is the invariant momentum transfer

p is the momentum of the ρ^o in the lab

$m_p(m_\pi)$ is the proton (pion) mass

m is the dipion mass

$$B = \frac{1}{m_p k}\left[\left(m_p k - \frac{m^2}{2}\right)^2 - m^2\left((m_p+k)^2 - k^2\cos^2\theta\right)\right]^{1/2}$$

θ is the angle of the proton in the lab.

2. The OPE model with a form factor dependence on the pion propagator(24) gives

$$\left(\frac{d\sigma}{d\Omega}\right)_{FF} = \left(\frac{d\sigma}{d\Omega}\right)_{OPE} \left(\frac{x^2}{t+x^2}\right)^2 .$$

In this case the value of x is to be determined by minimizing χ^2.

3. The Amati-Fubini-Staghellini$^{(22, 24)}$ model for diffraction production gives

$$\left(\frac{d\sigma}{d\Omega}\right)_{diff} = \left(\frac{1+\cos^2\theta}{16}\right) \frac{p}{E} \frac{[g^2_{\omega\pi\gamma}/4\pi][g^2_{\rho\pi\omega}/4\pi]}{(12\,\Gamma_\rho/m_\rho)^2} \left(\frac{d\sigma}{d\Omega}\right)_{\pi n}$$

where

p(E) is the momentum (energy) of the ρ^0

θ is the ρ^0 production angle

$g_{\omega\pi\gamma}$ and $g_{\rho\pi\omega}$ are the $\omega\pi\gamma$ and $\rho\pi\omega$ vertex coupling constants

$\left(\frac{d\sigma}{d\Omega}\right)_{\pi N}$ is the differential cross section for the reaction

$$\pi + p \rightarrow \pi + p .$$

The diffraction model, however, is of dubious applicability in this energy region for several reasons. First, the reaction $\pi + p \rightarrow \pi + p$ is not dominated by diffraction at the low energies considered here. Second, the formula above is an approximation valid only for $\theta \approx 0$. Third, the phase space available for ρ^0 production is *changing* significantly over the energy interval $850 < k < 1500$ MeV and the above formula is a higher energy approximation. Nevertheless, the diffraction model will be tried as a matter of interest. The form of the π-p cross section is

$$\left(\frac{d\sigma}{d\Omega}\right)_{\pi N} \propto \exp\left(-t/t_o\right) .$$

The energy variation of $\left(\frac{d\sigma}{d\Omega}\right)$ is small in the relevant energy region and was thus considered constant. The momentum transfer dependence, t_o, is then a variable to be determined by the usual χ^2 minimization.

Since the formula for $\left(\frac{d\sigma}{d\Omega}\right)_{\text{diff}}$ is a higher energy approximation, two methods for simulating the ρ^o threshold effects were tried. First, $\left(\frac{d\sigma}{d\Omega}\right)_{\text{diff}}$ was simply multiplied by the density of final states. Second, $(d\sigma/d\Omega)_{\text{diff}}$ was multiplied by the phenomenological threshold factor

$$f(k) = \sqrt{k - k_T(m)} - .013 \text{ MeV}^{-1/2}(k-k_T(m))$$

which was the form of f(k) given by the phenomenological model below. This second method gave a slightly better χ^2 fit than the first, so in the discussion below, the "diffraction model" refers to the second method for representing the threshold effects.

4. Finally, the event distribution can be fit with a purely phenomenological cross section

$$\frac{d\sigma}{d\Omega} = f(k)[1 + \alpha_2(1 - \cos\theta) + \alpha_3(1 - \cos\theta)^2 + \alpha_4(1 - \cos\theta)^3]$$

where α_2, α_3, and α_4 are parameters to be optimized. Several forms for $f(k)$ were tried. The form which gave the best fit was

$$f(k) = \sqrt{k - k_T(m)} - \alpha_1(k - k_T(m))$$

where $k_T(m)$ is the threshold energy for producing a dipion with mass m.

The presence of the α_4 term in $\frac{d\sigma}{d\Omega}$ improves the χ^2 negligibly and changes the parameters b, b_{ps}, m, and Γ_o by only a small fraction of their errors. This is evidence that a higher order polynomial in $\cos\theta_{cm}$ would not significantly improve the final fit.

C. N* Production

Since N* production produced so few events in this experiment, we could not reasonably expect to determine any of the parameters for N* production better than has been done already. For the initial fits, the energy and angular dependence of the N* cross section was taken from Tables IV and V of Michael Hauser's thesis, and the absolute value of the cross section was treated as variable. The expected contribution from the N* should have been

$$b_* = 10.2\% .$$

Since most fits gave $b_* \approx 8\% \pm 2\%$, the event distribution for N* production was then considered constant at $b_* = 10.2\%$ in all future fits.

The event distribution expected from N* production was determined as follows. Since both the energy and angular dependence of the cross section and the shape of the N* mass distribution are known, we have

$$N_*(k, m, i) = [H(k, i)/4\pi]\, g_*(k, m, i)$$

where

$$g_*(k, m, i) = \sigma_*(k) \int_{1080}^{m_2} E_*(k, m, i, m^*)\, P_*(m^*)\, dm^*$$

$\sigma_*(k)$ is the total cross section for N* production

$$P_*(m^*) = A \frac{m^* m_o \Gamma(m^*)}{(m^{*2} - m_o^2)^2 + m_o^2 \Gamma^2(m^*)}$$

$$m_o = 1238 \text{ MeV}$$

$$\Gamma(m^*) = \Gamma_o (q/q_o)^3 \frac{\rho(m^*)}{\rho(m_o)}$$

$$\Gamma_o = 123 \text{ MeV}$$

$q(q_o)$ is the momentum of the decay pion in the N* c. m. system for an N* mass of $m^*(m_o)$

$$\rho(m^*) = \frac{(m^* + m_\rho)^2 - m_\pi^2}{m^{*2}}$$

A is a normalization constant such that $\int_{1080}^{\infty} P(m^*)\, dm^* = 1$

$E_*(k, m, i, m^*)$ is discussed below

m_2 is the upper limit on the N* mass which can be produced by photon energy k .

The efficiency $E_*(k, m, i, m^*)$ is the efficiency for detecting an N* event produced with isobar mass m*, dipion mass m, and photon energy k, for experimental run i. The N* detection efficiency program (see Appendix V. D) only determined the efficiency $E(k, i, m^*)$, where

$$E(k, i, m^*) = \int E_*(k, m, i, m^*)\, dm\ .$$

Thus, $E_*(k, m, i, m^*)$ is simply a decomposition of $E(k, i, m^*)$ into its dipion mass spectrum. The factor $g_*(k, m, i)$ then represents the number of N* events expected in the interval k, m, i per target proton and per incident photon.

The final event distribution $N_*(k, m, i)$ obtained with $b_* = 10.2\%$ is shown in Table II.

$m_{\pi\pi}$ ↓																	
	0.66	0.54	0.	0.	0.	0.	0.	0.	0.	0.	0.	0.	0.	0.	0.	0.	-0.
	0.	2.37	0.68	0.	0.	0.	0.	0.	0.	0.	0.	0.	0.	0.	0.	0.	-0.
	0.	0.	0.41	0.23	0.	0.	0.	0.	0.	0.	0.	0.	0.	0.	0.	0.	-0.
600	0.	0.	1.13	4.61	0.69	0.	0.	0.	0.	0.	0.	0.	0.	0.	0.	0.	-0.
	0.	0.	0.	1.78	3.07	0.46	0.	0.	0.	0.	0.	0.	0.	0.	0.	0.	-0.
	0.	0.	0.	0.	2.90	2.85	0.50	0.	0.	0.	0.	0.	0.	0.	0.	0.	-0.
	0.	0.	0.	0.	0.59	2.79	2.72	0.27	0.	0.	0.	0.	0.	0.	0.	0.	-0.
	0.	0.	0.	0.	0.	1.02	3.39	1.58	0.59	0.06	0.	0.	0.	0.	0.	0.	-0.
700	0.	0.	0.	0.	0.	0.	1.24	4.00	1.72	0.26	0.05	0.	0.	0.	0.	0.	-0.
	0.	0.	0.	0.	0.	0.	0.07	1.76	3.52	1.23	0.20	0.	0.	0.	0.	0.	-0.
	0.	0.	0.	0.	0.	0.	0.	0.28	1.75	2.31	1.12	0.17	0.02	0.	0.	0.	-0.
	0.	0.	0.	0.	0.	0.	0.	0.	0.25	1.01	1.94	1.10	0.14	0.	0.	0.	-0.
	0.	0.	0.	0.	0.	0.	0.	0.	0.	0.43	1.58	1.56	0.68	0.08	0.00	0.	-0.
800	0.	0.	0.	0.	0.	0.	0.	0.	0.	0.06	0.62	1.47	0.96	0.31	0.02	0.00	-0.
	0.	0.	0.	0.	0.	0.	0.	0.	0.	0.	0.09	0.59	0.96	0.58	0.04	0.00	-0.
	0.	0.	0.	0.	0.	0.	0.	0.	0.	0.	0.	0.08	0.69	0.54	0.06	0.00	-0.
	0.	0.	0.	0.	0.	0.	0.	0.	0.	0.	0.	0.	0.12	0.33	0.06	0.00	-0.
	0.	0.	0.	0.	0.	0.	0.	0.	0.	0.	0.	0.	0.	0.06	0.04	0.00	-0.
900	0.	0.	0.	0.	0.	0.	0.	0.	0.	0.	0.	0.	0.	0.	0.01	0.00	-0.
	0.	0.	0.	0.	0.	0.	0.	0.	0.	0.	0.	0.	0.	0.	0.00	0.00	-0.
	-0.	-0.	-0.	-0.	-0.	-0.	-0.	-0.	-0.	-0.	-0.	-0.	-0.	-0.	-0.	-0.	0.
	-0.	-0.	-0.	-0.	-0.	-0.	-0.	-0.	-0.	-0.	-0.	-0.	-0.	-0.	-0.	-0.	0.
	-0.	-0.	-0.	-0.	-0.	-0.	-0.	-0.	-0.	-0.	-0.	-0.	-0.	-0.	-0.	-0.	0.
	-0.	-0.	-0.	-0.	-0.	-0.	-0.	-0.	-0.	-0.	-0.	-0.	-0.	-0.	-0.	-0.	0.
	-0.	-0.	-0.	-0.	-0.	-0.	-0.	-0.	-0.	-0.	-0.	-0.	-0.	-0.	-0.	-0.	0.

RUN 1

$m_{\pi\pi}$ ↓																	
	2.31	0.	0.	0.	0.	0.	0.	0.	0.	0.	0.	0.	0.	0.	0.	0.	-0.
	2.43	3.14	0.	0.	0.	0.	0.	0.	0.	0.	0.	0.	0.	0.	0.	0.	-0.
	0.	4.26	1.99	0.	0.	0.	0.	0.	0.	0.	0.	0.	0.	0.	0.	0.	-0.
600	0.	0.	6.24	3.22	0.10	0.	0.	0.	0.	0.	0.	0.	0.	0.	0.	0.	-0.
	0.	0.	0.34	8.01	2.28	0.04	0.	0.	0.	0.	0.	0.	0.	0.	0.	0.	-0.
	0.	0.	0.	3.22	7.06	1.94	0.09	0.	0.	0.	0.	0.	0.	0.	0.	0.	-0.
	0.	0.	0.	0.	4.28	6.19	1.35	0.03	0.	0.	0.	0.	0.	0.	0.	0.	-0.
	0.	0.	0.	0.	0.49	6.58	5.50	1.71	0.10	0.	0.	0.	0.	0.	0.	0.	-0.
700	0.	0.	0.	0.	0.	0.22	5.59	4.64	1.28	0.26	0.	0.	0.	0.	0.	0.	-0.
	0.	0.	0.	0.	0.	0.	1.05	6.14	4.37	0.80	0.14	0.	0.	0.	0.	0.	-0.
	0.	0.	0.	0.	0.	0.	0.	1.72	5.22	3.70	0.80	0.10	0.	0.	0.	0.	-0.
	0.	0.	0.	0.	0.	0.	0.	0.07	2.35	4.01	2.87	0.78	0.14	0.	0.	0.	-0.
	0.	0.	0.	0.	0.	0.	0.	0.	0.37	2.13	3.14	2.40	0.45	0.07	0.	0.	-0.
800	0.	0.	0.	0.	0.	0.	0.	0.	0.	0.92	2.19	2.35	1.43	0.38	0.01	0.	-0.
	0.	0.	0.	0.	0.	0.	0.	0.	0.	0.	0.71	2.29	2.10	0.65	0.03	0.00	-0.
	0.	0.	0.	0.	0.	0.	0.	0.	0.	0.	0.	0.87	1.34	0.93	0.06	0.00	-0.
	0.	0.	0.	0.	0.	0.	0.	0.	0.	0.	0.	0.12	1.06	0.82	0.11	0.00	-0.
	0.	0.	0.	0.	0.	0.	0.	0.	0.	0.	0.	0.	0.29	0.64	0.10	0.00	-0.
900	0.	0.	0.	0.	0.	0.	0.	0.	0.	0.	0.	0.	0.	0.20	0.08	0.00	-0.
	0.	0.	0.	0.	0.	0.	0.	0.	0.	0.	0.	0.	0.	0.	0.04	0.00	-0.
	-0.	-0.	-0.	-0.	-0.	-0.	-0.	-0.	-0.	-0.	-0.	-0.	-0.	-0.	-0.	-0.	0.
	-0.	-0.	-0.	-0.	-0.	-0.	-0.	-0.	-0.	-0.	-0.	-0.	-0.	-0.	-0.	-0.	0.
	-0.	-0.	-0.	-0.	-0.	-0.	-0.	-0.	-0.	-0.	-0.	-0.	-0.	-0.	-0.	-0.	0.
	-0.	-0.	-0.	-0.	-0.	-0.	-0.	-0.	-0.	-0.	-0.	-0.	-0.	-0.	-0.	-0.	0.
	-0.	-0.	-0.	-0.	-0.	-0.	-0.	-0.	-0.	-0.	-0.	-0.	-0.	-0.	-0.	-0.	0.

RUN 2

$m_{\pi\pi}$ ↓																	
	0.37	0.	0.	0.	0.	0.	0.	0.	0.	0.	0.	0.	0.	0.	0.	0.	-0.
	0.73	0.26	0.	0.	0.	0.	0.	0.	0.	0.	0.	0.	0.	0.	0.	0.	-0.
	0.	3.15	0.69	0.	0.	0.	0.	0.	0.	0.	0.	0.	0.	0.	0.	0.	-0.
600	0.	0.	3.87	0.85	0.	0.	0.	0.	0.	0.	0.	0.	0.	0.	0.	0.	-0.
	0.	0.	1.56	4.50	0.27	0.	0.	0.	0.	0.	0.	0.	0.	0.	0.	0.	-0.
	0.	0.	0.	2.47	4.59	0.34	0.	0.	0.	0.	0.	0.	0.	0.	0.	0.	-0.
	0.	0.	0.	0.	4.51	2.79	0.47	0.	0.	0.	0.	0.	0.	0.	0.	0.	-0.
	0.	0.	0.	0.	1.01	3.79	3.41	0.51	0.03	0.	0.	0.	0.	0.	0.	0.	-0.
700	0.	0.	0.	0.	0.	1.56	3.44	1.86	0.49	0.04	0.	0.	0.	0.	0.	0.	-0.
	0.	0.	0.	0.	0.	0.	1.19	3.21	2.03	0.22	0.03	0.	0.	0.	0.	0.	-0.
	0.	0.	0.	0.	0.	0.	0.	2.23	3.07	1.51	0.39	0.04	0.	0.	0.	0.	-0.
	0.	0.	0.	0.	0.	0.	0.	0.16	2.17	2.35	1.05	0.30	0.01	0.	0.	0.	-0.
	0.	0.	0.	0.	0.	0.	0.	0.	0.43	2.17	2.31	0.76	0.11	0.01	0.	0.	-0.
800	0.	0.	0.	0.	0.	0.	0.	0.	0.	1.27	2.20	1.67	0.54	0.09	0.00	0.	-0.
	0.	0.	0.	0.	0.	0.	0.	0.	0.	0.04	0.69	1.54	1.35	0.29	0.01	0.00	-0.
	0.	0.	0.	0.	0.	0.	0.	0.	0.	0.	0.17	0.93	0.90	0.54	0.04	0.00	-0.
	0.	0.	0.	0.	0.	0.	0.	0.	0.	0.	0.	0.14	0.88	0.52	0.06	0.00	-0.
	0.	0.	0.	0.	0.	0.	0.	0.	0.	0.	0.	0.	0.32	0.43	0.07	0.00	-0.
900	0.	0.	0.	0.	0.	0.	0.	0.	0.	0.	0.	0.	0.	0.23	0.05	0.00	-0.
	0.	0.	0.	0.	0.	0.	0.	0.	0.	0.	0.	0.	0.	0.02	0.03	0.00	-0.
	-0.	-0.	-0.	-0.	-0.	-0.	-0.	-0.	-0.	-0.	-0.	-0.	-0.	-0.	-0.	-0.	0.
	-0.	-0.	-0.	-0.	-0.	-0.	-0.	-0.	-0.	-0.	-0.	-0.	-0.	-0.	-0.	-0.	0.
	-0.	-0.	-0.	-0.	-0.	-0.	-0.	-0.	-0.	-0.	-0.	-0.	-0.	-0.	-0.	-0.	0.
	-0.	-0.	-0.	-0.	-0.	-0.	-0.	-0.	-0.	-0.	-0.	-0.	-0.	-0.	-0.	-0.	0.
	-0.	-0.	-0.	-0.	-0.	-0.	-0.	-0.	-0.	-0.	-0.	-0.	-0.	-0.	-0.	-0.	0.

1.0 1.2 1.4 k(BeV)

RUN 3

Event Distribution from N^* Production

TABLE II

Figure 10 shows the fit between various ρ^o models and the experimental mass distributions, and Table III summarizes the final parameters from each fit. Figure 11 compares the angular distribution from the various ρ^o models. Figure 12.1 shows the experimental angular distributions for various dipion mass intervals. These were obtained by dividing the data into .02 bins in $\cos\theta_{cm}$ and calculating the weighted average of $d^2\sigma/d\Omega dm$ in each $\cos\theta_{cm}$ bin. Figure 12.2 shows the angular distributions and total cross sections determined by previous experiments.

The resonant mass m_ρ deduced by the various fits is in the range $737 < m_\rho < 750$ which is consistent with previous experiments. The history of the ρ^o mass deduced from photoproduction experiments is worth noting here. The first observation of the ρ^o resonance(12) found $m_\rho = 725 \pm 5$ MeV, much lower than the value of 755 MeV from production by pions.(25) The CEA group(22) finds $m_\rho = 728 \pm 8$ MeV, and the DESY collaboration the mass decreasing from 760 MeV at threshold to about 725 MeV at a photon energy of 5 BeV. Recent experiments in production from complex nuclei,(43, 44) find 765 ± 5 MeV. In most cases, the rho mass found in photoproduction is lower than the currently accepted value of 755 ± 3 MeV from production by pions(49). This raises some interesting questions as to the existence of interference effects between ρ^o production and the background. Also, if an ϵ^o meson with $J^{PG} = 0^{++}$ exists, it will obviously have a strong influence on the interpretation of the results from dipion production.

The width of the resonance varied over the range $122 < \Gamma_o < 150$. The values of Γ_o from previous experiments vary widely. The DESY group found $112 < \Gamma_o < 198$ MeV depending on the photon energy considered. The CEA group also found $125 < \Gamma_o < 225$ depending on the photon energy interval. The production of ρ^o's from complex nuclei(43, 44) gives $\Gamma_o = 124$ MeV found in production by pions.(49)

Figure 10

There are a pair of figures for each ρ^o model - one comparing the expected and observed π-π mass plots for each run and the other comparing the expected and observed distribution in photon energy for each run. For the mass plot, the curve indicating the final fit was obtained from the summation over photon energy.

$$\sum_k [b_\rho N_\rho(k, m, i) + b_{ps} N_{ps}(k, m, i) + b_* N_*(k, m, i)] .$$

For the photon energy distributions, the curve indicating the final fit was the summation over dipion mass

$$\sum_m [b_\rho N_\rho(k, m, i) + b_{ps} N_{ps}(k, m, i) + b_* N_*(k, m, i)] .$$

Also shown are the individual contributions from phase space and N* production. The N* contribution is indicated by the dashed lines and the phase space contribution by the dash-dotted lines (when $b_{ps} \neq 0$).

Figure 10.1

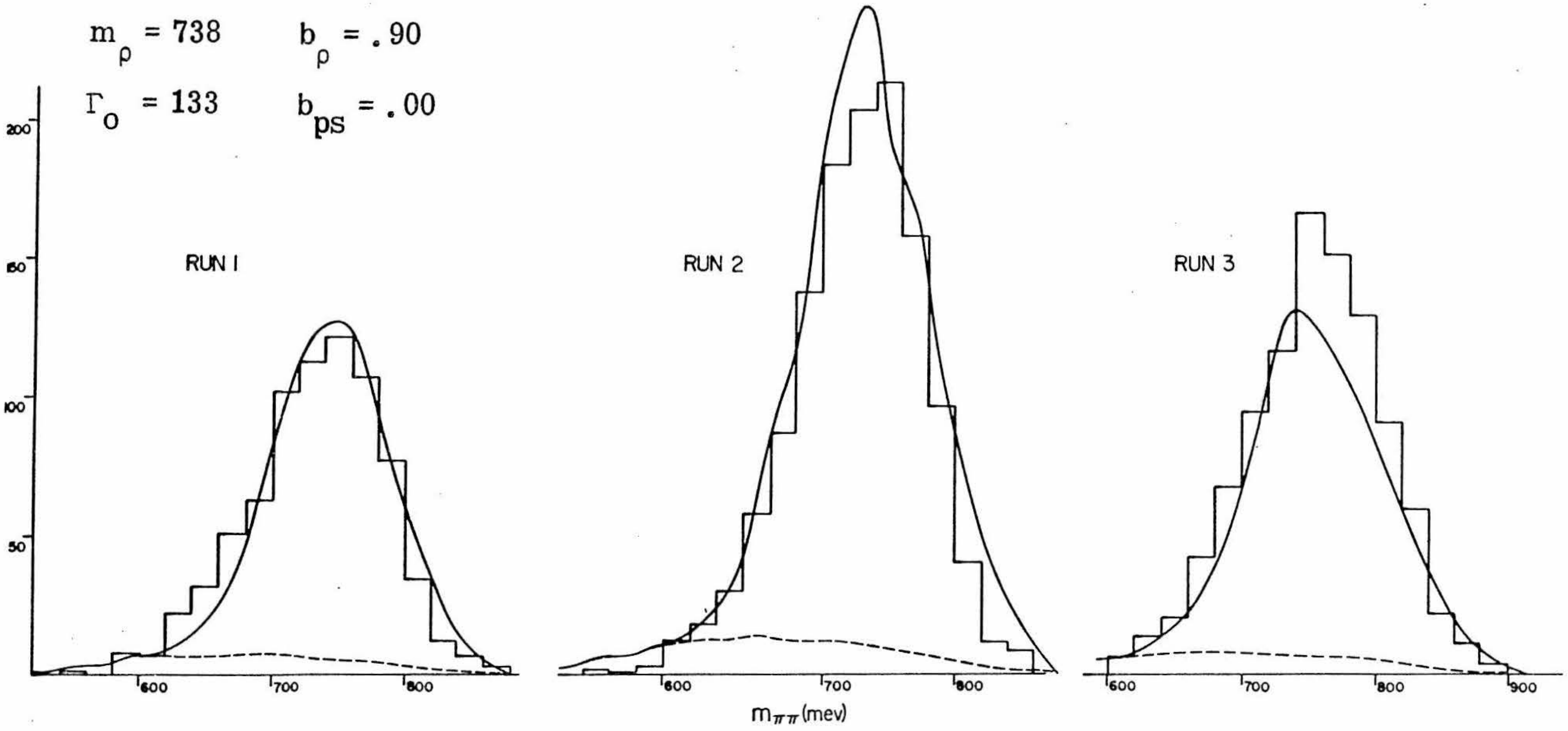

OPE Model

Figure 10.2

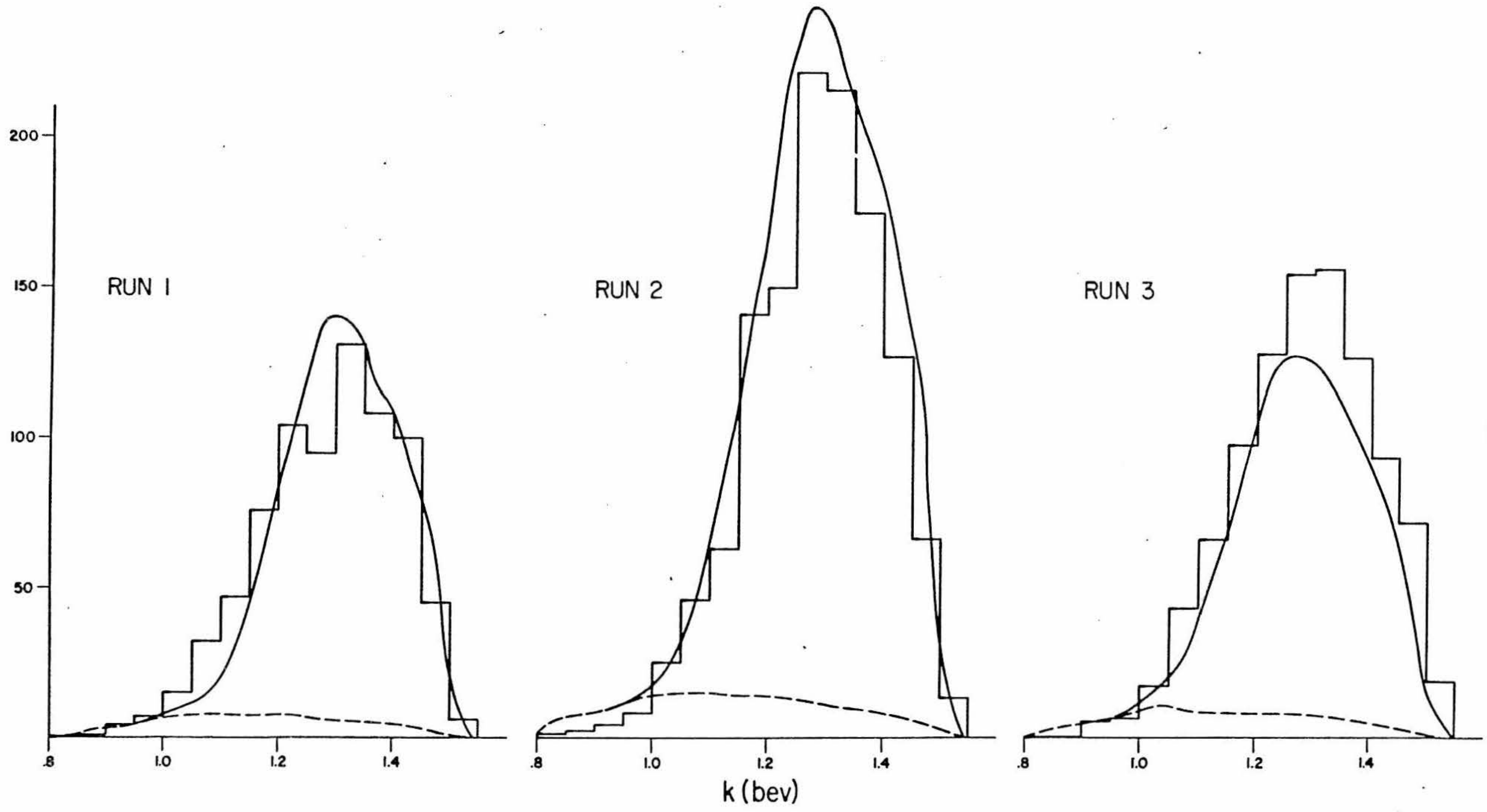

OPE Model

m_ρ = 750 b_ρ = .90
Γ_o = 150 b_{ps} = .00
x = 266 MeV

Figure 10.3

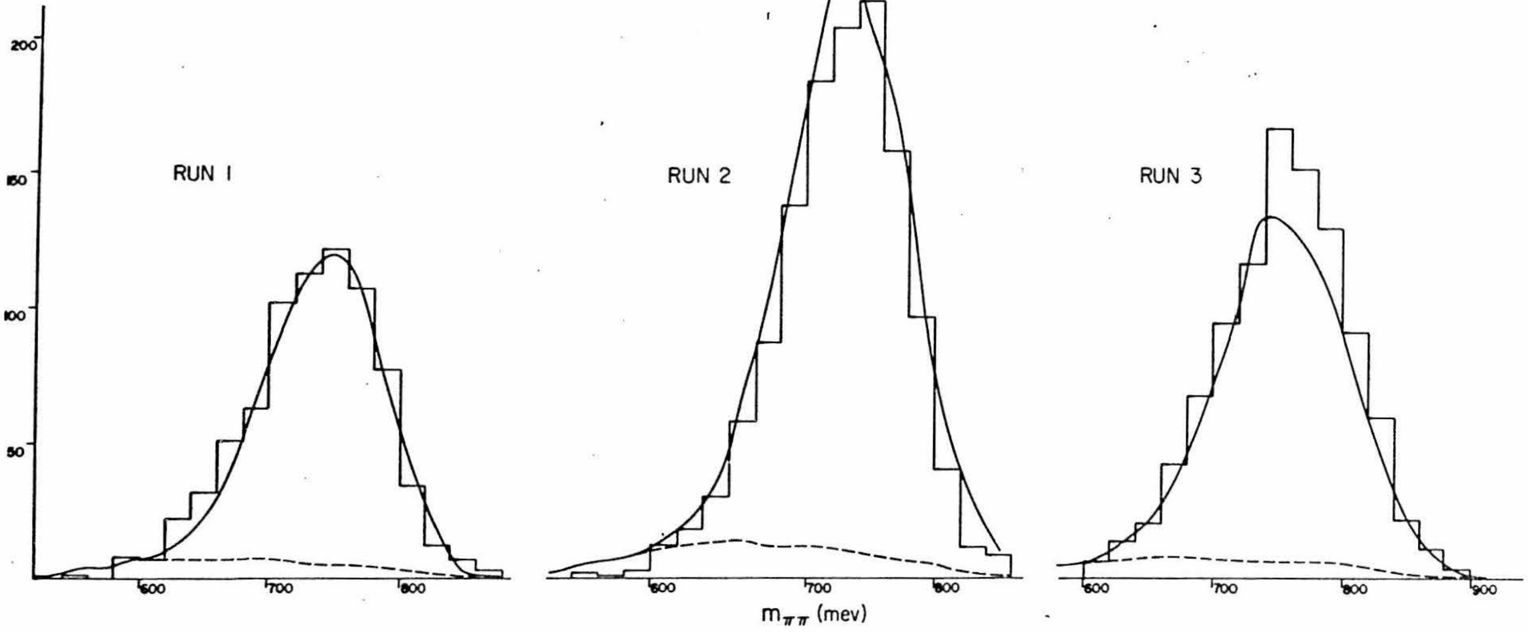

OPE with Form Factor

Figure 10.4

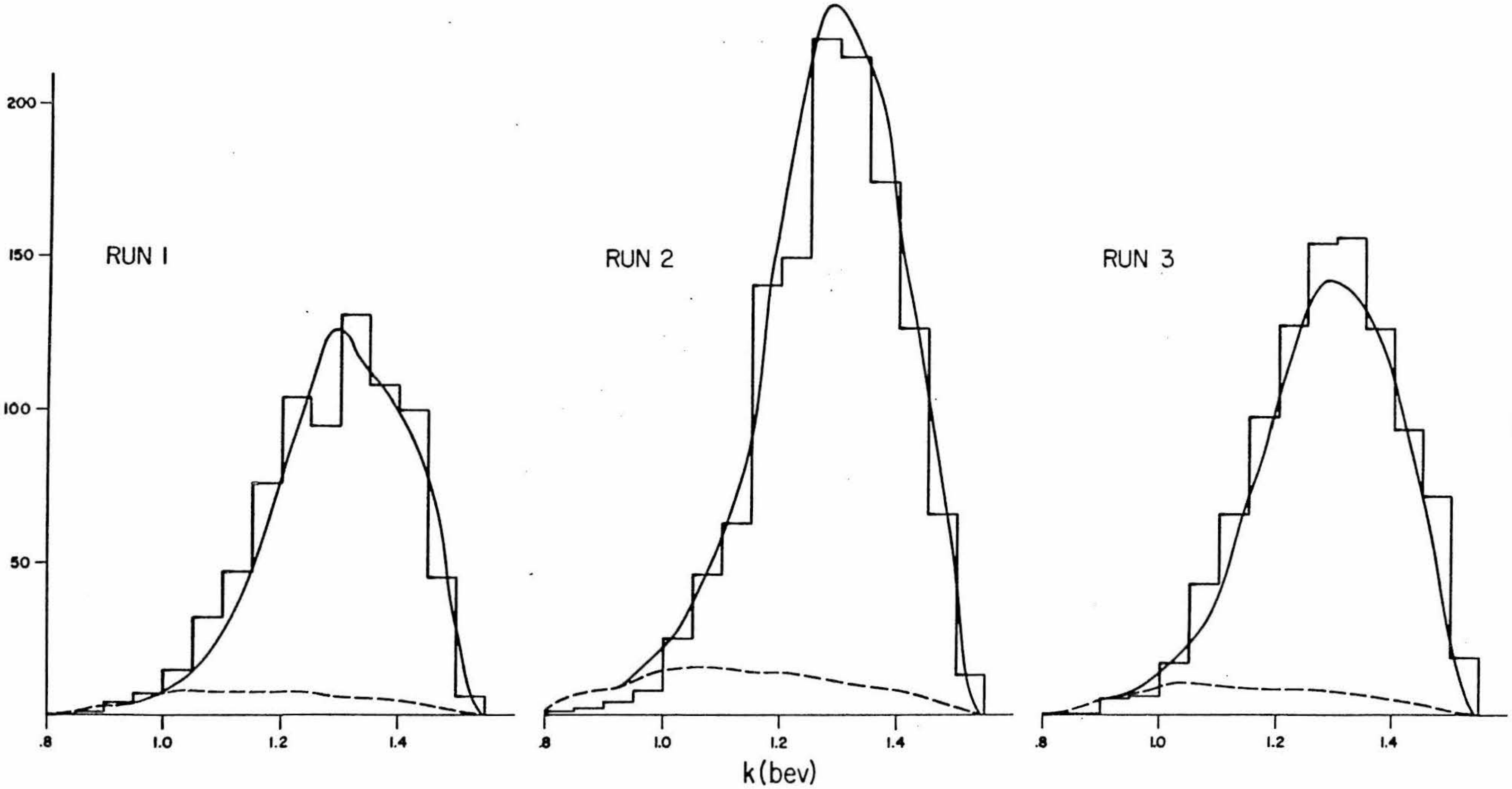

OPE with Form Factor

Figure 10.5

$m_\rho = 743$ $b_\rho = .90$

$\Gamma_o = 142$ $b_{ps} = .00$

$t_o = .956\ \text{BeV}^2$

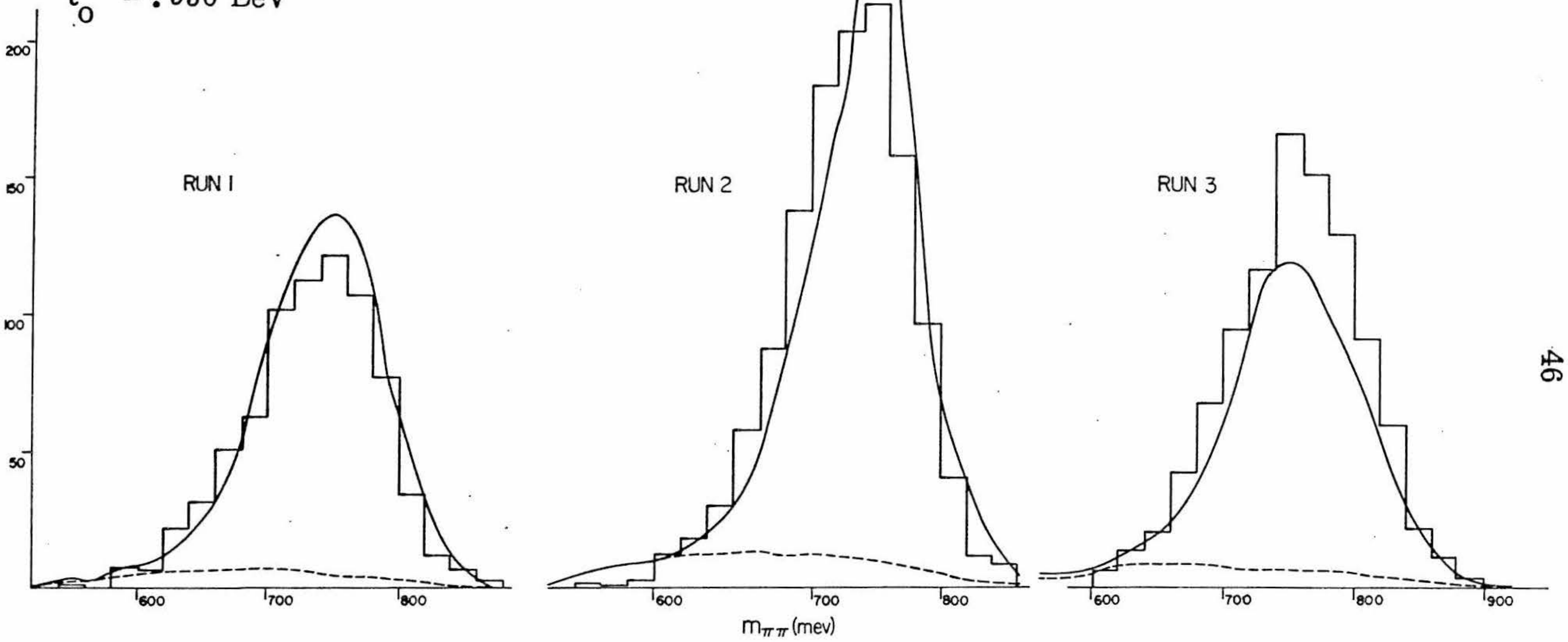

Diffraction Model

Figure 10.6

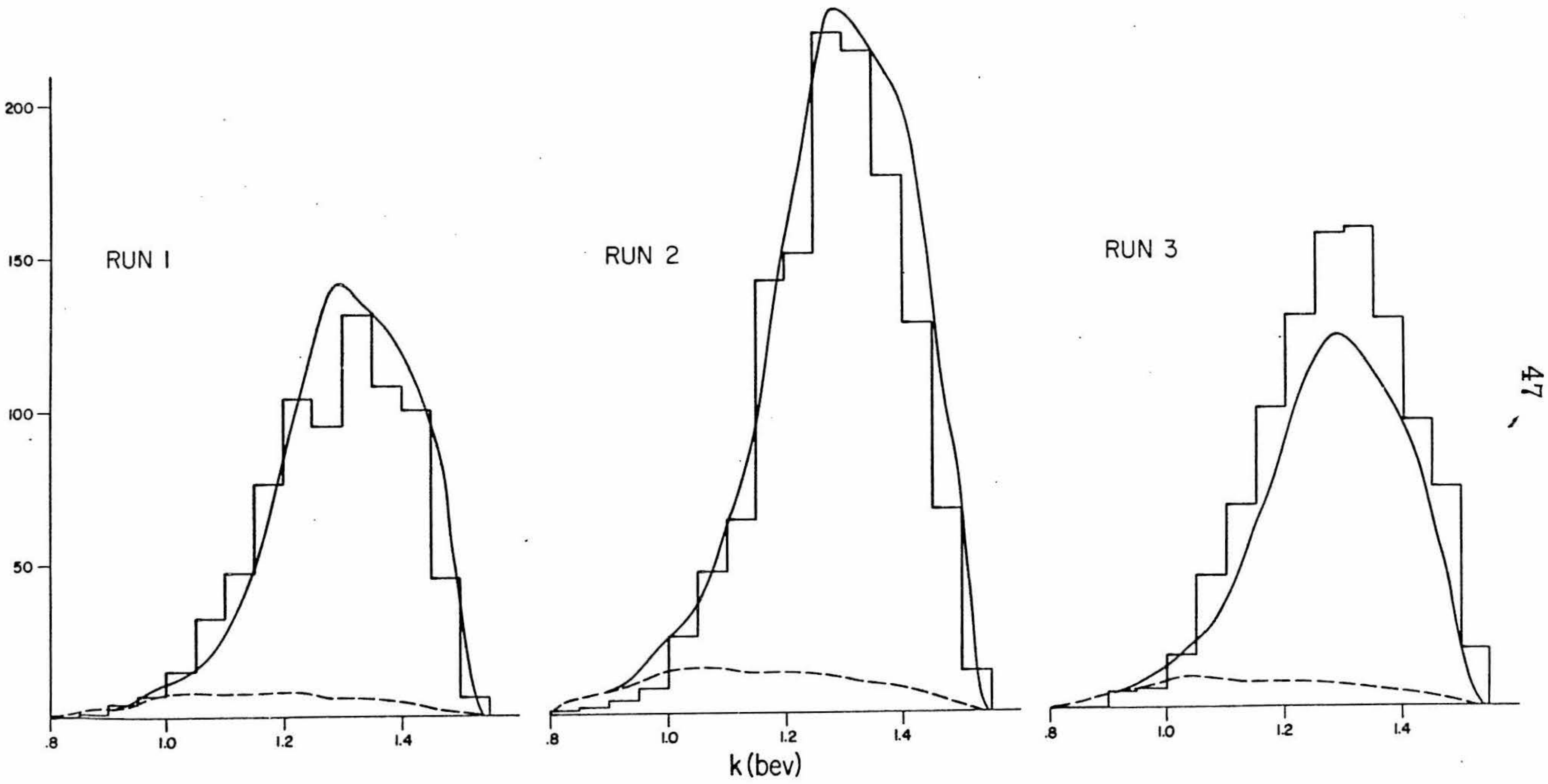

Diffraction Model

Figure 10.7

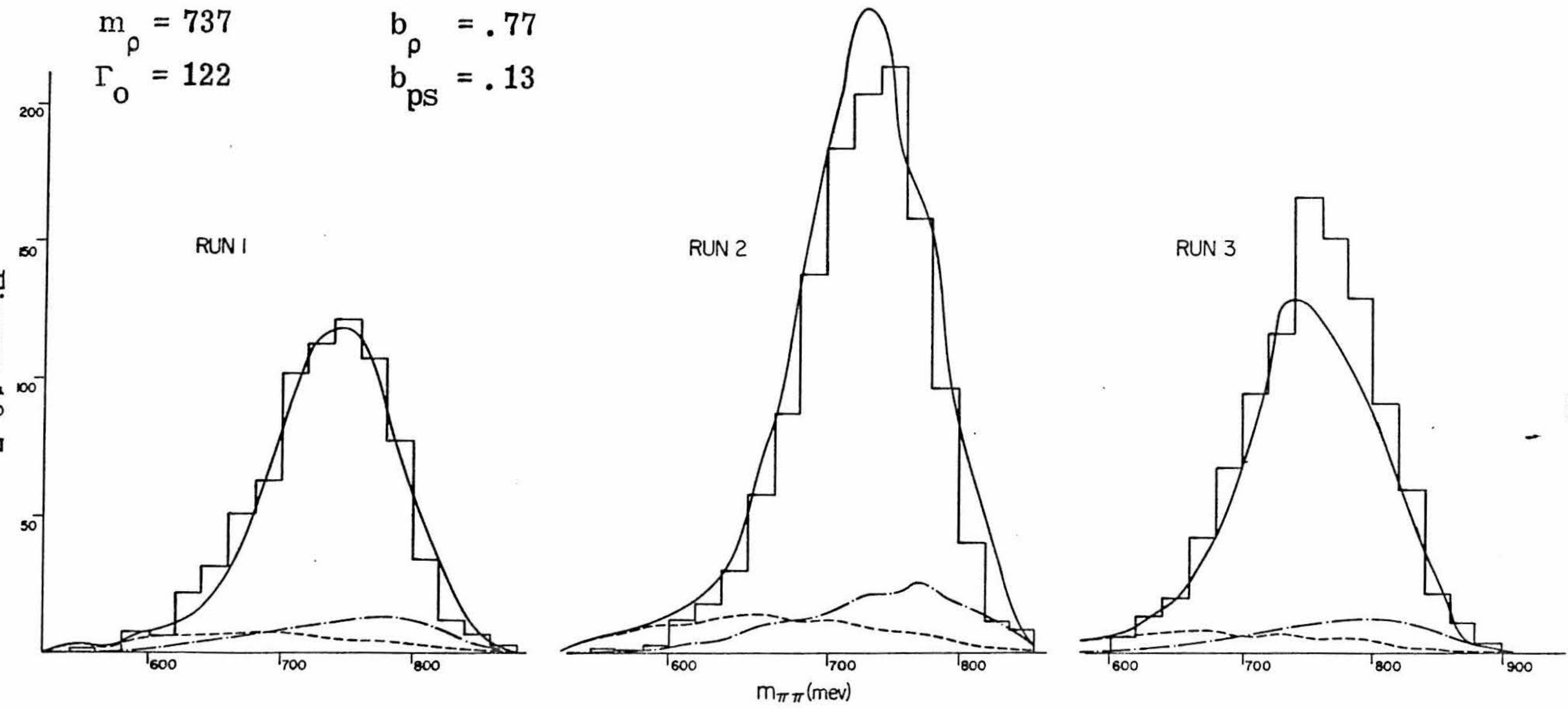

Phenomenological Model

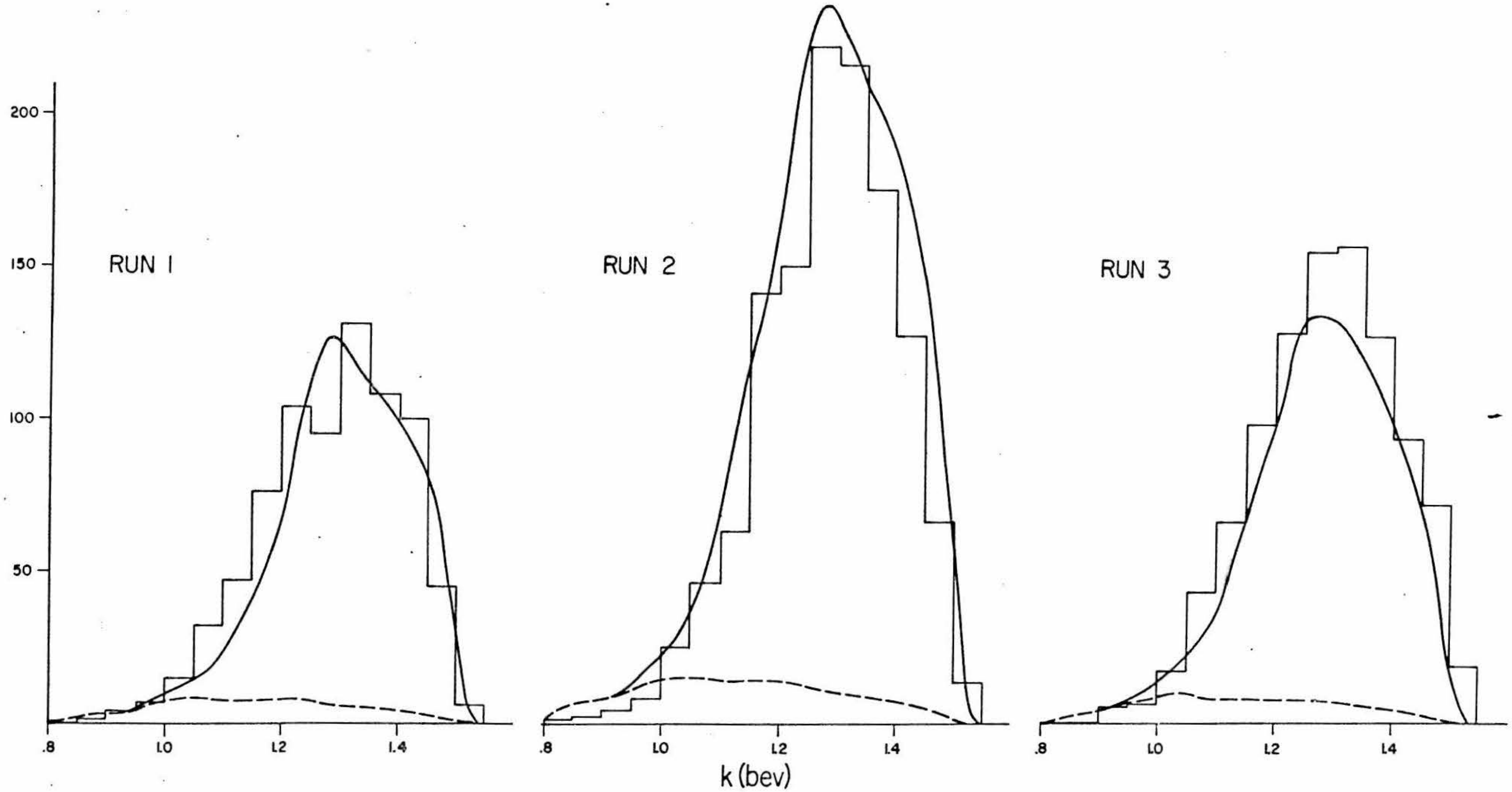

Figure 10.8

Phenomenological Model

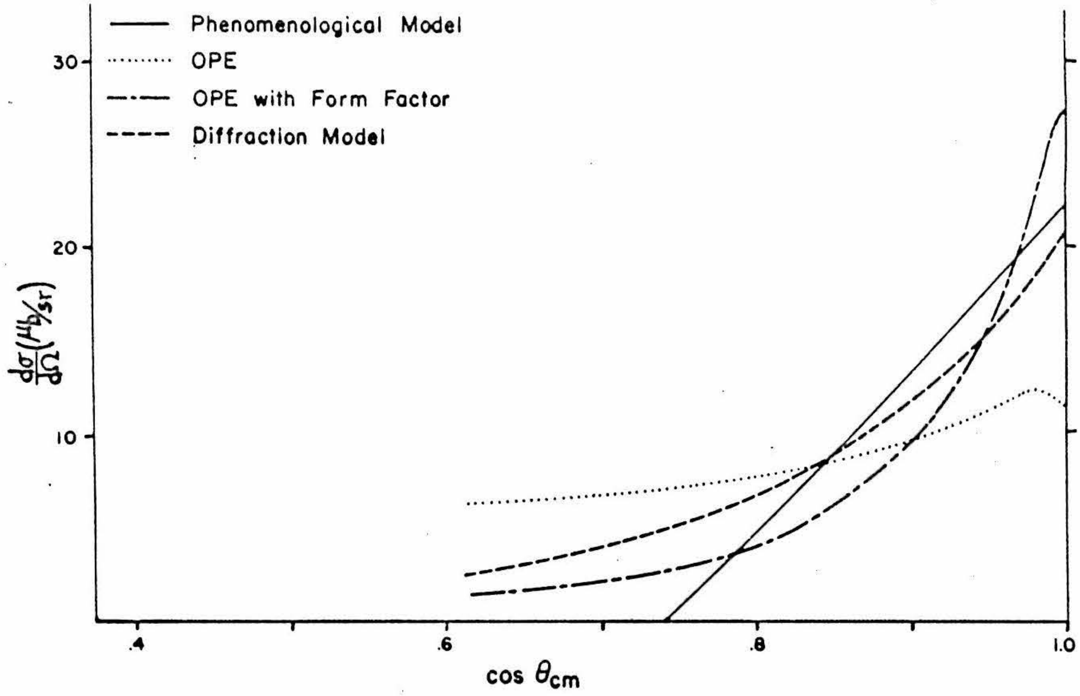
Phenomenological Model
OPE
OPE with Form Factor
Diffraction Model
30
20
10
$\frac{d\sigma}{d\Omega}$ (μb/sr)
.4
.6
.8
1.0
cos θ_{cm}

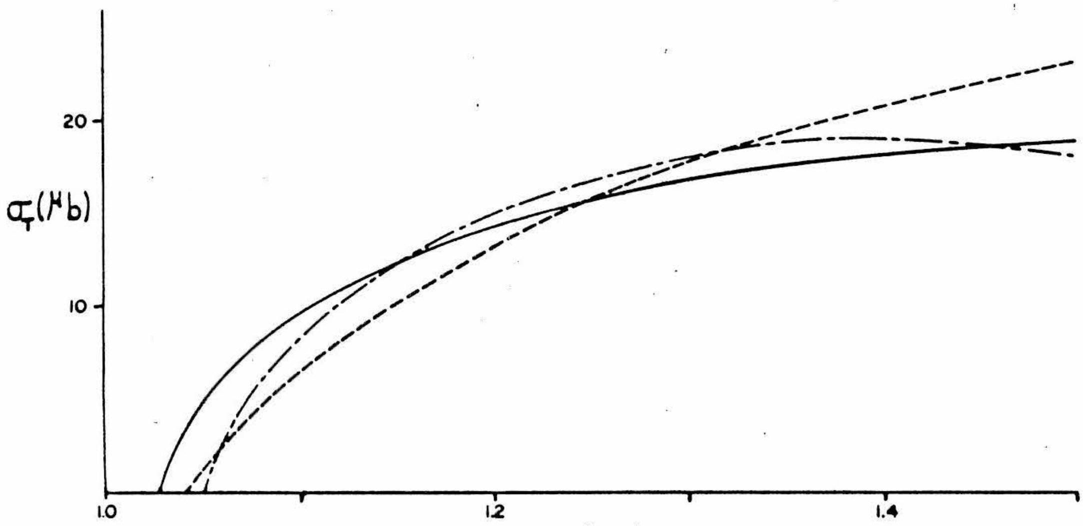
20
10
σ_T (μb)
1.0
1.2
1.4
k(bev)

Figure 11

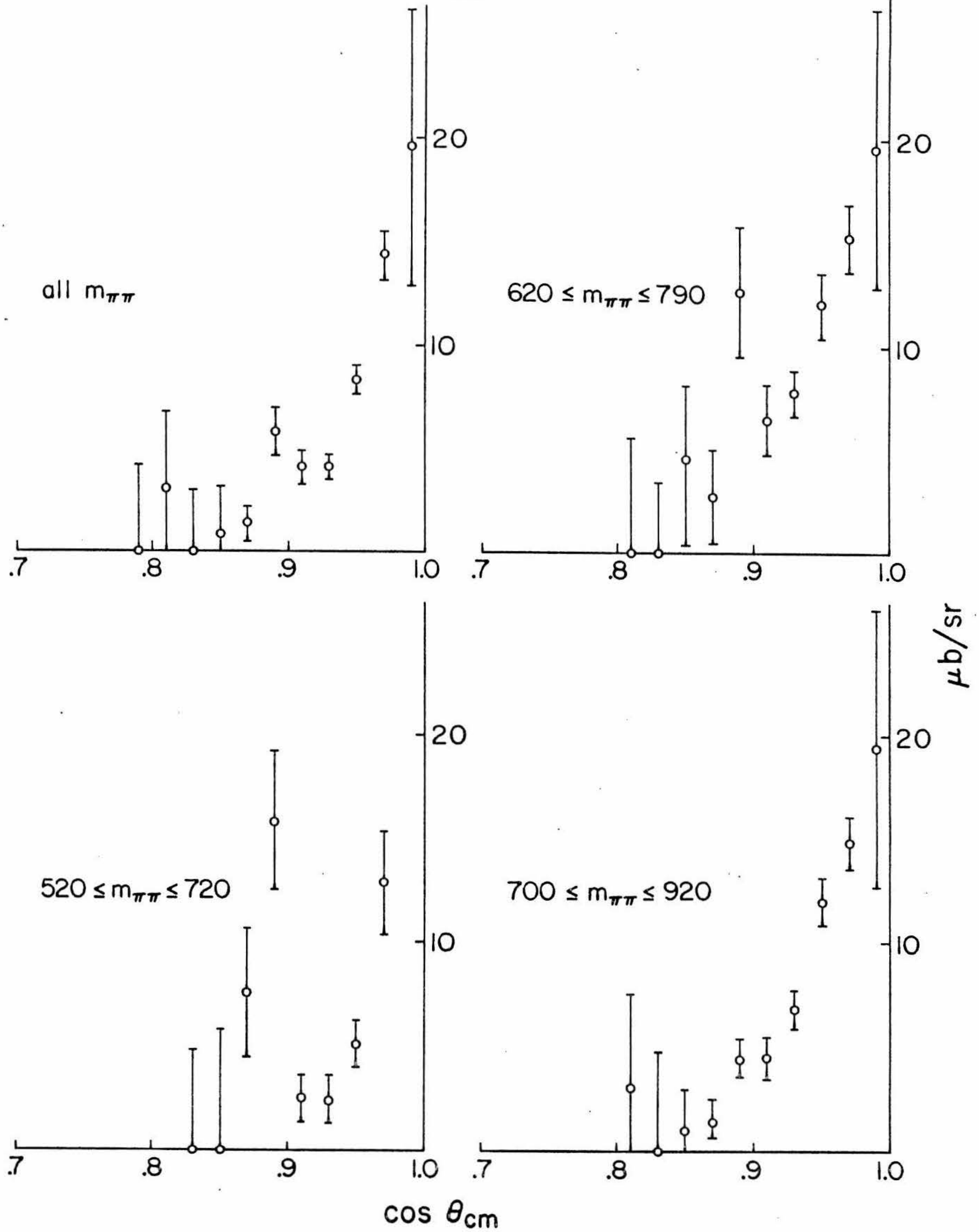
all $m_{\pi\pi}$
620 ≤ $m_{\pi\pi}$ ≤ 790
520 ≤ $m_{\pi\pi}$ ≤ 720
700 ≤ $m_{\pi\pi}$ ≤ 920
.7
.8
.9
1.0
10
20
μb/sr
cos θ_{cm}

Figure 12.1

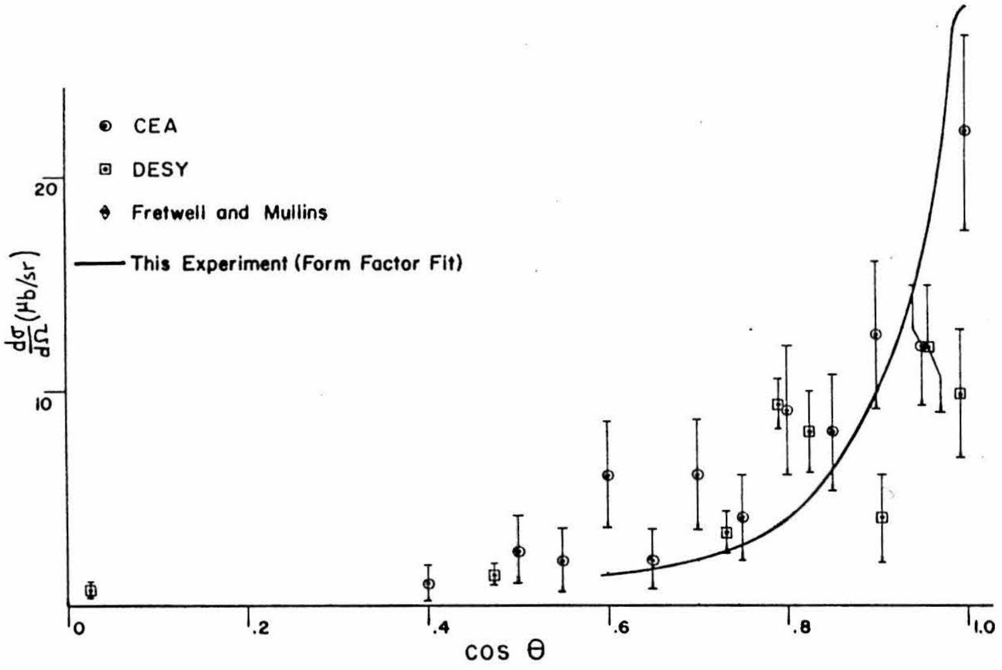

DIFFERENTIAL CROSS SECTION AT 1.4 BEV

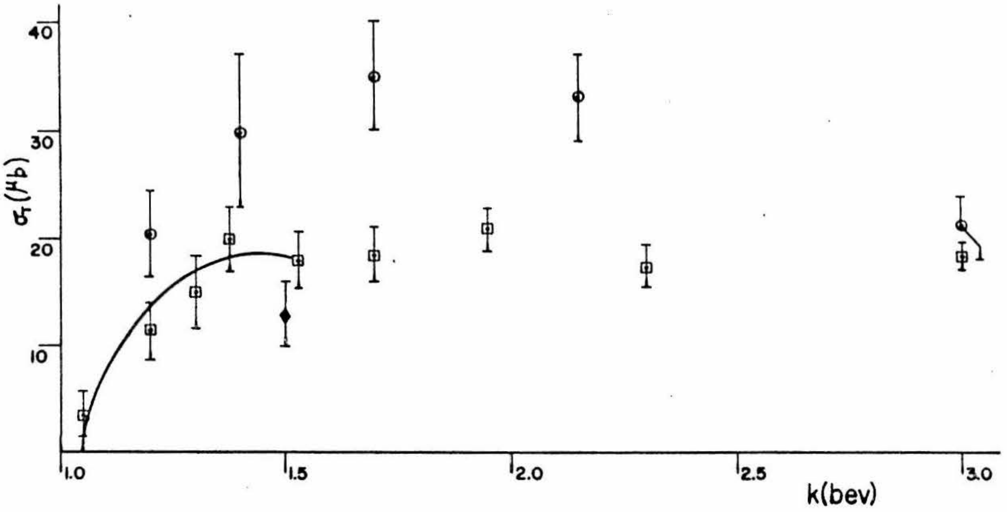

TOTAL CROSS SECTION

Figure 12.2

TABLE III

Model description	m_ρ(MeV)	Γ_o(MeV)	b_ρ	b_{ps}	extra parameters	χ^2	Prob.
OPE	738 ± 5	133 ± 7	$.90^{+.00}_{-.05}$	$0.0^{+.05}_{-.00}$	none	331	.0006
OPE (with form factor)	750 ± 6	150 ± 17	$.90^{+.00}_{-.08}$	$0^{+.06}_{-.00}$	$m_x = 266 \pm 8$ MeV	264	.345
Diffraction	743 ± 5	142 ± 10	$.90^{+.00}_{-.06}$	$.20 \pm .06$	$t_o = .956 \pm .03\ \mathrm{BeV}^2$	314	.005
Phenomenological model	737 ± 5	122 ± 11	$.77 \pm .05$	$.13 \pm .05$	$\alpha_1 = .013\ \mathrm{MeV}^{-1/2}$ $\alpha_2 = 4.1$ $\alpha_3 = .95$ $\alpha_4 = .126$	297	.033

Figure 12 compares the cross sections observed here with previous experiments. The differential cross section given by this experiment is somewhat more sharply peaked forward than observed before. However, since this experiment covered a limited range of angles at a given dipion mass and photon energy, statistical variations can strongly influence the fit to the angular dependence of the cross section. Bubble chamber experiments which cover all production angles should be considered a more reliable source of information on the differential cross section.

The total cross section given by the various fits are strikingly similar and the curve shown in Figure 12.2B represents the OPE form factor model. The ρ^o cross section from this experiment is slightly lower than observed in previous experiments, but the difference is well within the error limits. However, the amount of phase space production determined by this experiment is much less than found elsewhere. For a comparison of our phase space production with others, the significant parameter for comparison is the ratio of the ρ^o and phase space contributions to the data. CEA and DESY both find the ratio

$$b_{ps}/b_\rho \approx .9 \pm .2 .$$

Whereas we find

$$b_{ps}/b_\rho = \left\{ \begin{array}{ll} .00\,^{+.07}_{-.00} & \text{OPE model} \\ 0.0\,^{+.09}_{-.00} & \text{OPE with form factor} \\ .00\,^{+.07}_{-.00} & \text{Diffraction} \\ .14 \pm .06 & \text{Phenomenological Model .} \end{array} \right.$$

Since this experiment observed only a limited range of production angles, a slight distortion of the observed angular distribution could change the ratio b_{ps}/b_{ρ} by 5-15%. Also, since we were only sensitive to dipions which decayed more or less symmetrically, an anisotropic decay distribution for the ρ^{o} would influence the results. In particular, if the ρ^{o} decay distribution is $\sin^{2}\theta$ (see Appendix V), as expected from totally polarized ρ^{o}'s, then our total cross section for ρ^{o} production must be divided by two. Since the phase space cross section is uninfluenced by the ρ^{o} decay distribution, the ratio b_{ps}/b_{ρ} would then increase by a factor of two. Also, there is no reason to require that the background production of dipions behave exactly like phase space. If the background produces fewer events in the forward direction ($\cos\theta_{cm} \approx 1$) than phase space, then we would expect to observe a negligible background contribution in the interval of $\cos\theta_{cm}$ to which we were sensitive.

The OPE model gives a total cross section which is a factor of two higher than any of the other models, so the value $\Gamma_{\rho\pi\gamma} = .12$ MeV deduced from the OPE fit is quite meaningless. Assuming the form factor factor model introduces a factor

$$\left(\frac{g_{\pi x}\, m_{x}^{2}}{t + m_{x}^{2}}\right)^{2}$$

into the differential cross section, we find

$$\Gamma_{\rho\pi\gamma}\, g_{\pi x}^{2} = 1.07 \text{ MeV} .$$

Also, by looking at Figure 12.1 we note that the data prefer a differential section which is quite peaked in the forward direction.

This makes the OPE model fit badly, whereas the other models have adjustable parameters to allow for a sharply peaked angular distribution.

In conclusion, the major difficulties encountered in interpreting this experiment are due to the limited kinematic regions which were observed. In particular, many more experimental configurations could have covered a larger range of production angles, ρ^0 decay angles, and photon energy-dipion mass values. Future experiments along these lines would prove very interesting. The Caltech synchrotron is very well suited for an investigation of ρ^0 photoproduction near threshold, and more conclusive information on the production angular distribution, ρ^0 decay distribution, and the existence of interference effects between various production amplitudes would be invaluable.

APPENDIX I

Description of the Apparatus

A. Spark Chambers

The spark chamber characteristics which directly affect the results are the single track detection efficiency, the multiple track efficiency, and the time dependence of the efficiencies. The details of the spark chamber construction and triggering are similar to previous experiments, so they will not be discussed here.

The detection of the track produced by a single particle depended on both the "delay time" (the time between the creation of the ions in the chamber gaps and the appearance of the high voltage between the chamber plates) and the "sweep voltage" (a low D. C. voltage which "swept" the ion pairs into the plates in the absence of a high voltage pulse). Figure 13 shows the detection efficiency vs delay time for various sweep voltages. During the experiment, the sweep voltage was 70 V., which provided a delay time interval of 1.6 μs before the efficiency dropped to 50%. Since the normal delay time due to the electronics and signal cabling was 200 ns, the efficiency for detecting the particle responsible for triggering the electronics was 99% (in the absence of competing tracks).

The multiple track efficiency is not well known. However, the probability that a particle in the proton thin foil chambers would be missed is discussed in section B. 6 below. It should be noted that the proton thin foil chambers experienced by

Figure 13

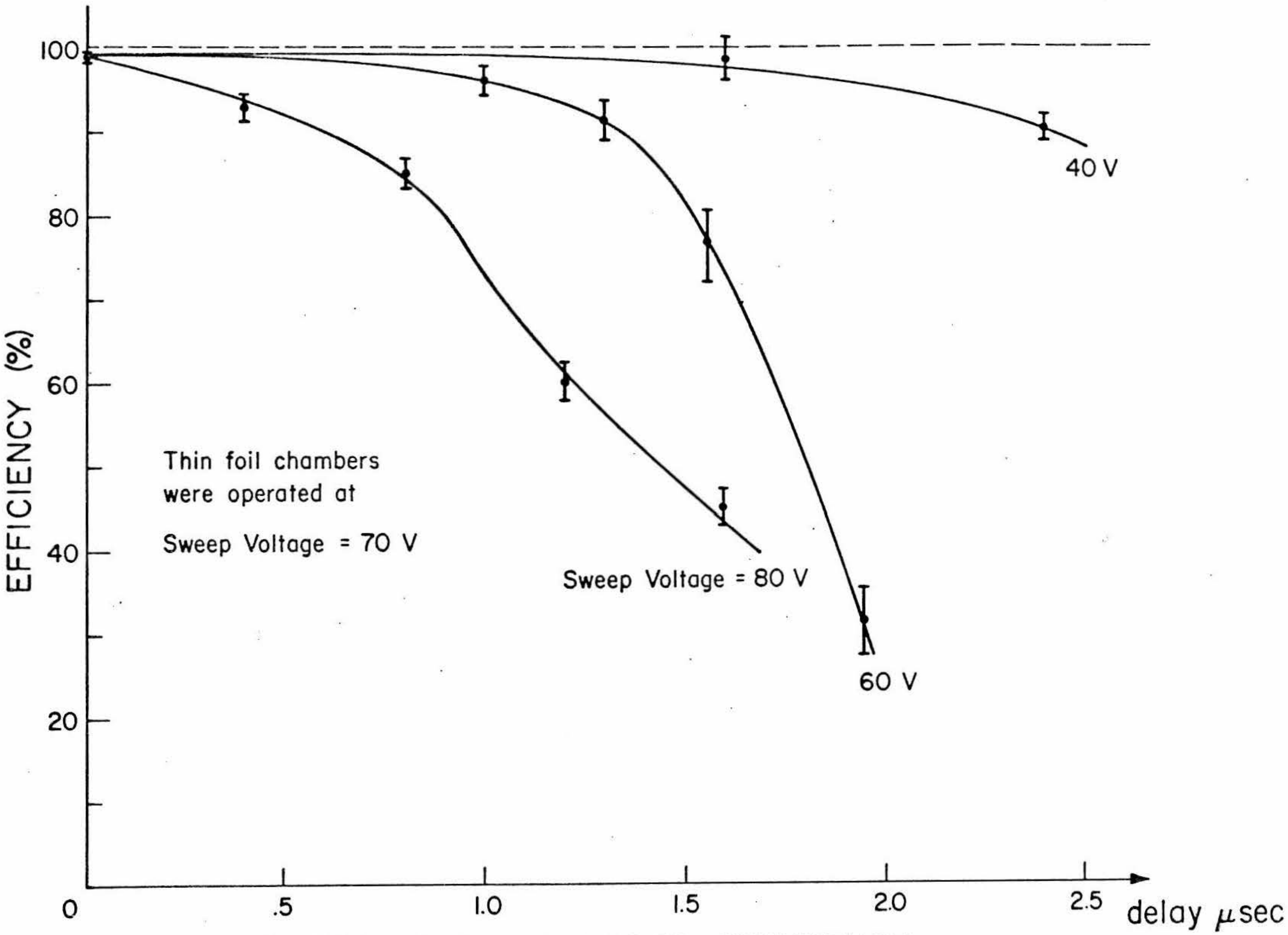

TYPICAL SPARK CHAMBER EFFICIENCY

far the largest particle flux. Using Table IV as an indication of the particle fluxes in the various chambers, the multiple track correction for the pion chambers is negligible.

The performance of the triggering circuits and the gas flow through the chambers was monitored regularly throughout the experiment and caused no difficulty.

B. Electronics

1. Spark Chamber Triggering Logic

The general features of the spark chamber triggering logic are discussed in section II. A, except for the specifics of setting the biases on the discriminators D1 and D2 (see Figure 3). The function of D1 was to prohibit lower mass particles which stopped in or before the first range chamber from triggering a frame, and thereby to reduce the number of unwanted frames in the film. The bias on D1 rejected 1% of the protons and 95% of the pions which stopped in the back of the first range chamber, and rejected none of the protons and 50% of the pions which stopped in the front of the first range chamber. The function of discriminator D2 was to perform a similar role for particles which stopped in the second range chamber. The bias on D2 rejected an average of 1/2% of the protons and 50% of the pions in this range. However, the computer analysis requirements on the agreement between the pulses and particle range provided a far better discrimination against pions (see subsection 2 below).

These biases were checked regularly during the experiment and were found to be very stable.

2. Rejection of Pions Entering the Proton Telescope

Figure 14 shows the expected pulse heights from pions and protons stopping in the proton telescope. There are two processes which might allow a pion to satisfy the overall proton requirements. First, the normal fluctuations in counter gains, mismeasurement of pulses, and fluctuations in ionization loss could be a source of trouble. But since the fluctuations in counters P1 and P2 were independent, the probability of satisfying the PULCHI criterion in the analysis is less than 1/2% at any energy. Second, the pion can make a nuclear interaction in a counter or a range chamber. Pions which make an interaction in a range chamber have pulses which are even lower than expected for normal pions of the same range, so this effect has even less influence than the normal fluctuations described above. Those which make a nuclear interaction in a counter, however, have a much greater opportunity for mischief. Calculations of this process were made and the final probability for a pion satisfying the proton requirements is shown in Figure 15.

There are additional constraints from the analysis which suppress the pion contamination further. First, the kinematic constraint on the particle angles and the observed heavy chamber range causes events in which a pion and proton are interchanged to have somewhat less than a 10% chance of being accepted, regardless of the pulse requirements. Second, if the event is an

Figure 14

The two left-hand graphs refer to particles which stopped in a range chamber. For these two graphs, the dashed lines are the upper and lower limits imposed by PULCHI. The dot-dashed lines are the limits imposed by the analysis program. (The dot-dashed lines are also indicative of the pulse height above which one expects only 1% of the pions.)

The right-hand graph refers to particles which stopped before the first range chamber. The dotted lines again indicate the limits imposed by PULCHI, and the dot-dashed line indicates the lower limit on the pulses allowed by the analysis program. Also shown is the energy E_T associated with the pulses in the regions allowed by PULCHI.

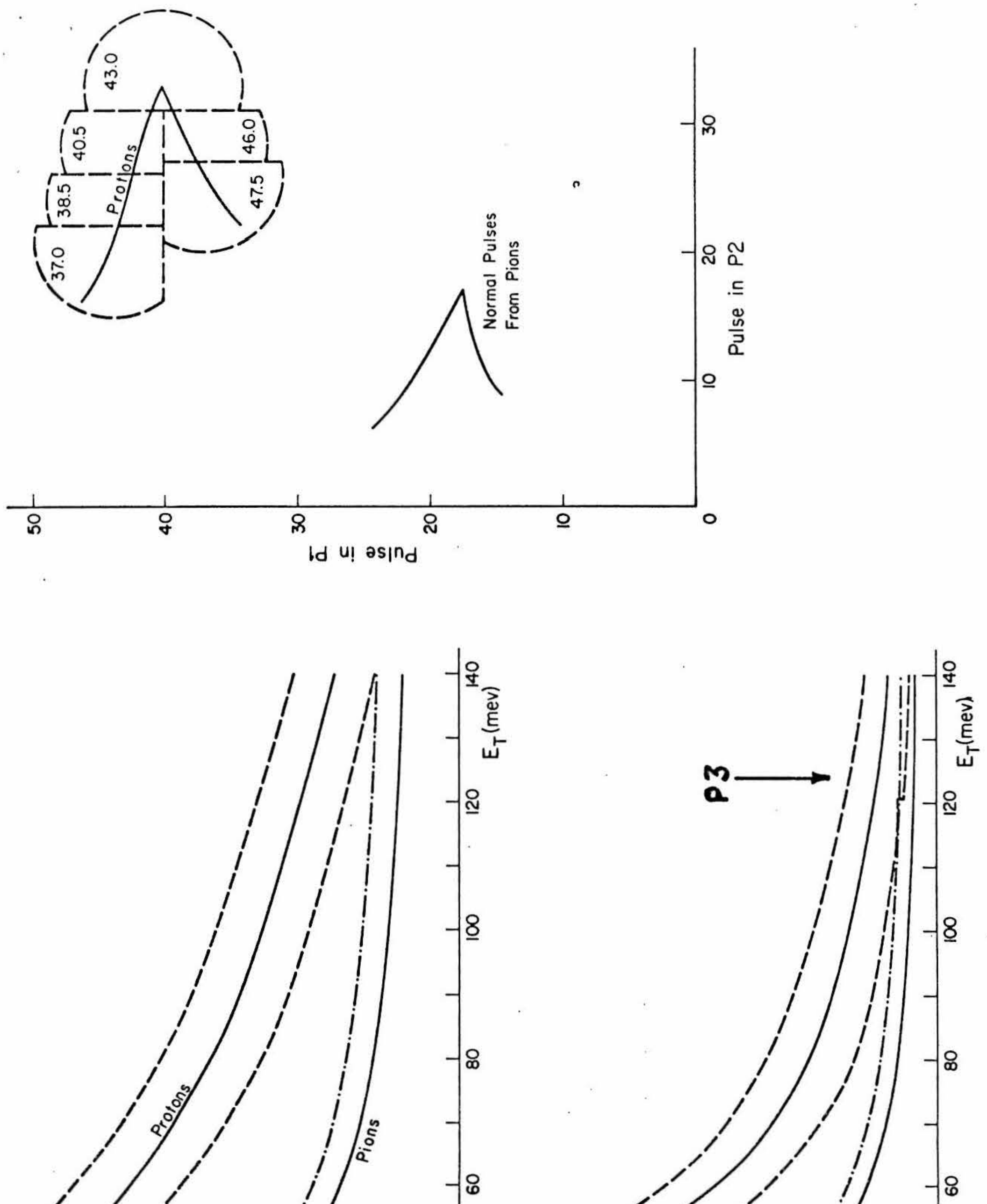
37.0
38.5
40.5
43.0
46.0
47.5
Protons
Normal Pulses From Pions
Pulse in P1
0
10
20
30
40
50
Pulse in P2
Protons
Pions
Pulse in Counter P1
Pulse in Counter P2
E_T (mev)
50
60
80
100
120
140
P3

Figure 14

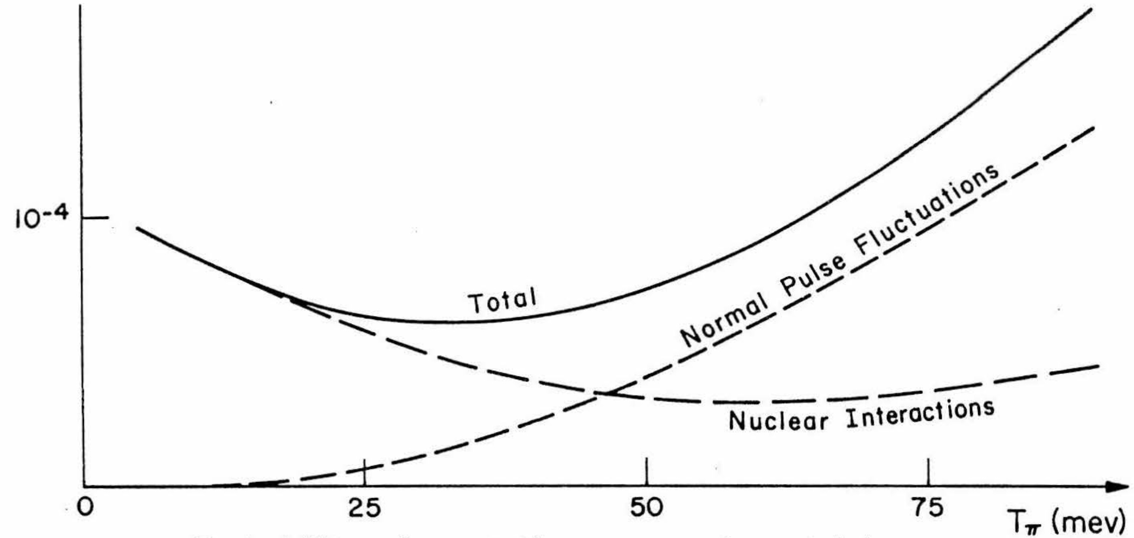

Probability of accepting an event containing a π in the proton telescope

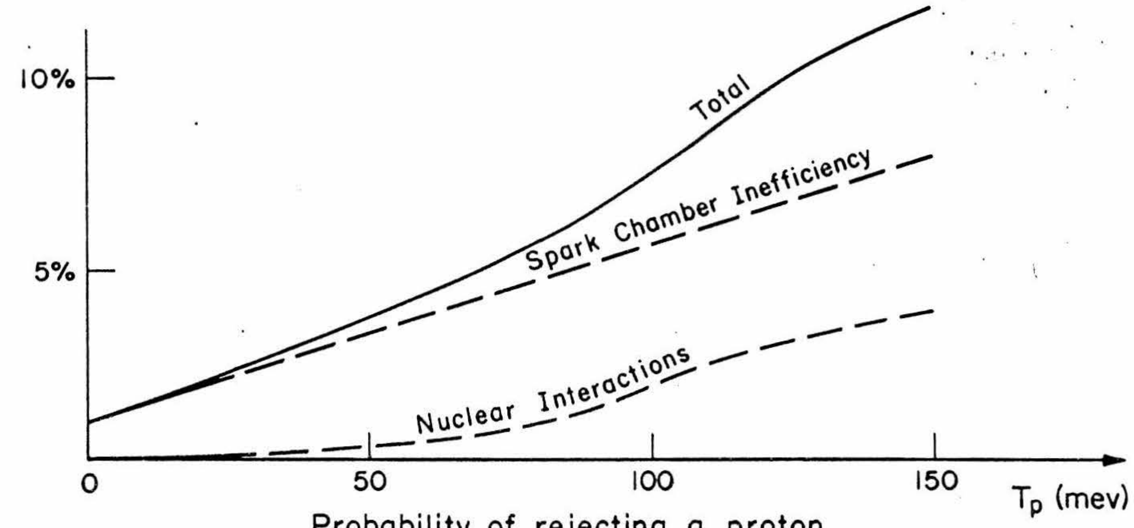

Probability of rejecting a proton

Figure 15

accidental, the results from Appendix III.D show that it has only a 3% chance of acceptance. The final probability that an acceptable event had a pion in the proton telescope is shown in Figure 11.5, and it is seen to be much smaller than other backgrounds.

3. Monitoring Phototube Gains

A radioactive B_i^{207} source, mounted on each counter, provided a source of decay electrons which when stopped in the counter gave the approximate pulse-height spectrum shown in Figure 16. Also shown in Figure 16 is a simplified logic diagram for monitoring the pulse spectrum. The discriminator D was set to the "expected peak" of the source spectrum for the phototube being tested, and the counting rate was compared with an appropriate "expected counting rate". The phototube gain was then reset to within 1% of its standard value.

The gains of the phototubes on counters P2 and P4 were monitored continuously, while the rest of the phototubes were checked three to four times per day. Thus there is no observable drift in the pulses from P2 and P4, but other phototubes had frequently drifted by several percent between checks. Only gain changes in counter P1 affected the final results, and these changes simply introduced an additional spread into the range vs. pulse-height curve for counter P1, which was equal to the measuring error on the pulse height.

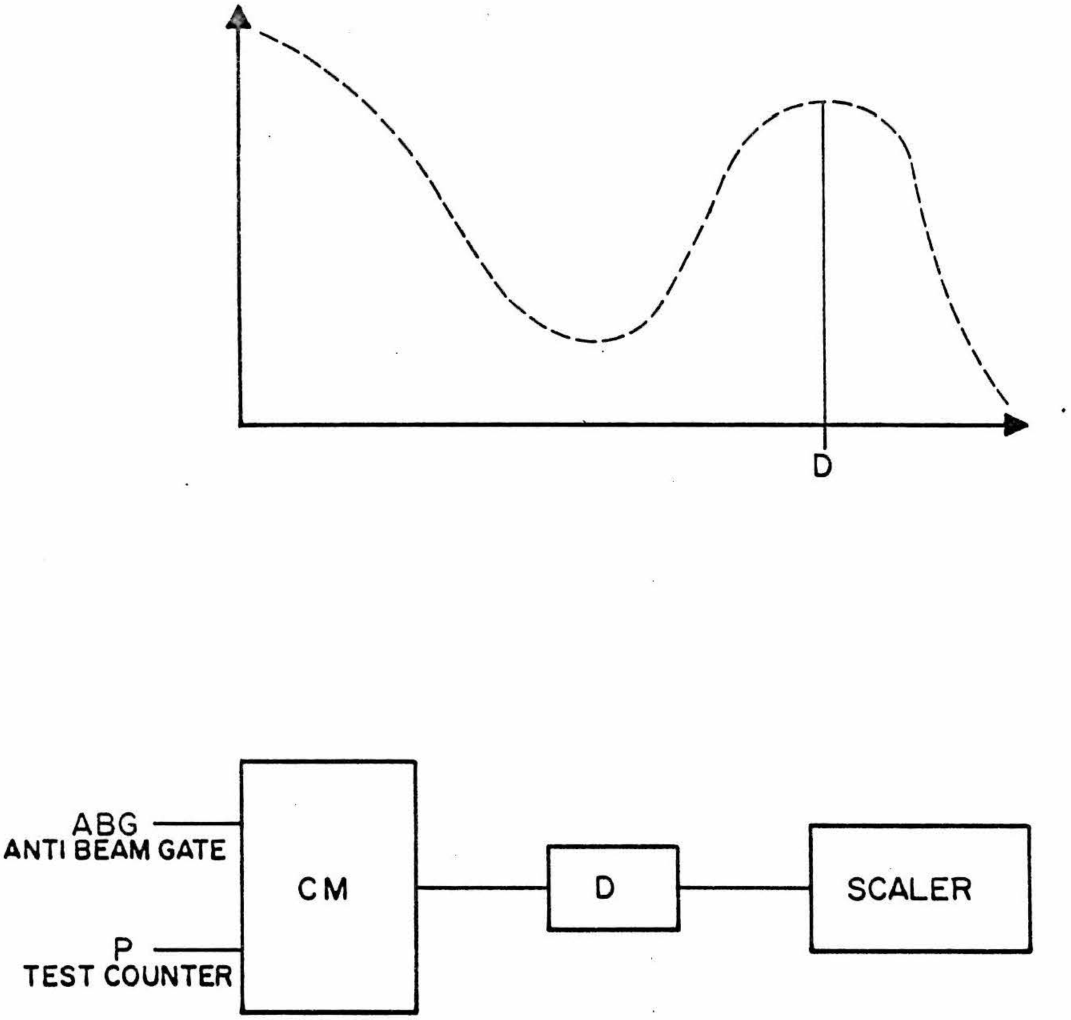

Figure 16

4. Oscilloscope Display and Calibration

Figure 17 shows typical scope pictures for the different triggering possibilities shown in Figure 3. For each event, there are two separate traces - a normal and an attenuated trace. Since certain amplifiers were saturating badly when the original pulse was larger than 1.5 cm on the scope screen, the lower attenuated trace was used to display the pulses attenuated by a factor of six. Also, since the pulse height from P1 was considered only useful for low energy protons, it was only put into the attenuated trace for an LD1 or LD2 trigger. The pulse from P2 (or P4 in the case of an LD3 trigger) was "integrated" over about 30 ns and displayed immediately following the original pulse. The original pulse showed whether there was an accidental pulse present which helped the event satisfy the discrimination biases, while the integrated pulse was used as a more accurate indication of the energy loss in the counter.

At regular intervals during the experiment, standard pulses were fed through the electronics to calibrate the oscilloscope screen. These provide a constant monitor on the complete electronics from the counters P1, P2, and P4 to the oscilloscope.

5. Beam Watcher and Ion Chamber Gate

Several very useful instruments were developed by Joe Mullins for use in this experiment. The first was a beam watcher which sensed the internal synchrotron beam,

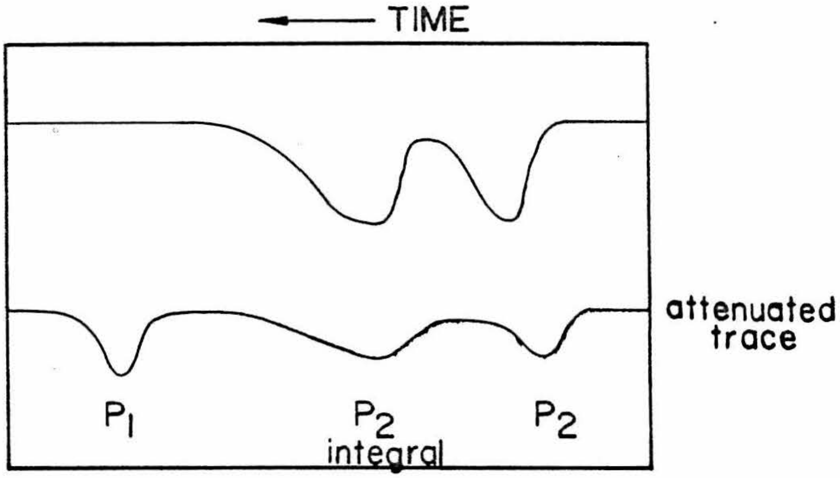

LD1 or LD2 trigger

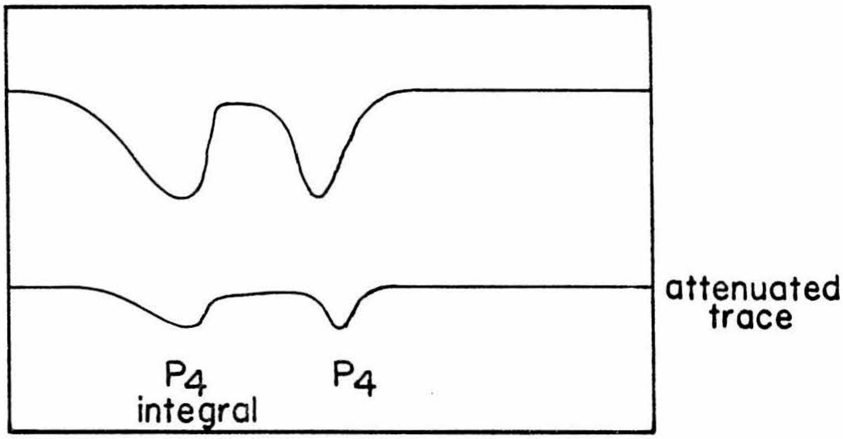

LD3 trigger

REPRESENTATIVE OSCILLOSCOPE FRAMES

Figure 17

and gated off our electronics when the beam was too large. This allowed us to run at reasonable beam intensities while avoiding the high accidental rates which accompany large beam spills. The second was a fast gate on the quantameter. After the electronics were triggered, the experiment could not accept another event until the next synchrotron pulse, so the energy dumped into the quantameter after triggering would not be part of the "usable total energy". The quantameter gate stopped integrating the beam energy within 10 ms after a trigger.

6. Counting Rate Problems

The particle fluxes present in the counters and spark chambers provided a variety of ways of contaminating a frame. The counting rates in certain sections of the logic are shown in Table IV.

First, the frame may have been triggered by an accidental coincidence between particles from two or more separate interactions in the target. Allied to this problem is the possible presence of more than one track in a thin chamber, in which case it is obvious that some track combinations must represent accidental events. On the average, there were 1.6 different events (combinations with one track selected from each thin chamber) in a typical frame. These were treated in the same manner as electronic accidentals, and the correction of the data for these effects is discussed in Appendix III. D.

Second, an accidental track may have effectively robbed available energy from a good track, causing the event to either be rejected or to yield a different result.

Table IV

Run	P1	$(P1 \cdot P2)^*$	$(\pi_1 \cdot \pi_2)$	C_π	$(P1B \cdot P2B)^*$
1	7×10^6/sec	1.4×10^6/sec	10×10^3/sec	60/sec	$.4\times10^6$/sec
2	8	1.6	10	60/sec	.8
3	9	1.6	9	60/sec	.6

*(P1B · P2B) refers to coincidences between P1 and P2 with pulses large enough to satisfy $C_\pi 1$ (see Figure 3).

(P1 · P2) refers to all coincidences between P1 and P2.

This effect should have been most prominent in the proton thin plate-chambers - especially the front one. For this purpose, a series of special frames were taken in which the spark chambers were triggered by particles in the proton telescope. By varying the pulse requirements for triggering, the efficiency of these chambers for detecting protons of various energies was determined, and the correction to the results is shown in Figure 15.

Finally, an accidental pulse may have been present in the scope display, causing the computer analysis to reject that frame. This amounted to 6%, 5%, and 5% in the first, second, and third experimental setups respectively.

APPENDIX II

A. Oscilloscope Film

The measurement and classification of the traces on the scope film was done using a Rekordak overhead projector, which projected the film image onto a formica table. First, the projector focus was adjusted so the image of the main graticule on the oscilloscope was a standard size, thus giving subsequent measurements an absolute calibration.

A computer program generated forms containing a frame number and spaces for the following information from each frame.

1. A COMMENT which described whether the frame contained a) no usable information, b) an accidental pulse or an extra hump on the trace, c) a normal uncontaminated trace. If the frame contained no useful information the scanner proceeded to the next frame.
2. A TYPE which indicated whether the pulses were from an LD1, LD2, or LD3 trigger. Representative normal traces for both types are shown in Figure 17.
3. Pulse-height measurements of all signals and their integrals made using a movable template. If a pulse (or integral) on the unattenuated trace was larger than 2 cm on the graticule, it was not measured because of the deflection limitations of the oscilloscope.

The final function of the scope measurements was to give information to the spark chamber film scanners for use in rejecting certain events. Before the spark chamber scanning of a new setup was started, a correlation was made to determine an acceptable relationship between the pulses and the observed particle range in the proton telescope. A bias, called MINSTØP, was then generated, which was the minimum range of a proton telescope track allowed to be associated with the measured pulse heights for that event. This criterion was used in the spark chamber film scanning to reduce the pion contamination and therefore to reduce the number of events to be measured. All this measured information was put on disc storage in the computing center and was available for use in the analysis of events.

A check on the efficiency of the scope scanning operation was performed by remeasuring a 10% sample of completed events. It was found that 10% of the time, the scan and rescan disagree in such a way as to change the result for that event when put through the entire analysis. Since the scope film was scanned only once, it was assumed that the original scan and the rescan had the same efficiency which was 95% ± 2%.

B. Spark Chamber Film

The spark chamber film handling was divided into two main categories. First was the preliminary scanning to determine which frames should be measured on the ITEK digitized measuring machines. Second was the actual measurement of these selected events.

The purpose of the preliminary scanning was to separate the events into three categories - good, questionable, and bad. The requirements for a good event were

1. Using a pivotable line and considering only the top views of the thin chambers, there had to be at least one set of three tracks (one track from each telescope) which shared a common origin. To allow for expected multiple scattering, this common origin could be anywhere within a region three times the size of the real hydrogen target, and using this origin, the track in the rear chamber of a telescope was allowed to be 2 cm in real space from the line drawn through the origin and the track in the front thin chamber. Since multiple-scattering could account for 3 mm r.m.s. deviation, this requirement had a negligible influence on rejecting good events.

2. Using a template which correlated the side views of each pion telescope, it was required that in the side view, each pion track extrapolated back to within ± 5 cm vertically of the center line of the hydrogen target. This had the virtue of rejecting many of the extra track candidates.

3. The heavy chamber track (if any) associated with a possible pair of candidates in the proton thin chambers had to have a range greater than the MINST0P requirements imposed by the scope pulse measurements (see Section III).

4. A valid candidate in a thin chamber had to have at least two sparks. A candidate with only one spark could not be used to classify the event as "good".

The requirements for a questionable event were the same as those for a good event, with the following relaxations:

1. The common track origin could be in a region four (instead of three) times the actual target size.
2. The extrapolated side views of the pion tracks could come ± 8 cm (instead of 5 cm) vertically from the center line of the target.
3. A track in a thin chamber might have only one spark if its partner in the same telescope had at least two sparks.
4. The front proton thin chamber could have no track if the rear proton thin chamber had a good track and there was a track in the heavy plate chamber which was associated with the track in PTF2.

Any questionable character associated with the event sufficed to classify the event as questionable.

Any event which failed to satisfy the requirements for either a good or a questionable event, was classified "bad".

A few comments about the heavy chambers would be useful here. First, the existence or absence of a track in the range chambers has no influence on the preliminary classification of an event except through the MINSTØP criterion and the few events which fell under Section 4 of the questionable event requirements.

Second, to be considered as part of the event, a heavy chamber track had to line up with a candidate from the thin chambers to ± 2 cm at the entrance to the first heavy chamber. (This was equivalent to three times the worst r. m. s. deviation of a track due to multiple scattering.) Finally, the heavy chamber track had to start before the fourth gap of the first heavy chamber. Since the efficiency of each of the first three gaps was better than 80%, this requirement alone rejected about 92% of gammas and 96% of the neutrons entering counter P1 but rejected less than 1% of the protons.

The following procedure was devised to get an accurate classification of the events in the preliminary scanning. Each event on the spark chamber film was scanned by two different scanners. If they agreed on the classification, no further scans of that event were required, but if they disagreed, then two more independent scans were done. If the last two scans agreed, then that frame was complete, but if there still was no agreement, then a fifth scan was done (by the most reliable scanner) and its result was law. From these results, lists were generated containing the events which were to be measured. During this whole process, all information about the scanning status of an event was available on disc storage in the computing center, so in particular, we know that the scanning of all the frames was completed.

A check on scanning efficiencies was performed by having each scanner rescan part of a uniformly selected 10% sample of already completed events. Since scanning efficiencies were high (all over 89%), and since the original classification was the result of at least two independent scans, the original classification was assumed to be correct and any disagreement was attributed to the rescanner. An examination of the scanning history of finally accepted events indicates that there is a 2.1% - 1.2% chance of a good event being rejected at the scanning level. The final correction factor on the results due to scanning inefficiency was taken to be 1.8%.

C. Measuring of Spark Chamber Film

The measuring of spark chamber film was done on two ITEK Model 1800 digitized image plane projection machines. The film image was projected, via a lens and mirror system, onto the back of a ground glass plate which was 36" x 36" for machine 1 and 24" x 24" for machine 2. An illuminated cross could be positioned over any desired point on the projected image, and by pressing a foot pedal, the x-y coordinates of the cross were punched to four significant figures on an IBM data card. This was done by using a Datex decoder to translate the output of the x and y axis encoders into signals appropriate for the IBM Model 526 summary punch. A set of parameters (frame number, scanner number, run number, and a code) were punched at the beginning of a card, and a card counter punched a card number in the last two columns of the card for each frame. This latter information was essential to ensure that the order of the cards was preserved throughout the data handling.

Calibration of the measuring machines.

In order to monitor and correct for the distortions in the projection system, measurements of a calibration plate were made at regular intervals. The calibration plate was a glass slide containing a grid of accurately spaced crosses. This plate was inserted in the projector and the scanner measured the positions of the fiducial marks eight times each, and also measured the position of a "fixed fiducial" scribed on the ground glass screen of the ITEK. Using these measurements, a set of parameters a_{jk} and b_{jk} were generated by making a least squares fit between the measurements and the formulae

$$x = \sum_{j=0}^{3} \sum_{k=0}^{j} a_{jk} (x - x_o)^k (y - y_o)^{j-k}$$

$$y = \sum_{j=0}^{3} \sum_{k=0}^{j} b_{jk} (x - x_o)^k (y - y_o)^{j-k} \quad .$$

In this way, an "undistorted position" (x, y) was associated with the point whose measured position was (x_m, y_m). The goodness of fit (χ^2) was required to be satisfactory, and also the most recent measurements had to fit reasonably well to a set of "standard parameters". Whenever there was a significant realignment of a machine, its "standard parameters" were redetermined by a new calibration, but in the absence of any major occurrences, the lack of a fit between a recent calibration and the standard had to be explained. For example, it was very useful for detecting faults in a machine such as loose parts etc. The "standardization" of a measured spark chamber frame was always done using the most recent acceptable calibration, and in this way, long term variations in the calibration were taken into account.

The actual measurement of a spark chamber frame proceeded as follows:

1. The scanner entered the relevant parameters on the parameter board. These would be punched in columns 1-14 of every card of that event.
2. The scanner marked with a felt pen, those tracks which were to be measured in each chamber. This also served the dual purpose of allowing the film to reach more of an equilibrium in thermal expansion. The film seemed to expand with a time constant of about 2 minutes, so spending 2 minutes on this section got most of the expansion out of the way.
3. Then the "main fiducials" were measured eight times each. These were crosses epoxied to cement blocks surrounding the experiment and illuminated by argon lamps. Their positions relative to the experimental apparatus were found to be stable throughout each run. When all four main fiducials were visible on the film, a consistency check was required between the corrected positions of the fiducials (corrected using

calibration plate data described above). During a large part of RUN 3, the fourth main fiducial was not visible so this check was not available on that portion of the film. The eight measurements of every main fiducial were allowed to have a spread of 1/2 mm in real space. If one or more of the eight fiducial measurements was farther than 1/2 mm from the average position, then the measurement with the largest deviation was ignored and the seven remaining measurements were checked. If after rejecting individual measurements in this way, there were five or less measurements of a fiducial left, then the event was considered mismeasured and was required to be measured again.

4. Next, the position of all relevant sparks in the thin chambers was measured in a prescribed order. Up to three "candidates" were allowed in each thin chamber (a candidate being a set of sparks which had been marked as described in Section 2). The top and side views of each candidate were required to have sparks in identical gaps, i. e., they must "look identical", or else the event was tagged for remeasurement. In the analysis program, if two or more candidates in the same thin chamber "looked the same", then all combinations of top and side views were tried in reconstructing the space position of the sparks. Many of these combinations produced absurd tracks, but

this precaution was infinitely safer than trusting the scanner to make the correct pairing of top and side views for candidates with the same gap character.

5. The four main fiducials were remeasured again exactly as described in Section 3 above. The average position of each fiducial was required to be the same, to within 1/2 mm in real space, as the initial set of measurements from Section 3 , or else the event was rejected and slated for remeasurement. Measuring the main fiducials immediately after measuring the thin chamber sparks served the purpose of checking for film creeping, and minimizing the influence of film expansion and creeping on the position of the thin chamber sparks. Using the averaged positions of the four main fiducials, an absolute coordinate system was established on the film. In particular, the position and orientation of all spark chamber plates and the location of the logic lights (see Section 7 below) were known in this coordinate system, and were independent of the orientation or expansion of the film during the measurement of a frame. This was used to determine the gap locations of all sparks and to check that the gap location of the top and side views of a spark were the same (see Section 4 above). The effect of measuring errors in the fiducials could produce at most a .2 mm systematic error in the reconstructed space position of all sparks, and would have an undetectable influence on the results for that event.

6. The track (if any) in the heavy plate chambers was now measured. This track had to start in one of the first three gaps in the first chamber and had to line up with a previously measured set of thin chamber tracks to within 2 cm in real space. For tracks which stopped in the first heavy chamber, the scanner measured the first spark, a spark somewhere in the middle, and the last two sparks of the range. If the track had a bend of more than 5^o, a spark near this bend was measured instead of a spark somewhere in the middle of the track, but if the track went less than 1/3 the length of the chamber (i. e., $T_p < 80$ MeV) then no spark was measured in the middle (just the first spark and the last two sparks were measured). If the range extended beyond the first heavy chamber, then for each chamber traversed the scanner measured the first spark, a spark in the middle, and the last spark of the track in that chamber. In this way we could tell if the tracks in successive chambers were really related to each other, i. e., if they lined up. The reason for measuring a spark somewhere in the middle of the length of a track in a chamber is mainly historical. If one wanted to get information about the proton polarization, then one could use these measurements and add a section to the analysis which determined the direction of scattering of a track, but this was not done here.

7. Finally, the scanner measured the position of three "logic lights". These were three pairs of lights (only one of each pair being on at a time) which were driven by three flip-flops and indicated which section of the electronic logic was responsible for triggering that event. Agreement was then required between the measured range and the information as to which logic lights were on. The measurement of each logic light had to be within 3 mm of the expected position (to eliminate the possibility of measuring a random speck on the film), and one and only one of the lights from each flip-flop was required.

APPENDIX III

Analysis Procedures and Tests

A. Track Probability Function Φ_k

Given an origin $\hat{x}_o$, and an initial particle momentum $\hat{p}$, the probability that the sparks produced by this particle will be measured at $\hat{m}_j$ will be derived. (The subscript j describes the gap location of a spark.) First, we will consider a particle starting from $\hat{x}_o = 0$ with initial momentum along the z axis ($\hat{p} = p\hat{e}_z$), and will derive the probability density for measuring sparks at $\hat{m}_j$. Then the results will be generalized to arbitrary $\hat{x}_o$ and $\hat{p}$.

For a particle with its initial momentum along the z axis, the two processes responsible for deviations of sparks from the z axis are the multiple scattering in materials along its path and the mismeasurement of spark positions by the scanners. Since there is no correlation between the projection of the sparks onto the x - z and y - z planes, we can start by considering the x - z plane alone. The problem is subdivided further. First determine the probability that the particle followed the dashed trajectory shown in Figure 18 (subsection 1 below). Second, assuming the particle followed the trajectory in Figure 18, determine the probability that the n_1 sparks in the first thin plate chamber were measured at $\hat{m}_j$ ($j = 1..n_1$) and that the n_2 sparks in the second chamber were measured at $\hat{m}_j$ ($j = 5.., 4 + n_2$) (see subsection B below). Finally, since we have no information except the measured spark positions, we must integrate over our ignorance of what the real x_1, θ_1, x_2, and θ_2 were (see subsection 3 below).

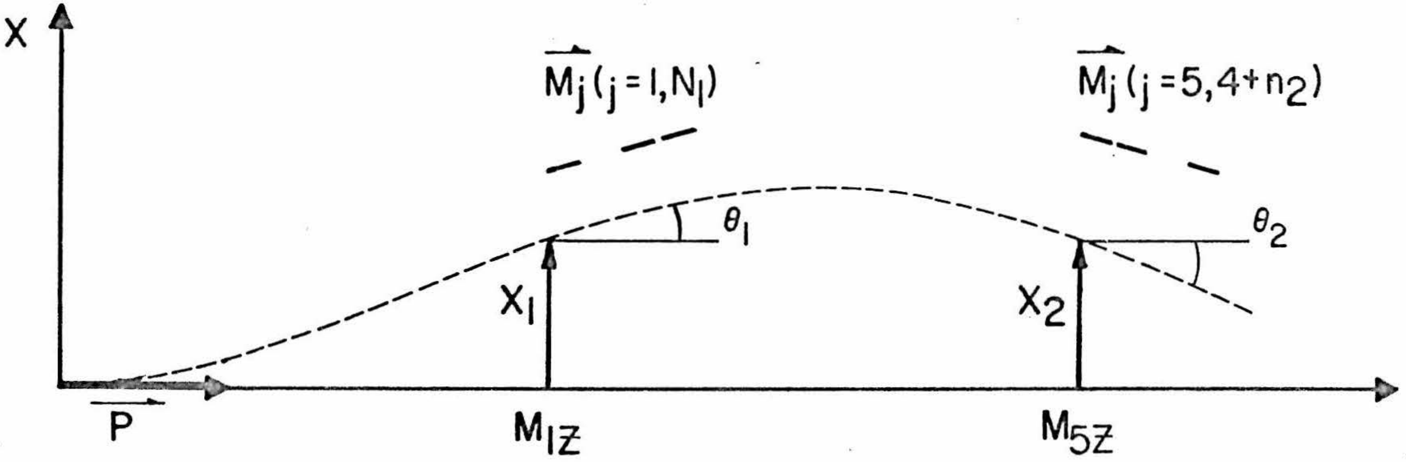
X
$\overrightarrow{M_j}(j=1,N_1)$
$\overrightarrow{M_j}(j=5,4+n_2)$
θ_1
θ_2
X_1
X_2
$\overrightarrow{P}$
M_{1Z}
M_{5Z}

Figure 18

1) It has been shown(45) that the distribution function in x_1 and θ_1 for a particle which has travelled a distance z in a homogeneous material with radiation length L_o is

$$P(x_1, \theta_1) = \exp(-g_1) \qquad (1)$$

where

$$g_1 = \frac{4}{Tz}(\theta_1^2 \; 0 \; 3\theta_1 \frac{x_1}{z} + 3(\frac{x_1}{z})^2)$$

$$T = (\frac{20 \text{ mev}}{p\beta})^2 \frac{1}{L_o} .$$

It is shown in Appendix I. 2 that if the particle traverses various materials with different thicknesses and radiation lengths, the distribution function can be written as in (1) with

$$g_1 = 4(f_1\theta_1^2 - f_2 x_1 \theta_1 + f_3 x_1^2)$$

where f_1, f_2, and f_3 involve only the materials before the first thin chamber. The distribution function for x_2 and θ_2 given that the particle had x_1 and θ_1 and m_{1z} is

$$P(x_2, \theta_2 \mid x_1, \theta_1) = \exp(-g_2) \qquad (2)$$

where

$$g_2 = 4(f_4\, \delta^2 - f_5\, \delta\omega + f_6\, \omega^2)$$

$$\delta = \theta_2 - \theta_1$$

$$\omega = x_2 - x_1 - \theta_1\, (m_{5z} - m_{1z})$$

f_4, f_5, f_6 involve only materials between the first and second chambers. So finally the probability density that the particle followed the dashed path of Figure 18 is

$$P(x_1,\ \theta_1,\ x_2,\ \theta_2) = \exp(-g) \tag{3}$$

where

$$g = g_1 + g_2\,.$$

2) The deviation of a spark from the dashed trajectory is assumed randomly distributed with an r. m. s. width of $\Delta = 1.1$ mm determined by analyzing multiply measured events. The contribution of "spark jitter" is much smaller than this and was neglected. The probability that the sparks were measured at m_j assuming the particle followed the dashed trajectory is

$$P(m_j | x_1,\ \theta_1,\ x_2,\ \theta_2) = \exp(-g_m) \tag{4}$$

where

$$g_m = \frac{1}{2\Delta^2} \sum_{j=1}^{n_1} [m_{jx} - (x + \theta_1 \delta_j)]^2 + \sum_{j=5}^{4+n_2} [m_{jx} - \theta_2 \delta_j)]^2$$

$$\delta_j = \begin{cases} m_{jz} - m_{1z} & \text{for the first chamber} \\ m_{jz} - m_{5z} & \text{for the second chamber .} \end{cases}$$

In deriving g_m, it was assumed that the multiple scattering inside the chambers themselves was small enough so that the track within a chamber was a straight line, i. e., deviations of the sparks from a line in a chamber is only due to measuring error. This is substantiated by the fact that the multiple scattering in a thin plate chamber is more than an order of magnitude smaller than the error Δ. The material in the first chamber was, however, included in determining the f_4, f_5, and f_6 described above.

3) The final desired probability for the $x - z$ plane projection of the sparks is given by an integration over x_1, θ_1, x_2, and θ_2.

$$P(m_{jx}) = \iiiint P(x_1, \theta_{.}, x_2, \theta_2) P(m_{jx} | x_1, \theta_1, x_2, \theta_2) dx, d\theta, dx_2 d\theta_2 = \exp(-g)$$

where

$$g = S_x^2 - J_{2x}^2/\lambda_1 - Fx^2/\lambda_4 - Gx^2/\lambda_7 - Lx^2/\lambda_{10}$$

$$S_x^2 = 4\sigma \sum_{\text{all sparks}} |m_{jx}|^2$$

$$\lambda_1 = f_4 \sigma \sum_{j=5}^{4+n_2} \delta_j^2$$

$$\lambda_4 = 4(F_6 + \sigma n_2) - \lambda_1 R_1^2$$

$$R_1 = (f_5 - D_2)/\lambda_1$$

$$D_2 = 2\sigma \sum_{j=5}^{4+n_2} \delta_j$$

$$\lambda_7 = 4(\sigma n_1 + f_3 + f_6) - f_5^2/\lambda_1 - \lambda_4 R_4^2$$

$$R_4 = (R_1 f_5 - 4f_6)_{\lambda_4}$$

$$\lambda_{10} = 4\left[(f_1 + f_4 - f_5 \Delta z^2 + \sigma \sum_{j=1}^{n_1} \delta_j^2)\right] - R_2^2/\lambda_1 - R_5^2/\lambda_4 - \lambda_7 R_6^2$$

$$R_5 = 2f_5 - 4f_6 \Delta z - R_1 R_2$$

$$R_6 = \frac{1}{\lambda_7} [2(D_1 - f_2 - f_5 + 2f_6\Delta z) + f_5R_2/\lambda_1 - R_4R_5]$$

$$\Delta z = m_{5z} - m_{1z}$$

$$\sigma = \frac{1}{8\Delta^2}$$

$$\hat{L} = (R_5/\lambda_4)\, \hat{F} - 2\hat{J}_1 - (R_2/\lambda_1)\, \hat{J}_2 - R_6\hat{G}$$

$$\hat{G} = R_4\hat{F} - 2\hat{E}_1 + (f_5/\lambda_1)\, \hat{J}_2$$

$$\hat{F} = 2\hat{E}_2 + R_1\hat{J}_2$$

$$\hat{J}_2 = 2\sigma \sum_{j=5}^{4+n_2} \delta_j\hat{m}_j$$

$$\hat{J}_1 = 2\sigma \sum_{j=1}^{n_1} \delta_j\hat{m}_j$$

$$\hat{E}_2 = 2\sigma \sum_{j=5}^{4+n_2} \hat{m}_j$$

$$\hat{E}_1 = 2\sigma \sum_{j=1}^{n_1} \hat{m}_j \ .$$

The J_{2x}, F_x, G_x, and L_x used in the formula for g above are the x components of the vectors defined above.

The probability for a similar set of sparks projected onto the y - z plane is given simply by changing all the subscripts on the vectors from x to y. So finally we have

$$P(\hat{m}_j) = P(m_{jx})\, P(m_{jy}) \ .$$

The generalization of this result for a particle produced from an arbitrary origin $\hat{x}_o$ and with an arbitrary unit momentum vector u is as follows: $P(m_j)$ contains the various vectors only in the combinations $V_x^2 + V_y^2$. But noting that

$$V_x^2 + V_y^2 = |\hat{e}_z \times \hat{V}|^2$$

and that the only thing special about e_z is that it is the initial unit momentum vector, the generalization to arbitrary particle direction is

$$P(\hat{m}_j) = \exp(-\Phi)$$

where

$$\Phi = 4\sigma \sum_{\text{all sparks}} |\hat{u}x\hat{m}_j|^2 - \frac{1}{\lambda}|\hat{u}x\hat{j}_2|^2 - \frac{1}{\lambda_4}|\hat{u}x\hat{F}|^2$$

$$- \frac{1}{\lambda_7}|\hat{u}x\hat{G}|^2 - \frac{1}{\lambda_{10}}|\hat{u}x\hat{L}|^2 .$$

J_2, F, G, L have been defined previously. The generalization to arbitrary x_o simply involves the substitutions

$$\hat{m}_j \rightarrow \hat{m}_j - \hat{x}_o$$

$$\delta_k = \begin{cases} \hat{u} \cdot (\hat{m}_j - \hat{m}_1) & \text{for the first chamber} \\ \hat{u} \cdot (\hat{m}_j - \hat{m}_5) & \text{for the second chamber} \end{cases} .$$

The form of the probability before integration is that of a χ^2 function of $2(n_1 + n_2 + 4)$ degrees of freedom. After integration over the x_1, θ_1, x_2, and θ_2 for each projection of the sparks, Φ should be distributed like a χ^2 function of $2(n_1 + n_2)$ degrees in a Monte Carlo fashion and calculating Φ in each case, and to well within the statistical errors, the distribution of Φ behaved like a χ^2 function of $2(n_1 + n_2)$ degrees of freedom.

B. Derivation of the Multiple Scattering Coefficients

The coefficients f_1, f_2, f_3, f_4, f_5, and f_6 used in determining Φ will be derived.

A collimated beam of particles penetrating a distance z in a homogeneous medium with radiation length L_o, has a distribution function $P(x, \theta)$ given by formula (1) of the previous section. Assume for the moment that after going through n different of materials, the distribution function can be written

$$P_n(x, \theta) = \exp(-4g) \tag{5}$$

where

$$g_n(x, \theta) = f_1^n \theta^2 - 3f_2^n \theta x + 3f_3^n x^2 .$$

Then after going a distance z_{n+1} through a material with radiation length L_{n+1} we have

$$P_{n+1}(x, \theta) = \iint \exp[-4g(x_o, \theta_o)] \exp[-4h(x, \theta, x_o, \theta_o)]dx_o d\theta_o$$

where

$$h(x, \theta, x_o, \theta_o) = \frac{1}{m_{n+1} z_{n+1}} [(\theta - \theta_o)^z - 3(\theta - \theta_o)\eta + 3\eta^2]$$

$$m_{n+1} = (\frac{20 \text{ MeV}}{p\beta})^2 \frac{1}{L_{n+1}}$$

$$\eta = (x - x_o - \theta_o z_{n+1})/z_{n+1} .$$

Performing the integration and casting the result into the form of equation (5) we have

$$g_{n+1}(x, \theta) = f_1^{n+1}\,\theta^2 - 3f_2^{n+1}\,x\theta + 3f_3^{n+1}\,x^2$$

$$f_1^{n+1} = \frac{1}{\alpha}\,[f_1^n + 3f_2^n\,z_{n+1} + (3f_3^n + t^n)z_{n+1}^2]$$

$$f_2^{n+1} = \frac{1}{\alpha}\,[f_2^n + (2f_3^n + t^n)z_{n+1}]$$

$$f_3^{n+1} = \frac{1}{\alpha}\,(f_3^n + t^n)$$

$$t^n = (4f_3^n f_1^n - 3{f^n}^2)m_{n+1}z_{n+1}$$

$$\alpha = 1+4f_1^n\,m_{n+1}z_{n+1}+6f_2^n\,m_{n+1}z_{n+1}^2+(4f_3^n+t^n)m_{n+1}z_{n+1}^3.$$

By induction, the form assumed in equation (5) is justified.

The f_1, f_2, and f_3 are found by using the recursive relations above for all the materials between the origin x_o and the first chamber, and f_4, f_5, f_6 are found similarly by using all the materials between the first and second chambers. Finally, note that the f_2, f_3, f_5, and f_6 used in calculating Φ are three times the respective f's defined above.

C. Determining the Proton Energy

1. Events with a valid range track

The range of the proton in the heavy chambers served only to determine the proton energy when it left the target wall (E_T). A table of E_T vs. the last gap of the proton range was generated by fitting the range-energy curves of the various materials traversed with the formula

$$R(E_T) = g\,E_T^a + c_1 + c_2\,E_T + c_3\,E_T^2 .$$

The parameters g, a, c_1, c_2, and c_3 were separately determined in the three energy intervals [0, 35 MeV], [35, 90 MeV], [90 MeV, 280 MeV]. The first term gives a reasonably good fit (3% off at worst), but this error would be comparable to other sources such as range straggling and the effect of finite plate thickness, so the quadratic was added which reduces the error between the tabulated(46) and calculated ranges to less than 1/4%, which is much smaller than any of the other errors involved.

With this R(E) formula for each material and energy interval, an E_T was calculated for each gap of the proton range telescope and also for events stopping in counters P3, P4, and P6. The results were later compared to a similar table generated by using a program written by Donald Groom(47) and an interpolation routine for intermediate points.(48) The table agreed to within 1/2% which is less than the advertised accuracy of the range tables themselves.

2. Events with no range track

This category includes both events with no measured proton range track, and events which had a measured range track which did not line up with the thin chamber proton track or which did not agree with the measured logic lights. The hypothesis that the proton stopped in counter P2 is always tried before rejecting the event. In this case we required certain minimum pulses in P1 and P2 (see Figure 14). These limits were very liberal, so even events with a range of several gaps in the first heavy chamber could have satisfied the requirements. But the PULCHI requirement after the analysis provided much more stringent requirements on the agreement between the pulses and assumed range, so we were willing to have certain unwanted events go through the analysis to be rejected by the PULCHI criterion later (see Section IV of the main text).

Knowing the calibration of the electronics, the calibration of the phototubes, and the saturation of the scintillator for large energy losses, one can draw an expected curve of the pulse heights P1 vs. P2 for events stopping in P2 (see Figure 14). Also each point on this curve has associated with it a certain energy of the proton as it left the target wall (E_T). Since there are measuring errors, Landau fluctuations in ionization loss, and gain variations in the phototubes which spread the distribution of events from the expected curve, the P1-P2 plane was divided into sections as shown in Figure 14, and a certain E_T was associated with each section. The PULCHI criterion (see Section IV of the main text) eliminated those events which were too far from the expected curve. The data averaged about the expected curve to within 4% (which is the limit of confidence in our overall calibration), so a new "expected curve" was generated by drawing a smooth curve through P1 vs. E_T and P2 vs. E_T for events with a range in the heavy chambers, and extending these curves to the lower energies associated with events having no range track.

3. Energy drop in the target hydrogen

Knowing the energy (E_T) of the proton on leaving the target, and given an assumed origin ($\hat{x}_0$) of the event and an assumed proton angle, one then knows the amount of hydrogen traversed and hence the original energy. The range-energy relation for hydrogen used was

$$R(E) = .000856\, E^{1.812}$$

which fits very well over the interval [0, 150 MeV].

D. Artificial Generation of Events

Before one can determine which of the events that went through the analysis are to be accepted, one must know what to expect from good events whose tracks are subject to the normal multiple scattering, and whose proton range and scope pulses undergo the usual fluctuations. For this purpose a program was written which took a "pure event", i.e., a self-consistent set of particles, angles and energies, and constructed sparks in the thin and heavy plate chambers and the associated scope pulses. All known effects such as multiple scattering, measuring errors, proton range straggling, the finite plate thicknesses in the heavy chambers, and fluctuations in pulse heights were simulated. Also, pion decay was simulated, allowing the decay muon to generate subsequent sparks in that telescope. The "pure" events used as a basis for generating these artificial events were selected from the Monte Carlo events which were generated to determine detection efficiencies (see Section V or Appendix V). This selection was done in such a way that the distribution of selected events in the variables k and $m_{\pi\pi}$ was identical to the distribution of the data in these variables. Finally, the artificial events generated in this way were put through the complete analysis program, and some of the results are described below.

1. Distribution of F (the minimized χ^2)

The distribution of F from fake events in which neither pion decayed is shown in Figure 19. This should be compared with the distribution of F given by the data and one can see that they agree fairly well although not precisely. To explain this difference, artificial events were analyzed in which the measuring error used in generating the events differs from the measuring error assumed in the analysis. Since the statistical uncertainty in the measuring error is about 10%, the test case

$$\sigma_{\text{generate event}} = .9\,\sigma_{\text{analyze}}$$

was tried and produced the distribution shown in Figure 19. Comparing these distributions, we conclude that the differences can be easily explained by the expected uncertainty in the measuring error. Also, the measuring error varied as much as 25% from scanner to scanner, which caused the F distribution of experimental events to be broader than that of fake events.

2. The distributions of B and PULCHI (see Section IV) for nondecaying events are shown in Figures 20 and 21 respectively.

3. Analysis of Decaying Events

The events used as a basis for investigating the effect of pion decay are the selected Monte Carlo events

Figure 19

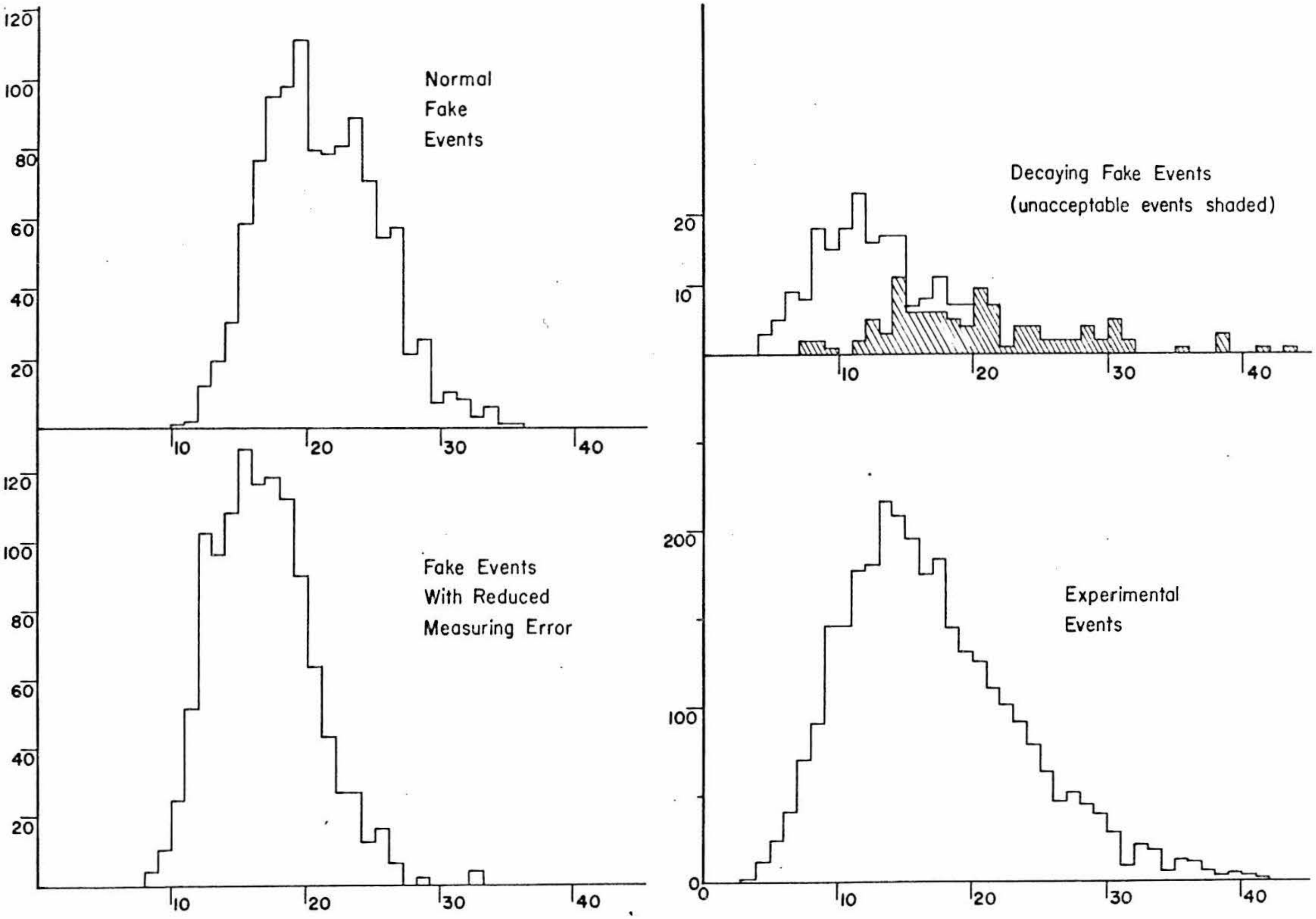

F DISTRIBUTIONS

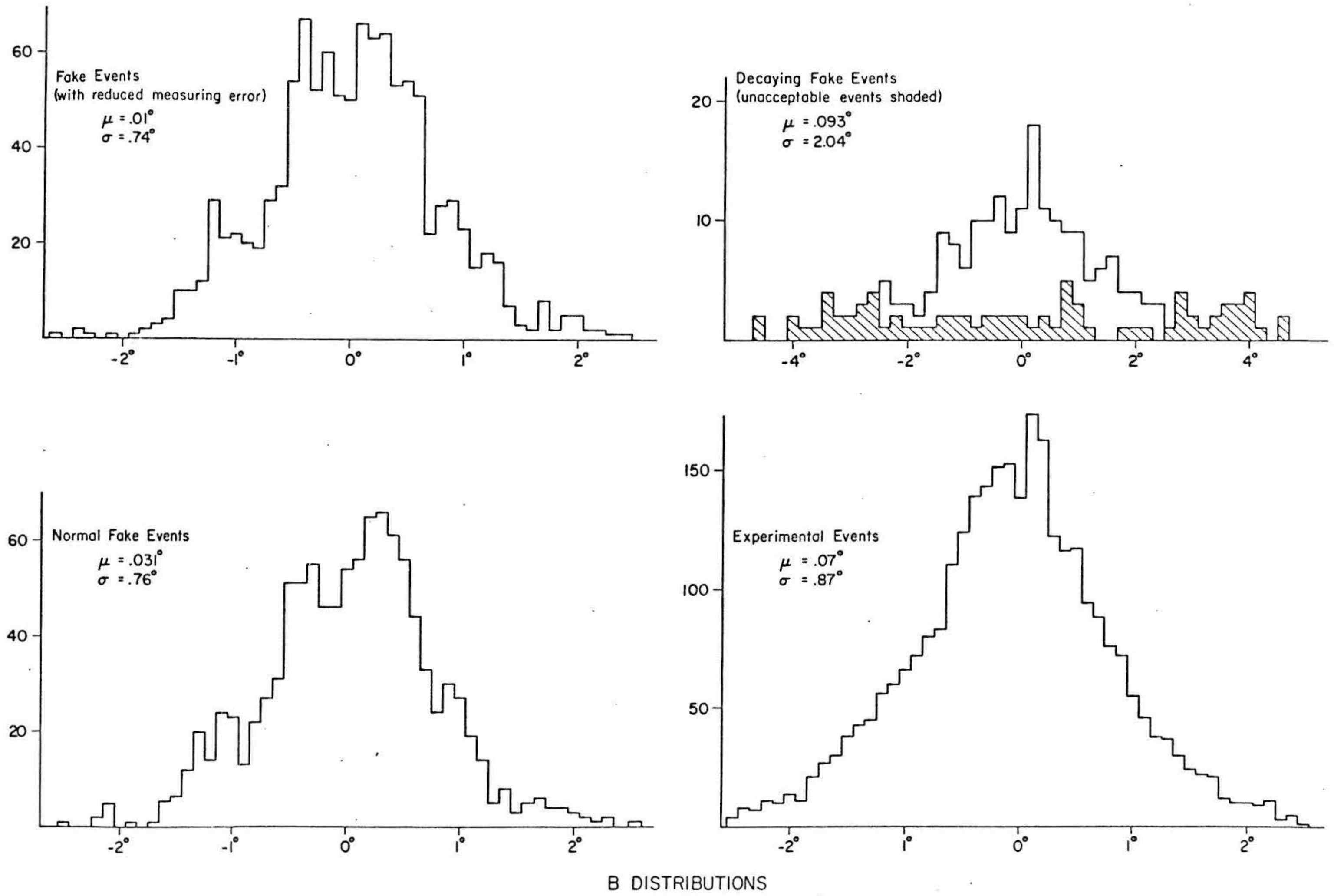
Fake Events
(with reduced measuring error)
μ = .01°
σ = .74°
60
40
20
-2°
-1°
0°
1°
2°
Decaying Fake Events
(unacceptable events shaded)
μ = .093°
σ = 2.04°
20
10
-4°
-2°
0°
2°
4°
Normal Fake Events
μ = .031°
σ = .76°
60
40
20
-2°
-1°
0°
1°
2°
Experimental Events
μ = .07°
σ = .87°
150
100
50
-2°
1°
0°
1°
2°
B DISTRIBUTIONS

Figure 20

Figure 21

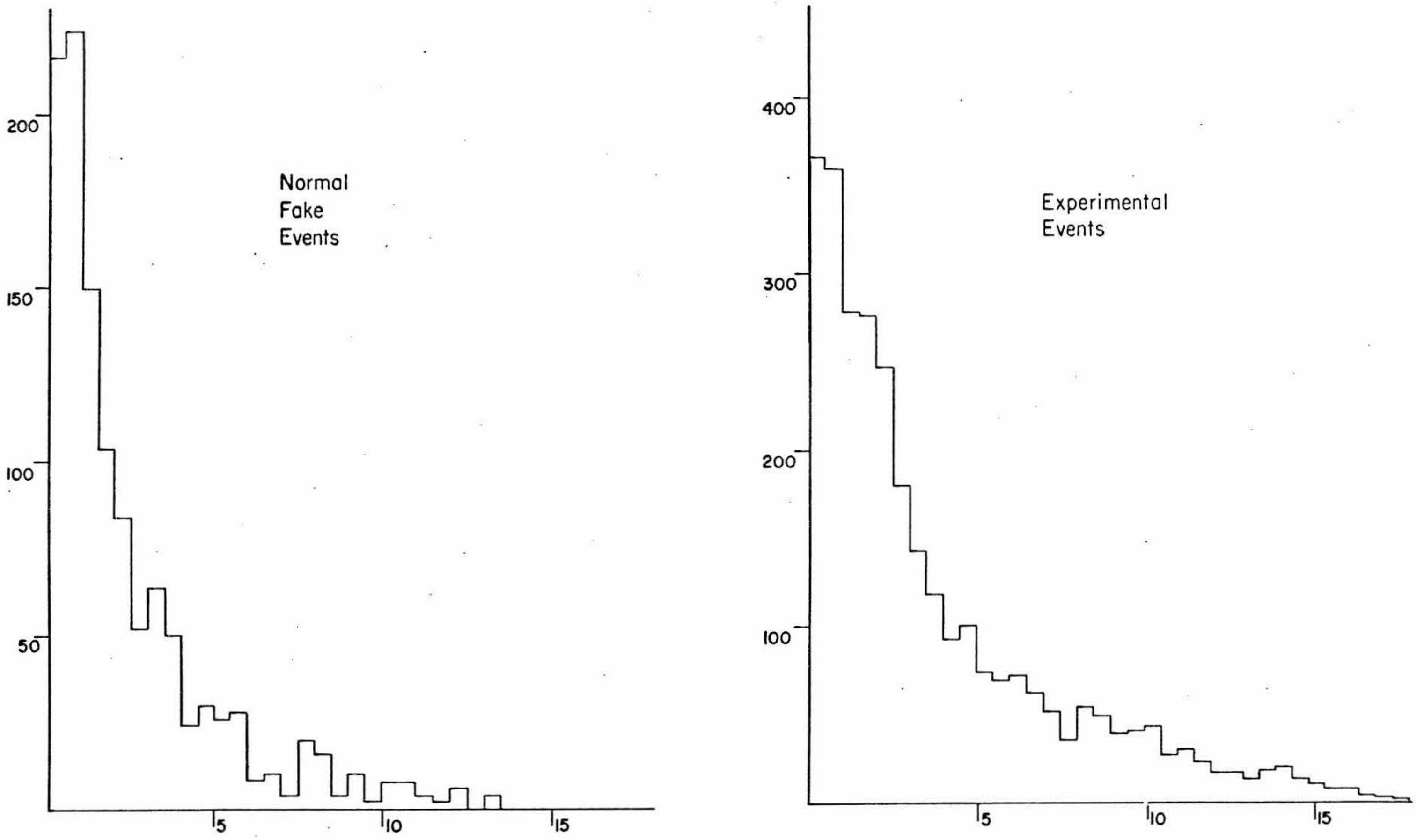

PULCHI DISTRIBUTIONS

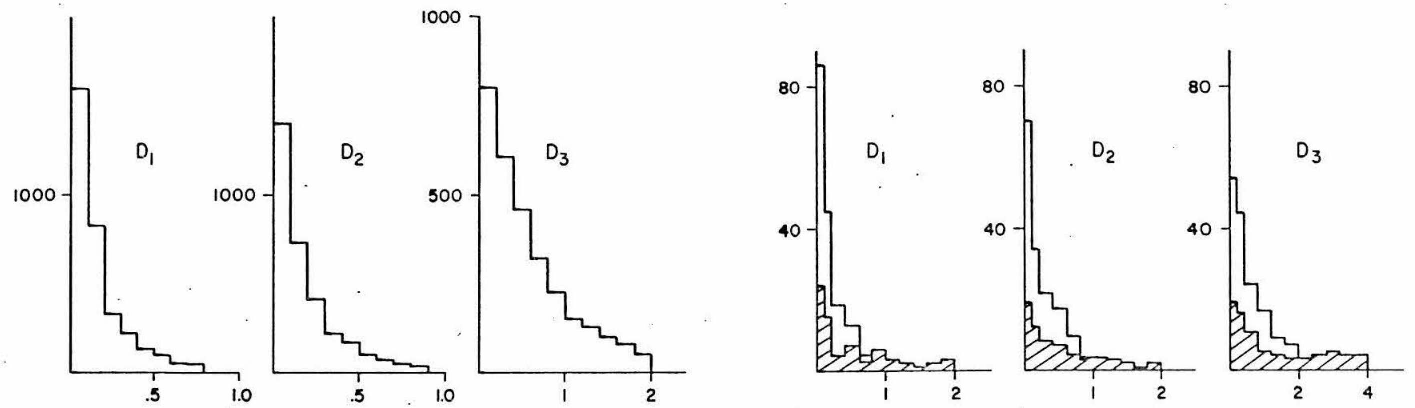

Experimental Events

Decaying Fake Events (shaded portion rejected)

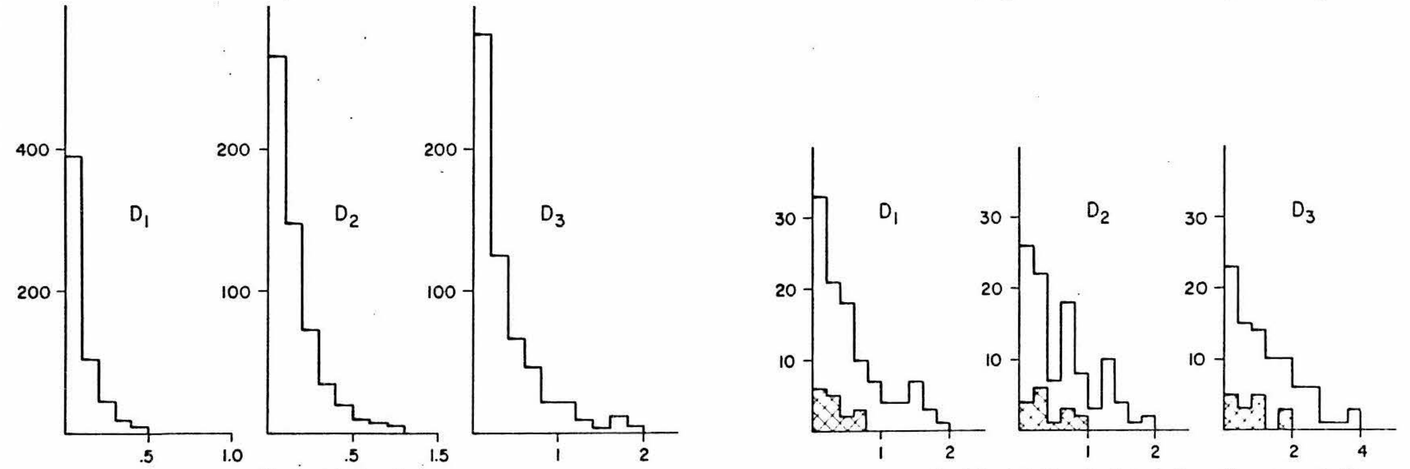

Normal Fake Events

Accidental Events (shaded portion accepted)

DISTRIBUTIONS OF D_K

Figure 22

described above. Knowing the energy of each pion, the decay point was selected from an exponential distribution and the direction of the decay muon was selected from a distribution isotropic in the pion center-of-mass frame. Artificial events were generated as before, except that if a pion decayed before the second spark chamber, the subsequent sparks were altered by the appropriate rotation. It was found that the probability for at least one pion decaying varied from 8% at $m_{\pi\pi} = 530$ to 15% at $m_{\pi\pi} = 900$. However, since a decaying event had only a 22% probability of being accepted by the analysis, we expect 2.7 ± .3% of the final accepted events to contain a pion decay. The distributions of F, B, and D_k for decaying events are shown in Figures 19, 20, and 22 respectively. The distribution of these quantities is much more spread out for decaying events than for non-decaying events. Finally, it should be noted that the resolutions in k and $m_{\pi\pi}$ are also much broader for decaying events. (See Table V).

4. Origin ($\hat{x}_0$) Distributions

Consider first the origin distribution of the Monte Carlo "hits" (the Monte Carlo events which could have been detected in this experiment: see Appendix V). If the spark chamber acceptance apertures were independent of the origin ($\hat{x}_0$), and if the recoil proton was always produced with enough energy to be detected, then the origin distribution from the Monte Carlo "hits" would be uniform along the beam axis (z) and approximately Gaussian in the vertical (y) and horizontal (x) directions (and centered in the

TABLE V

Resolutions in Various Quantities

	non-decaying events	decaying events	effect of +1/2% change in R(E)	effect of $W_{\pi}2$ up 3 mm
k	24 MeV	92 MeV	+5	+4.4 MeV
$m_{\pi\pi}$	8 MeV	38 MeV	+3	+2.1 MeV
T_p	2 MeV	3 MeV	+.3 -.7 MeV	.3 MeV
x_o	1.7 mm	8.5 mm	--	.1 mm
y_o	1.8 mm	3.9 mm	--	- .9 mm
z_o	2.5 mm	1.43 mm	--	- .7 mm

beam axis). However, since the spark chamber apertures changed with x_o, and since the recoil proton was required to have an energy $T_p > 35$ MeV as it left the target, the origin distribution of Monte Carlo "hits" will be somewhat distorted from that described above.

If dipion production was completely dominated by phase space, then the origin distribution of experimental events would be identical to the origin distribution of the "hits" described above. However, the origin distribution of the selected Monte Carlo events will be further distorted by the production cross section. In particular, if the cross section is large for low proton energy, then the origin distributions would be shifted toward the top and the front of the target. (A low energy proton has a greater probability of leaving the target with $T_p > 35$ MeV if its origin is near the front or the top of the target, i. e., if it must penetrate less hydrogen.)

Figures 23 and 24 show the origin distributions from both the experimental events and the selected Monte Carlo events. In conclusion, it appears that the effects described above are sufficient to explain the experimental origin distribution.

5. Accidental Event Acceptance

Since the particle fluxes during this experiment were quite high, it is possible that despite the various checks a frame may be accepted which contains tracks from separate events in the target. To determine this contamination two things are necessary. The first is to know how often one observes various types of accidental events, and the second is how often an accidental event is accepted into the final data.

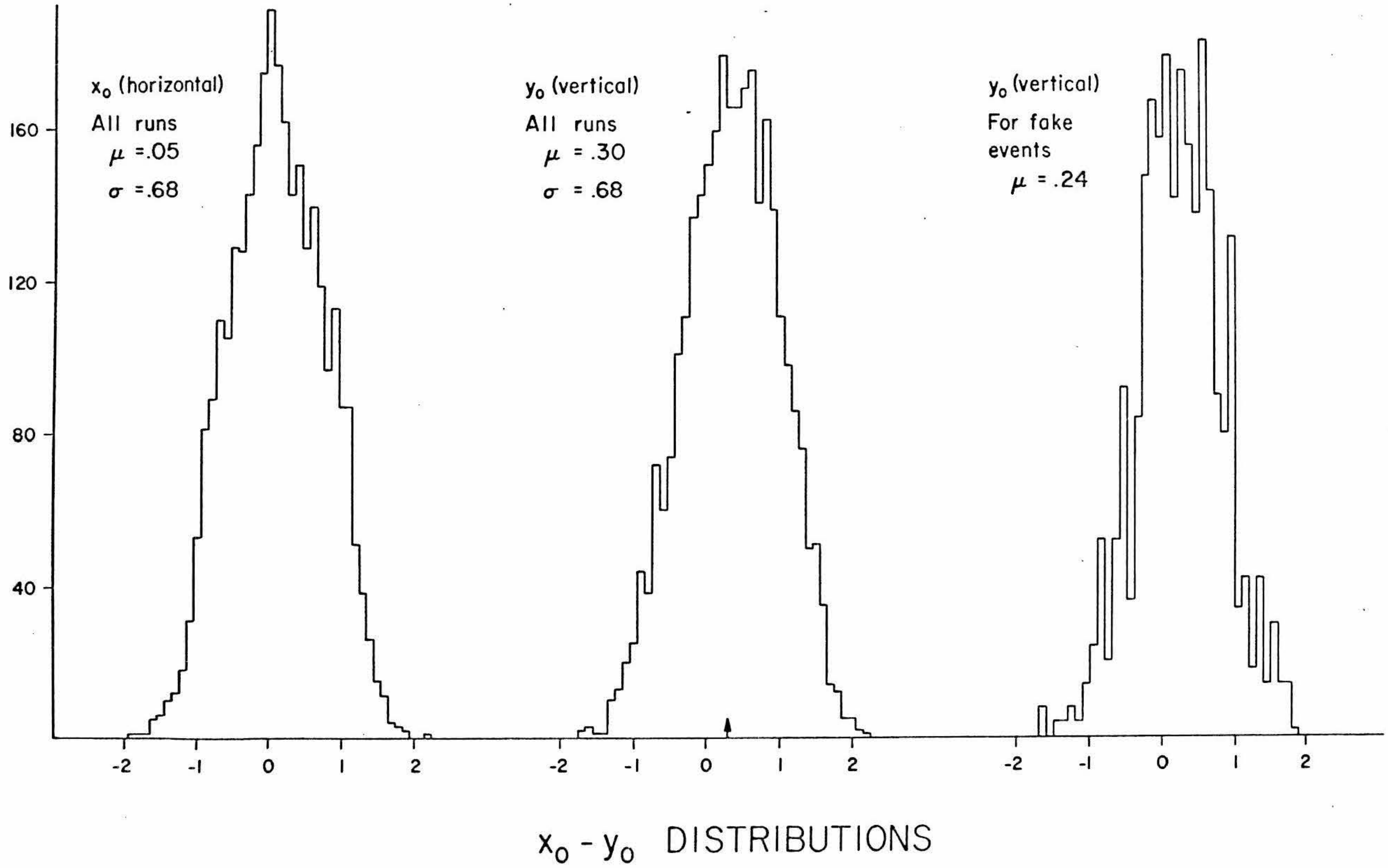
160
120
80
40
x_o (horizontal)
All runs
μ =.05
σ =.68
y_o (vertical)
All runs
μ = .30
σ = .68
y_o (vertical)
For fake events
μ = .24
-2
-1
0
1
2
-2
-1
0
1
2
-2
-1
0
1
2
$x_o - y_o$ DISTRIBUTIONS

Figure 23

Figure 24

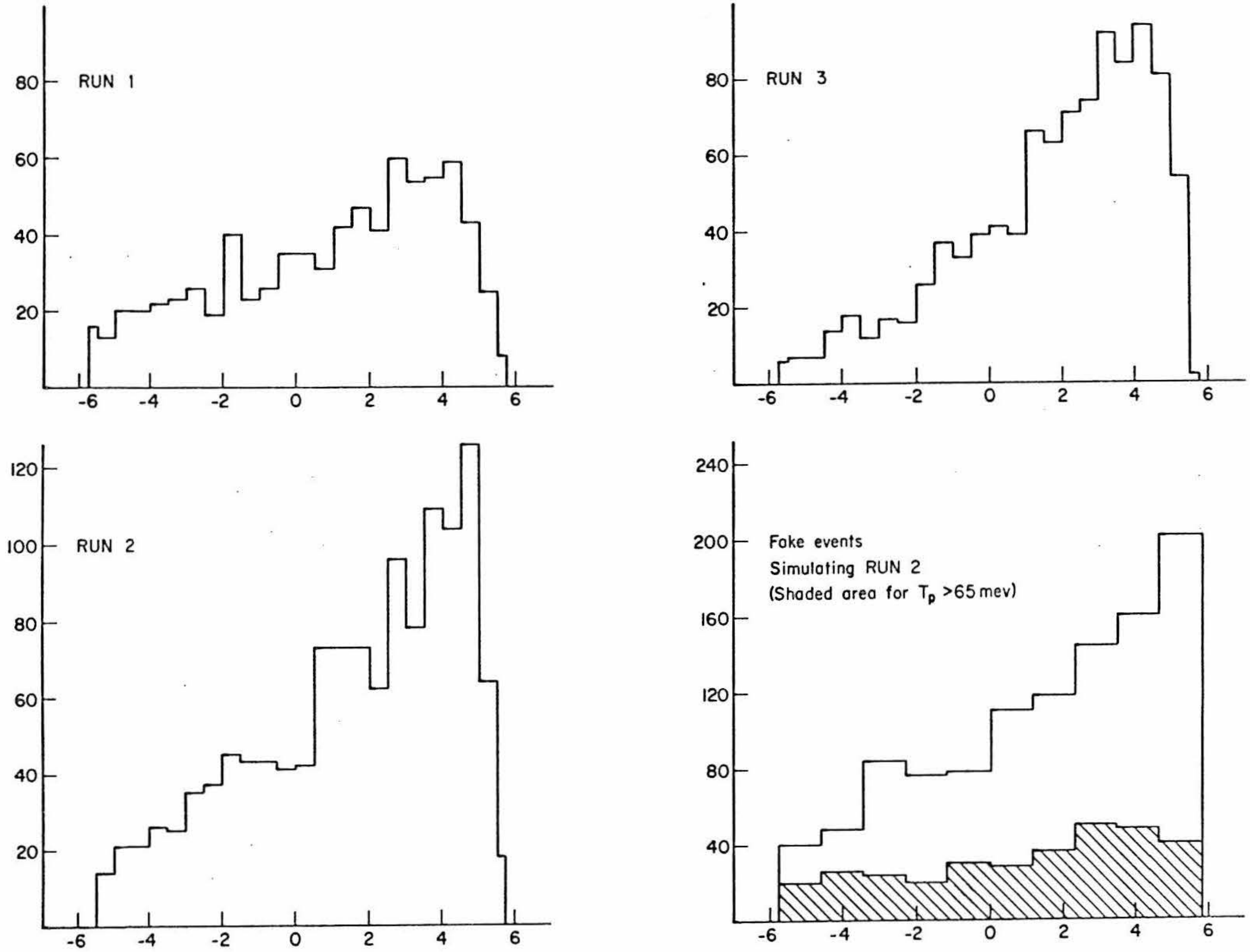

Z_0 DISTRIBUTIONS

To answer the first question, we may look at the "accidental runs" taken during the experiment. In these runs, the output of the pion coincidence circuit C_π (see Figure 3) was delayed 100 ns with respect to the rest of the logic. During these runs, the triggers per BIP were generally 35-40% of the normal trigger rate, which indicates that we expect 35-40% of the frames to be bad from this type of accidental alone. But there are other types of accidentals. For instance, the proton and one pion could be related, with the other pion being an alien intruder. Since the rate of accidentals from the accidental runs agrees roughly with a calculation based on the rates involved and the coincidence resolving time, one may attempt to estimate this latter type of accidental by a calculation. Using a coincidence rate of 150/sec between the proton telescope and one pion telescope, 10^4/sec from a one pion telescope, and an 8 ns resolving time we have 1.2×10^{-2}/sec of these accidentals. But we must multiply this by two because the odd pion track can come from either telescope. This type of accidental may then be 50% of the total trigger rate. Finally, we see that almost all of the spark chamber trigger rate could be explained by accidentals.

In determining the probability for accepting accidental events, two approaches are available. First, when all the accidental runs described in the preceding paragraph are analyzed, they contain only two accepted events. The empty target runs only provide ten accepted events (which is consistent with production from gaseous hydrogen). From this one can say that phenomenologically we expect 2 ± 1% of the data to be accidentals or events produced in the target walls. The second source of information comes from constructing "events" by combining two consecutive measured events. In particular, the proton track and pulses from one event and the pion tracks from the preceding event were combined to form an artificial event which was then analyzed. Of these artificial events, 4% can be accepted, thus, if 70% of the total frames are accidentals, then 2.8% of the total frames would be acceptable accidentals. Since 20% of the total frames were accepted, this would mean that accidentals constitute 12% of accepted events. But this is a biased indication of the accidental contamination. In forming an artificial event by the method described above, the pion tracks tend to point in certain kinematically preferred directions. The pion tracks from a true accidental, however, would in general be distributed evenly throughout the spark chamber aperture, and thus would have less probability of being compatible with an arbitrary proton track.

The contamination from the accidentals described above (the two "pions" coming from one event and the proton from another) was taken to be 5 ± 3%, and if the rest of the unacceptable frames are accidentals, then the total accidental contamination should be 9 ± 4%.

6. Resolutions

The quantities whose resolutions are considered here are the photon energy k, the dipion mass $m_{\pi\pi}$, the initial proton energy T_p, and the origin vector $\hat{x}_o$. The artificial events described in Section 5 of this appendix were used to give information about the various resolutions, and the results are shown in Table V. These artificial events, however, give no information about systematic errors. There are several sources of systematic errors described below.

First, the proton range curves used to determine the proton energy are advertized as accurate to 1% in range (or 1/2% in energy). Table V indicates the influence of this error on certain variables. Second, errors in the fiducials and virtual cameras used in reconstructing spark positions contribute significantly. In particular, the $W\pi 2$ chamber gave some difficulty (see Appendix IV) and could produce a 3 mm systematic error in the sparks in that chamber, so an analysis was done in which the $W\pi 2$ sparks were shifted up 3 mm and the results are shown in Table V.

From these investigations, it is estimated that the data contain a systematic error which is much smaller than the resolution expected from non-decaying events.

7. Final Selection of Acceptable Events

Various quantities calculated during the analysis were used to determine whether or not an event was finally accepted (see Section IV for detailed description of these quantities). The following table shows the limits on certain quantities, and the fraction of good events expected to be rejected by that criterion.

TABLE VI

There is some correlation between events rejected by the various criteria. Using the artificial events as an indication of this correlation, the final probability for rejecting a good event is 5 ± 2%.

	upper limit	% rejection
F	40	2 ± 1%
B	2.5°	3/4 ± 1/4
D_1	$.8\ \text{cm}^2$	
D_2	$.9\ \text{cm}^2$	4 ± 2%
D_3	$1.9\ \text{cm}^2$	
PULCHI	16	1/2%

APPENDIX IV

Reconstruction of Sparks

The method used to obtain the space position of a spark knowing its film coordinates in the standard coordinate system was as follows. Given the film coordinates of a view of the spark and the space and film coordinates of nearby fiducials, one can determine the position of the intersection onto the fiducial plane of the line from the spark to the virtual camera for that view i. e., either point F_T or F_S of Figure 25A. The closest approach of the two vectors $\overline{C_T F_T}$ and $\overline{C_S F_S}$ defines the spark position.

A. Fiducial Positions

Before and after each experimental setup, the positions of certain fiducials were surveyed. Since the top and side fiducials of a telescope are integral parts of the same structure, the positions of fiducials in the top views were surveyed by marking their projection onto the floor and their heights with respect to fiducials attached to cement shielding blocks. When the apparatus was finally dismantled, each fiducial structure was mounted on a planar and the relative positions of all fiducials in both views were measured very accurately. Using this information, the space positions of all fiducials were determined. Since some fiducials were very difficult to survey, the measuring accuracy is not what it could have been under more comfortable circumstances, but it should be noted that the multiple scattering of sparks is many times the possible error in fiducial

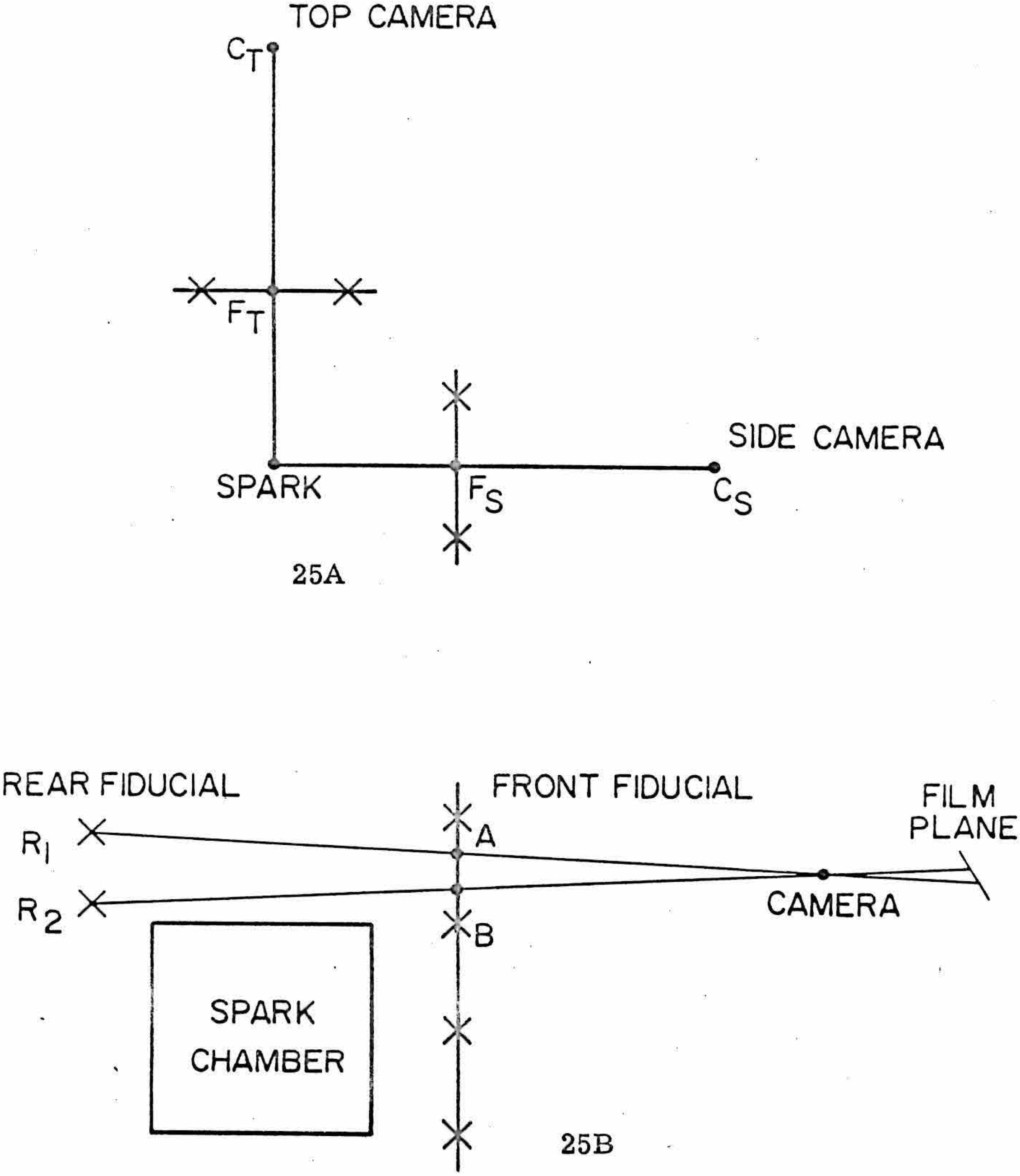
TOP CAMERA
C_T
F_T
SIDE CAMERA
SPARK
F_S
C_S
25A
REAR FIDUCIAL
FRONT FIDUCIAL
FILM PLANE
R_1
A
R_2
CAMERA
B
SPARK CHAMBER
25B

Figure 25

positions. So this effect contributes a systematic error which is negligible compared to the resolutions.

B. Camera Positions

We will start by discussing the top view of the proton telescope because it does not offer problems encountered in other views and telescopes. For each view of each telescope, there were what are called front and rear fiducials. The front fiducials were crosses scribed on a lucite plate through which one observed the spark chambers. The rear fiducials were crosses further from the camera than the front fiducials and in general further from the camera than the spark chamber (see Figure 25B). Knowing the space and film positions of all fiducials, one can determine the space positions of the projections of the rear fiducials onto the front fiducial plane, i. e., points A, B, C, etc. (there were ten rear fiducials for the proton top view). Then using the vectors $\overline{R_1A}$, $\overline{R_2B}$, $\overline{R_3C}$, etc. one can determine the camera position by a least squares fit to these directions.

Using this method to determine the pion top view cameras has additional difficulties. Because the fiducial plane and the film plane were not parallel as in the proton top view, and because the rear fiducials were in a single row (the proton rear fiducials were in two parallel rows fairly well separated) the method described in the preceding paragraph became much more difficult and inaccurate. Instead, the direction of the camera was determined by the projection of the rear fiducials onto the front fiducial plane, and the distance of the camera from the front fiducial plane was determined by the closest approach of this direction to the proton top camera.

The side views presented another problem in that the side camera for each chamber was independent. Here one uses the fact that the side mirrors of a chamber were adjusted such that the side camera was along a line from the center of the side fiducial plane and normal to that plane. The distance of the camera along that line was determined as follows. Knowing the separation of fiducials on the film, the focal length of the camera lens, and the separation of these fiducials in space, one could determine the distance. Also knowing the projection of the two rear fiducials onto the front fiducial plane the distance can be determined. Both of these facts were used, and a least squares fit to the camera distance was made knowing all the errors involved.

C. Checks on the Reconstruction

After the data collecting for the experiment was finished, the thin foil chambers were removed from their supports while leaving the whole fiducial system unchanged. Then five "beams" were constructed which held an array of scribed crosses at each end and in such a way that each array of crosses was in a place formerly occupied by a spark chamber. The pairs of "chambers" connected by the five beams were a) front east pion ($E\pi 1$) to rear east pion ($E\pi 2$), b) front west pion ($W\pi 1$) to rear west pion ($W\pi 2$), c) front proton (PTF1) to rear proton (PTF2), d) $E\pi 1$ to $W\pi 1$, and e) PTF1 to $E\pi 1$. With a certain beam in position between two "chambers", photographs were taken of these crosses. The space position of each cross was determined by exactly the same measurement and reconstruction process used for regular sparks.

Finally, the distances between the reconstructed position of any two crosses was compared with a direct measurement made on the beam. All the reconstructed distances were correct to within 1 mm except the $W\pi 1$ to $W\pi 2$ distances. As an additional indicator, the closest approach distance (KAP) between the top and side view lines used to reconstruct a cross was checked, and again all crosses except those on $W\pi 2$ had a small KAP. The fault appears to be in $W\pi 2$ only, because the crosses in $W\pi 1$ have small KAP and $W\pi 1$ to $E\pi 1$ distances are correct. Investigations of the source of this difficulty show that if one adjusts the camera positions to correct the $W\pi 1$ - $W\pi 2$ distances, then KAP becomes worse for $W\pi 2$. Also various fiducial distances were rechecked and found to be correct, so the situation is that $W\pi 1$ - $W\pi 2$ distances are off by 4 mm and KAP is 3 mm for the $W\pi 2$ crosses.

If there is a systematic shift in the spark positions in $W\pi 2$, this should be observable in the D_k distributions of Figure 22. A test performed by shifting the $W\pi 2$ sparks up 3 mm and/or west 3 mm indicated that there should be a discernable flatness of the distributions near $D_k = 0$. Since the data show no such appreciable flatness, we conclude that the systematic error in $W\pi 2$ spark positions is within 3 mm and this is included as part of the systematic errors in Table III.

APPENDIX V

Detection Efficiencies

A. Particle Acceptance Apertures

First the four corners of each thin foil chamber were determined. From these, a set of apertures was generated defined by the intersection of the two chamber apertures of a telescope as viewed from a given origin $\hat{x}_0$. Thus each particle telescope had a set of ten apertures corresponding to the ten uniformly spaced origin positions used in generating events (see below). In a few cases, an aperture formed a pentagon, in which case the corner with the largest internal angle was eliminated.

To determine the acceptance limits of an individual chamber, two methods are available. First, the measured positions of the corners of the chambers and counters can be used. The difficulty in this is that the scanners may have tended to miss tracks near the edges of a chamber, so as far as the scanning and measuring is concerned, the effective volume of a chamber may be somewhat smaller than its physical volume. This might lead to the conclusion that the cross section in a certain region was zero when in fact only the scanning detection efficiency was zero. The second method is to use the distribution of sparks from acceptable events to define the chamber edges. The difficulty here is that the kinematics may make acceptable events congregate in certain sections of a chamber. (For instance, the pion tracks obviously tend to lie below the beam line.) This might lead to the conclusion that this experiment can provide no information on the cross section in certain regions, when in fact, since the detection efficiency in that region was really non-zero, we do have such information.

It was finally decided that a scanner could without difficulty see events within 2 mm of any edge of a pion chamber and within .1 mm of any edge of a proton chamber. Then if enough events were found closer to an edge than these limits, the aperture was enlarged to include these events.

B. Generation of Events

To determine the detection efficiency at a given photon energy, k, and dipion mass, $m_{\pi\pi}$, an origin for the event was chosen from a distribution uniform along the beam direction and Gaussian in the vertical direction, to simulate the known incident beam shape. The proton direction was selected from a distribution isotropic in the overall center-of-mass system, and the pion decay direction was selected from a distribution isotropic in the dipion center-of-mass system. The resultant particle directions were then examined to see if they passed through their respective particle apertures. In addition, the proton was required to leave the hydrogen target with at least 35 MeV kinetic energy to represent an event which could be detected by the proton telescope. Each successful event was recorded on magnetic tape for further reference.

C. Efficiency Calculation

At a given k and $m_{\pi\pi}$, the distribution of successful events in t (the invariant momentum transfer) would yield directly the efficiency $E(k, m_{\pi\pi}, t)$. However, the distribution of t for constant k and $m_{\pi\pi}$ was sharply peaked, so the region of non-zero efficiency for each experimental setup was effectively a surface (not a volume) in $k - m_{\pi\pi} - t$ space. Thus, the efficiency was considered a function of only two variables, and the results for $E(k, m_{\pi\pi})$ are shown in Figure 26 for each of the three setups. Table VII shows the efficiencies (multiplied by 10^7) and Table VIII shows the value of $\cos\theta_{cm}$ at which the efficiencies were peaked.

Assumptions about the dipion decay distribution may affect the results quite markedly. In the dipion center-of-mass system, define a polar coordinate system in which the photon direction is $\theta = 0$ and the $\gamma - p$ reaction plane defines $\varphi = 0$. The spark chambers were sensitive only for dipions which decayed with $\theta = 90^o \pm 9^o$ and $\varphi = 90^o \pm 17^o$. Defining $f(\theta, \varphi) \frac{\Delta\Omega}{4\pi}$ as the fraction of decays in which the π^+ decayed into the solid angle element $\Delta\Omega$, then all efficiencies must be divided by $1/2(f(\pi/2, \pi/2) + f(\pi/2, -\pi/2))$ to compensate for anisotropic dipion decay (see Section V). The results from the CEA and DESY collaborations fail to indicate any statistically significant anisotropy, so no correction factor was applied to the efficiencies.

D. Detection of the N*(1238 MeV) Resonance

To determine the influence of N* production in our results, events were generated similar to those described in Section B of this appendix. In this case, however, the production and decay distributions of the N* were provided by previous experiments.(22, 23) The distribution of event origins in the target and the criteria for a successful event were otherwise the same as described in Section B above. These events were then analyzed to provide the distribution of $d^2\sigma(k, m_{\pi\pi}, t)/d\Omega dm_{\pi\pi}$ expected from N** production alone (see Table II).

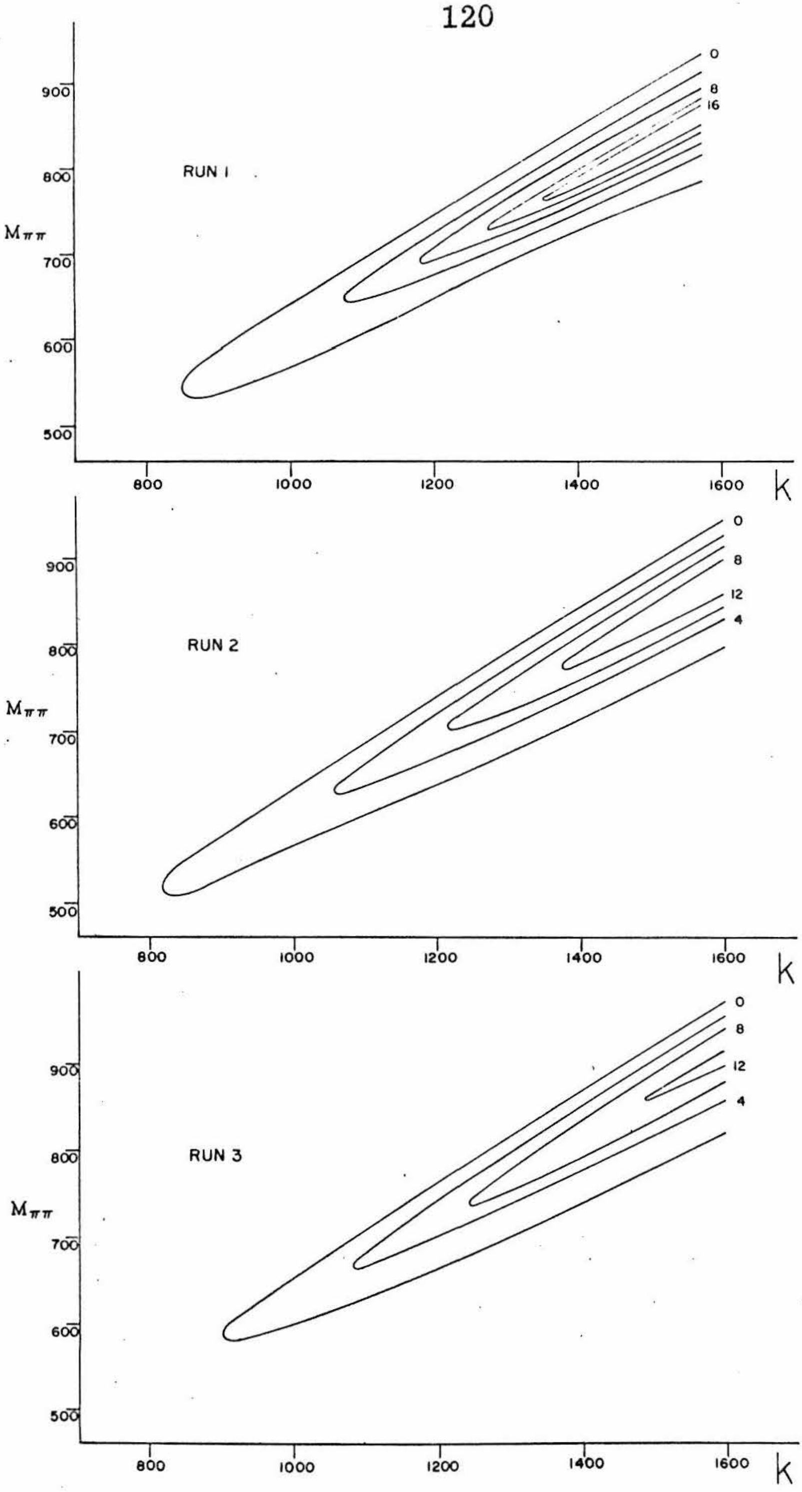

DETECTION EFFICIENCY

Figure 26

$m_{\pi\pi}$ ↓

	0.5	0.	0.	0.	0.	0.	0.	0.	0.	0.	0.	0.	0.	0.	0.	0.	0.
	0.	8.8	0.7	0.	0.	0.	0.	0.	0.	0.	0.	0.	0.	0.	0.	0.	0.
	0.	0.9	7.9	0.9	0.	0.	0.	0.	0.	0.	0.	0.	0.	0.	0.	0.	0.
600 —	0.	0.	4.5	17.6	4.0	0.	0.	0.	0.	0.	0.	0.	0.	0.	0.	0.	0.
	0.	0.	0.	18.3	25.7	4.2	0.	0.	0.	0.	0.	0.	0.	0.	0.	0.	0.
	0.	0.	0.	0.3	31.5	40.2	5.4	0.	0.	0.	0.	0.	0.	0.	0.	0.	0.
	0.	0.	0.	0.	1.9	44.9	57.6	8.9	0.2	0.	0.	0.	0.	0.	0.	0.	0.
	0.	0.	0.	0.	0.	7.6	70.1	62.7	10.2	0.1	0.	0.	0.	0.	0.	0.	0.
700 —	0.	0.	0.	0.	0.	0.	17.2	104.2	73.3	14.7	0.1	0.	0.	0.	0.	0.	0.
	0.	0.	0.	0.	0.	0.	0.	40.5	108.2	68.6	16.0	0.	0.	0.	0.	0.	0.
	0.	0.	0.	0.	0.	0.	0.	1.1	59.1	136.1	58.6	15.0	0.1	0.	0.	0.	0.
	0.	0.	0.	0.	0.	0.	0.	0.	7.5	91.6	139.6	66.1	17.0	0.0	0.	0.	0.
	0.	0.	0.	0.	0.	0.	0.	0.	0.	19.7	101.2	141.9	84.0	23.4	0.3	0.	0.
800 —	0.	0.	0.	0.	0.	0.	0.	0.	0.	0.	34.7	118.7	130.3	83.3	26.6	0.8	0.
	0.	0.	0.	0.	0.	0.	0.	0.	0.	0.	0.4	54.4	141.7	132.1	80.0	28.8	0.
	0.	0.	0.	0.	0.	0.	0.	0.	0.	0.	0.	5.2	61.6	167.4	136.2	80.2	0.
	0.	0.	0.	0.	0.	0.	0.	0.	0.	0.	0.	0.	10.8	81.8	144.3	134.7	0.
	0.	0.	0.	0.	0.	0.	0.	0.	0.	0.	0.	0.	0.	28.1	97.4	157.5	0.
900 —	0.	0.	0.	0.	0.	0.	0.	0.	0.	0.	0.	0.	0.	0.	44.1	141.2	0.
	0.	0.	0.	0.	0.	0.	0.	0.	0.	0.	0.	0.	0.	0.	0.	51.9	0.
	0.	0.	0.	0.	0.	0.	0.	0.	0.	0.	0.	0.	0.	0.	0.	1.7	0.
	0.	0.	0.	0.	0.	0.	0.	0.	0.	0.	0.	0.	0.	0.	0.	0.	0.
	0.	0.	0.	0.	0.	0.	0.	0.	0.	0.	0.	0.	0.	0.	0.	0.	0.
	0.	0.	0.	0.	0.	0.	0.	0.	0.	0.	0.	0.	0.	0.	0.	0.	0.
	0.	0.	0.	0.	0.	0.	0.	0.	0.	0.	0.	0.	0.	0.	0.	0.	0.

RUN 1

$m_{\pi\pi}$ ↓

	2.2	0.	0.	0.	0.	0.	0.	0.	0.	0.	0.	0.	0.	0.	0.	0.	0.
	1.0	6.6	0.	0.	0.	0.	0.	0.	0.	0.	0.	0.	0.	0.	0.	0.	0.
	0.	13.1	4.9	0.	0.	0.	0.	0.	0.	0.	0.	0.	0.	0.	0.	0.	0.
600 —	0.	0.	22.0	13.8	0.	0.	0.	0.	0.	0.	0.	0.	0.	0.	0.	0.	0.
	0.	0.	1.5	60.6	22.9	0.	0.	0.	0.	0.	0.	0.	0.	0.	0.	0.	0.
	0.	0.	0.	12.9	72.9	25.0	0.8	0.	0.	0.	0.	0.	0.	0.	0.	0.	0.
	0.	0.	0.	0.	48.3	92.8	21.3	1.3	0.	0.	0.	0.	0.	0.	0.	0.	0.
	0.	0.	0.	0.	0.	92.1	136.9	39.3	2.5	0.	0.	0.	0.	0.	0.	0.	0.
700 —	0.	0.	0.	0.	0.	5.8	113.2	148.7	37.0	4.8	0.	0.	0.	0.	0.	0.	0.
	0.	0.	0.	0.	0.	0.	18.3	139.1	147.5	48.6	6.0	0.	0.	0.	0.	0.	0.
	0.	0.	0.	0.	0.	0.	0.	43.8	181.4	166.8	41.9	9.1	0.	0.	0.	0.	0.
	0.	0.	0.	0.	0.	0.	0.	0.	92.7	235.8	183.8	71.0	7.8	0.	0.	0.	0.
	0.	0.	0.	0.	0.	0.	0.	0.	6.0	126.6	223.9	164.1	76.2	8.4	0.	0.	0.
800 —	0.	0.	0.	0.	0.	0.	0.	0.	0.	27.3	182.9	266.2	186.7	74.0	13.4	0.	0.
	0.	0.	0.	0.	0.	0.	0.	0.	0.	0.	45.7	196.9	257.7	162.8	68.8	8.4	0.
	0.	0.	0.	0.	0.	0.	0.	0.	0.	0.	0.	83.1	238.5	250.3	148.6	74.4	0.
	0.	0.	0.	0.	0.	0.	0.	0.	0.	0.	0.	6.0	132.7	277.4	260.4	166.4	0.
	0.	0.	0.	0.	0.	0.	0.	0.	0.	0.	0.	0.	33.4	208.2	295.0	236.8	0.
900 —	0.	0.	0.	0.	0.	0.	0.	0.	0.	0.	0.	0.	0.	32.5	243.0	294.4	0.
	0.	0.	0.	0.	0.	0.	0.	0.	0.	0.	0.	0.	0.	0.	80.8	259.1	0.
	0.	0.	0.	0.	0.	0.	0.	0.	0.	0.	0.	0.	0.	0.	1.5	140.8	0.
	0.	0.	0.	0.	0.	0.	0.	0.	0.	0.	0.	0.	0.	0.	0.	21.6	0.
	0.	0.	0.	0.	0.	0.	0.	0.	0.	0.	0.	0.	0.	0.	0.	0.	0.
	0.	0.	0.	0.	0.	0.	0.	0.	0.	0.	0.	0.	0.	0.	0.	0.	0.
	0.	0.	0.	0.	0.	0.	0.	0.	0.	0.	0.	0.	0.	0.	0.	0.	0.

RUN 2

$m_{\pi\pi}$ ↓

	0.	0.	0.	0.	0.	0.	0.	0.	0.	0.	0.	0.	0.	0.	0.	0.	0.
	7.6	0.	0.	0.	0.	0.	0.	0.	0.	0.	0.	0.	0.	0.	0.	0.	0.
	0.	25.3	0.	0.	0.	0.	0.	0.	0.	0.	0.	0.	0.	0.	0.	0.	0.
600 —	0.	0.	27.4	0.5	0.	0.	0.	0.	0.	0.	0.	0.	0.	0.	0.	0.	0.
	0.	0.	3.8	34.0	4.2	0.	0.	0.	0.	0.	0.	0.	0.	0.	0.	0.	0.
	0.	0.	0.	30.1	55.8	6.1	0.	0.	0.	0.	0.	0.	0.	0.	0.	0.	0.
	0.	0.	0.	0.	47.2	62.7	7.5	0.	0.	0.	0.	0.	0.	0.	0.	0.	0.
	0.	0.	0.	0.	0.5	76.1	68.7	14.3	0.	0.	0.	0.	0.	0.	0.	0.	0.
700 —	0.	0.	0.	0.	0.	14.4	110.9	74.0	14.7	0.2	0.	0.	0.	0.	0.	0.	0.
	0.	0.	0.	0.	0.	0.	49.3	120.2	73.2	19.7	1.5	0.	0.	0.	0.	0.	0.
	0.	0.	0.	0.	0.	0.	0.	85.7	165.1	89.1	16.8	2.0	0.	0.	0.	0.	0.
	0.	0.	0.	0.	0.	0.	0.	2.8	105.2	183.9	90.2	26.3	1.8	0.	0.	0.	0.
	0.	0.	0.	0.	0.	0.	0.	0.	22.6	151.1	181.3	92.7	24.2	1.9	0.	0.	0.
800 —	0.	0.	0.	0.	0.	0.	0.	0.	0.	42.9	161.1	212.8	90.7	23.1	2.0	0.	0.
	0.	0.	0.	0.	0.	0.	0.	0.	0.	0.	85.1	174.8	207.3	93.2	29.8	2.3	0.
	0.	0.	0.	0.	0.	0.	0.	0.	0.	0.	5.3	121.4	206.4	173.4	106.6	30.7	0.
	0.	0.	0.	0.	0.	0.	0.	0.	0.	0.	0.	33.8	144.2	229.9	179.3	97.1	0.
	0.	0.	0.	0.	0.	0.	0.	0.	0.	0.	0.	0.	48.7	193.4	224.0	187.2	0.
900 —	0.	0.	0.	0.	0.	0.	0.	0.	0.	0.	0.	0.	0.	111.4	212.9	252.3	0.
	0.	0.	0.	0.	0.	0.	0.	0.	0.	0.	0.	0.	0.	11.3	153.7	233.7	0.
	0.	0.	0.	0.	0.	0.	0.	0.	0.	0.	0.	0.	0.	0.	35.4	172.3	0.
	0.	0.	0.	0.	0.	0.	0.	0.	0.	0.	0.	0.	0.	0.	0.	60.1	0.
	0.	0.	0.	0.	0.	0.	0.	0.	0.	0.	0.	0.	0.	0.	0.	0.	0.
	0.	0.	0.	0.	0.	0.	0.	0.	0.	0.	0.	0.	0.	0.	0.	0.	0.
	0.	0.	0.	0.	0.	0.	0.	0.	0.	0.	0.	0.	0.	0.	0.	0.	0.

1.0 1.2 1.4 k(BeV)

RUN 3

ρ^0 Detection Efficiency (x 10^7)

TABLE VII

	0.905	0.	0.	0.	0.	0.	0.	0.	0.	0.	0.	0.	0.	0.	0.	0.	0.
	0.	0.919	0.920	0.	0.	0.	0.	0.	0.	0.	0.	0.	0.	0.	0.	0.	0.
	0.	0.888	0.918	0.925	0.	0.	0.	0.	0.	0.	0.	0.	0.	0.	0.	0.	0.
600	0.	0.	0.898	0.921	0.933	0.	0.	0.	0.	0.	0.	0.	0.	0.	0.	0.	0.
	0.	0.	0.	0.901	0.920	0.940	0.	0.	0.	0.	0.	0.	0.	0.	0.	0.	0.
	0.	0.	0.	0.852	0.908	0.930	0.945	0.	0.	0.	0.	0.	0.	0.	0.	0.	0.
	0.	0.	0.	0.	0.870	0.909	0.930	0.950	0.954	0.	0.	0.	0.	0.	0.	0.	0.
	0.	0.	0.	0.	0.	0.885	0.916	0.933	0.950	0.956	0.	0.	0.	0.	0.	0.	0.
700	0.	0.	0.	0.	0.	0.	0.886	0.920	0.939	0.952	0.956	0.	0.	0.	0.	0.	0.
	0.	0.	0.	0.	0.	0.	0.	0.886	0.921	0.941	0.954	0.962	0.	0.	0.	0.	0.
	0.	0.	0.	0.	0.	0.	0.	0.849	0.856	0.926	0.940	0.954	0.959	0.	0.	0.	0.
	0.	0.	0.	0.	0.	0.	0.	0.	0.842	0.898	0.924	0.944	0.955	0.957	0.	0.	0.
	0.	0.	0.	0.	0.	0.	0.	0.	0.	0.858	0.898	0.925	0.945	0.958	0.963	0.	0.
800	0.	0.	0.	0.	0.	0.	0.	0.	0.	0.	0.861	0.898	0.928	0.947	0.958	0.964	0.
	0.	0.	0.	0.	0.	0.	0.	0.	0.	0.	0.779	0.863	0.905	0.927	0.947	0.958	0.
	0.	0.	0.	0.	0.	0.	0.	0.	0.	0.	0.	0.797	0.865	0.904	0.930	0.946	0.
	0.	0.	0.	0.	0.	0.	0.	0.	0.	0.	0.	0.	0.812	0.865	0.900	0.931	0.
	0.	0.	0.	0.	0.	0.	0.	0.	0.	0.	0.	0.	0.	0.810	0.862	0.900	0.
900	0.	0.	0.	0.	0.	0.	0.	0.	0.	0.	0.	0.	0.	0.	0.815	0.871	0.
	0.	0.	0.	0.	0.	0.	0.	0.	0.	0.	0.	0.	0.	0.	0.	0.820	0.
	0.	0.	0.	0.	0.	0.	0.	0.	0.	0.	0.	0.	0.	0.	0.	0.726	0.
	0.	0.	0.	0.	0.	0.	0.	0.	0.	0.	0.	0.	0.	0.	0.	0.	0.
	0.	0.	0.	0.	0.	0.	0.	0.	0.	0.	0.	0.	0.	0.	0.	0.	0.
	0.	0.	0.	0.	0.	0.	0.	0.	0.	0.	0.	0.	0.	0.	0.	0.	0.
	0.	0.	0.	0.	0.	0.	0.	0.	0.	0.	0.	0.	0.	0.	0.	0.	0.

$m_{\pi\pi}$ ↓

RUN 1

	0.912	0.	0.	0.	0.	0.	0.	0.	0.	0.	0.	0.	0.	0.	0.	0.	0.
	0.917	0.929	0.	0.	0.	0.	0.	0.	0.	0.	0.	0.	0.	0.	0.	0.	0.
	0.	0.910	0.933	0.	0.	0.	0.	0.	0.	0.	0.	0.	0.	0.	0.	0.	0.
600	0.	0.	0.910	0.939	0.	0.	0.	0.	0.	0.	0.	0.	0.	0.	0.	0.	0.
	0.	0.	0.923	0.924	0.949	0.	0.	0.	0.	0.	0.	0.	0.	0.	0.	0.	0.
	0.	0.	0.	0.912	0.933	0.953	0.956	0.	0.	0.	0.	0.	0.	0.	0.	0.	0.
	0.	0.	0.	0.	0.915	0.938	0.954	0.960	0.	0.	0.	0.	0.	0.	0.	0.	0.
	0.	0.	0.	0.	0.	0.920	0.942	0.958	0.964	0.	0.	0.	0.	0.	0.	0.	0.
700	0.	0.	0.	0.	0.	0.905	0.923	0.945	0.959	0.965	0.	0.	0.	0.	0.	0.	0.
	0.	0.	0.	0.	0.	0.	0.889	0.925	0.949	0.963	0.965	0.	0.	0.	0.	0.	0.
	0.	0.	0.	0.	0.	0.	0.	0.897	0.930	0.951	0.962	0.967	0.	0.	0.	0.	0.
	0.	0.	0.	0.	0.	0.	0.	0.	0.894	0.935	0.953	0.962	0.971	0.	0.	0.	0.
	0.	0.	0.	0.	0.	0.	0.	0.	0.876	0.906	0.940	0.953	0.965	0.970	0.	0.	0.
800	0.	0.	0.	0.	0.	0.	0.	0.	0.	0.878	0.909	0.939	0.956	0.965	0.972	0.	0.
	0.	0.	0.	0.	0.	0.	0.	0.	0.	0.	0.874	0.914	0.941	0.956	0.967	0.971	0.
	0.	0.	0.	0.	0.	0.	0.	0.	0.	0.	0.	0.868	0.917	0.943	0.956	0.967	0.
	0.	0.	0.	0.	0.	0.	0.	0.	0.	0.	0.	0.815	0.873	0.924	0.943	0.957	0.
	0.	0.	0.	0.	0.	0.	0.	0.	0.	0.	0.	0.	0.848	0.886	0.920	0.943	0.
900	0.	0.	0.	0.	0.	0.	0.	0.	0.	0.	0.	0.	0.	0.831	0.882	0.921	0.
	0.	0.	0.	0.	0.	0.	0.	0.	0.	0.	0.	0.	0.	0.	0.839	0.888	0.
	0.	0.	0.	0.	0.	0.	0.	0.	0.	0.	0.	0.	0.	0.	0.805	0.837	0.
	0.	0.	0.	0.	0.	0.	0.	0.	0.	0.	0.	0.	0.	0.	0.	0.809	0.
	0.	0.	0.	0.	0.	0.	0.	0.	0.	0.	0.	0.	0.	0.	0.	0.	0.
	0.	0.	0.	0.	0.	0.	0.	0.	0.	0.	0.	0.	0.	0.	0.	0.	0.
	0.	0.	0.	0.	0.	0.	0.	0.	0.	0.	0.	0.	0.	0.	0.	0.	0.

$m_{\pi\pi}$ ↓

RUN 2

	0.	0.	0.	0.	0.	0.	0.	0.	0.	0.	0.	0.	0.	0.	0.	0.	0.
	0.929	0.	0.	0.	0.	0.	0.	0.	0.	0.	0.	0.	0.	0.	0.	0.	0.
	0.	0.943	0.	0.	0.	0.	0.	0.	0.	0.	0.	0.	0.	0.	0.	0.	0.
600	0.	0.	0.948	0.957	0.	0.	0.	0.	0.	0.	0.	0.	0.	0.	0.	0.	0.
	0.	0.	0.936	0.954	0.962	0.	0.	0.	0.	0.	0.	0.	0.	0.	0.	0.	0.
	0.	0.	0.	0.931	0.957	0.967	0.	0.	0.	0.	0.	0.	0.	0.	0.	0.	0.
	0.	0.	0.	0.	0.938	0.960	0.972	0.	0.	0.	0.	0.	0.	0.	0.	0.	0.
	0.	0.	0.	0.	0.915	0.947	0.963	0.973	0.	0.	0.	0.	0.	0.	0.	0.	0.
700	0.	0.	0.	0.	0.	0.916	0.952	0.965	0.974	0.975	0.	0.	0.	0.	0.	0.	0.
	0.	0.	0.	0.	0.	0.	0.925	0.953	0.967	0.975	0.978	0.	0.	0.	0.	0.	0.
	0.	0.	0.	0.	0.	0.	0.	0.934	0.958	0.969	0.976	0.981	0.	0.	0.	0.	0.
	0.	0.	0.	0.	0.	0.	0.	0.912	0.936	0.960	0.969	0.976	0.981	0.	0.	0.	0.
	0.	0.	0.	0.	0.	0.	0.	0.	0.914	0.942	0.960	0.970	0.978	0.981	0.	0.	0.
800	0.	0.	0.	0.	0.	0.	0.	0.	0.	0.910	0.946	0.963	0.972	0.977	0.982	0.	0.
	0.	0.	0.	0.	0.	0.	0.	0.	0.	0.	0.917	0.948	0.964	0.973	0.977	0.982	0.
	0.	0.	0.	0.	0.	0.	0.	0.	0.	0.	0.851	0.922	0.950	0.964	0.974	0.979	0.
	0.	0.	0.	0.	0.	0.	0.	0.	0.	0.	0.	0.872	0.925	0.950	0.965	0.974	0.
	0.	0.	0.	0.	0.	0.	0.	0.	0.	0.	0.	0.	0.887	0.930	0.952	0.964	0.
900	0.	0.	0.	0.	0.	0.	0.	0.	0.	0.	0.	0.	0.	0.890	0.933	0.953	0.
	0.	0.	0.	0.	0.	0.	0.	0.	0.	0.	0.	0.	0.	0.848	0.897	0.933	0.
	0.	0.	0.	0.	0.	0.	0.	0.	0.	0.	0.	0.	0.	0.	0.848	0.896	0.
	0.	0.	0.	0.	0.	0.	0.	0.	0.	0.	0.	0.	0.	0.	0.	0.844	0.
	0.	0.	0.	0.	0.	0.	0.	0.	0.	0.	0.	0.	0.	0.	0.	0.	0.
	0.	0.	0.	0.	0.	0.	0.	0.	0.	0.	0.	0.	0.	0.	0.	0.	0.
	0.	0.	0.	0.	0.	0.	0.	0.	0.	0.	0.	0.	0.	0.	0.	0.	0.

$m_{\pi\pi}$ ↓

1.0 1.2 1.4 k(BeV)

RUN 3

Cos θ_{cm} at which the ρ^0 Efficiency Peaked

TABLE VIII

Figure 27

This shows the bremsstrahlung spectrum obtained by folding the theoretical spectrum(42) with a 22 MeV resolution function.

The beam energy meter was at 1475 MeV during the experiment. The calibration of the beam energy meter

$$\frac{E_o(\text{true}) - E_o(\text{b. e. m.})}{E_o(\text{b. e. m.})} = +2.1\% \quad (52)$$

gives the value $E_o = 1504$ MeV which was used to calculate the theoretical spectrum above.

Figure 27

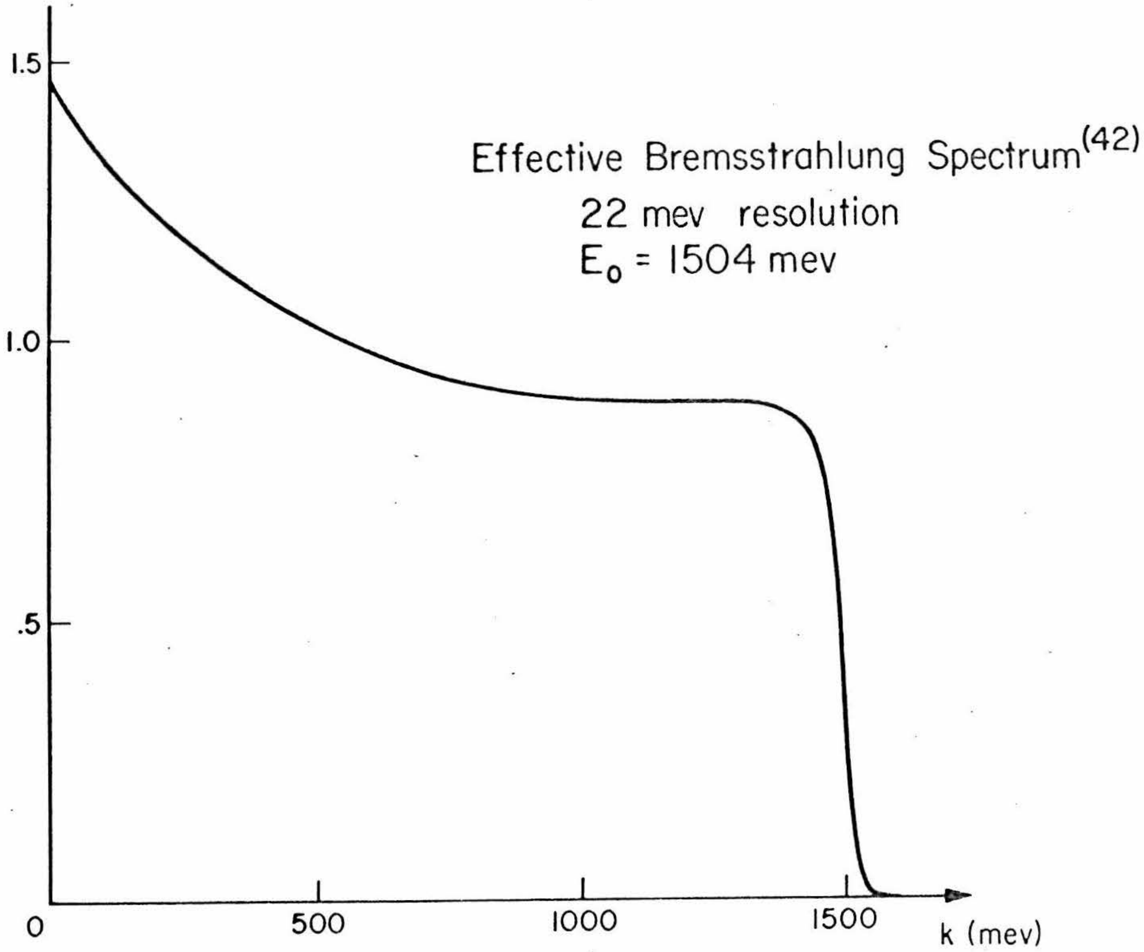
Effective Bremsstrahlung Spectrum(42)
22 mev resolution
E0 = 1504 mev
1.5
1.0
.5
0
500
1000
1500
k (mev)

SUMMARY OF SYMBOLS AND DEFINITIONS

F	overall χ^2 associated with an event.
Φ_k	individual track probability for particle k .
B	the change in the proton angle θ_p when solving the kinematic equation.
P_x(PULCHI)	the χ^2 fit between the proton range and the measured scope pulses.
E_T	the energy of the proton as it left the target wall.
D_k	the distance between the origin (x_o) and a straight line approximation to the track for particle k.
$\hat{x}_o$	the origin of the event inside the hydrogen target.
T_p	the initial proton kinetic energy.
$m_{\pi\pi}$	the invariant mass of the $\pi - \pi$ system.
σ	related to the measuring error (see p - 110).
$\hat{m}_{kj}$	the position of the j^{th} spark on track k.
MINSTØP	a lower limit on the proton range used in the preliminary scanning.
LD1	the electronic trigger produced by a proton stopping in HC1.
LD2	the electronic trigger produced by a proton stopping in HC2.
LD3	the electronic trigger produced by a proton stopping in HC3 or 4.
D1	the discrimination on proton pulses required for an LD1 trigger.
D2	the discrimination on proton pulses required for an LD2.

REFERENCES

1. V. Peterson and I. Henry, Phys. Rev. 96, 850 (1954).
2. M. Sands, M. Bloch, J. Teasdale and R. L. Walker, Phys. Rev. 99, 652 (1955).
3. V. Z. Peterson, Bull. Am. Phys. Soc. Series II 1, 173 (1956).
4. R. M. Griedman and K. M. Crowe, Phys. Rev. 105, 1369 (1957).
5. W. M. Woodward, R. R. Wilson, and P. D. Luckey, Bull. Am. Phys. Soc. Series II 2, 195 (1957).
6. M. Bloch and M. Sands, Phys. Rev. 108, 1101 (1957).
7. M. Bloch and M. Sands, Phys. Rev. 113, 305 (1959).
8. D. D. Elliott, Ph.D. Thesis, California Institute of Technology (1959).
9. J. M. Sellen, G. Cocconi, V. Cocconi, and E. Hart, Phys. Rev. 113, 1323 (1959).
10. B. M. Chasan, G. Cocconi, V. Cocconi, R. M. Schectman, and D. H. White, Phys. Rev. 119, 811 (1960).
11. J. R. Kilner, R. E. Diebold, and R. L. Walker, Phys. Rev. Letters 7, 518 (1960).
12. D. McLeod, S. Richert, and A. Silverman, Phys. Rev. Letters 7, 383 (1961).
13. N. P. Samios, A. H. Bachman, R. M. Lea, T. E. Kalogeropoulos, and W. D. Shephard, Phys. Rev. Letters 9, 139 (1962).

14. R. Del Fabbro, M. dePretis, R. Jones, G. Marini, A. Adian, G. Stoppini, and L. Tau, Phys. Rev. Letters 12, 674 (1964).

15. R. Del Fabbro, M. dePretis, R. Jones, G. Marini, A. Adian, G. Stoppini, and L. Tau, Phys. Rev. 139, B 701 (1965).

16. M. Beneventano, R. Finzi, L. Poaluzi, F. Sebastiani, M. Severi, and F. Villa, Nuovo Cimento 38, 1054 (1965).

17. H. R. Crouch, et al., "Proceedings of the International Symposium on Electron and Photon Interactions at High Energies, Vol. II", Hamburg (1965).

18. J. V. Allaby, H. L. Lynch, and D. M. Ritson, Phys. Rev. 142, 887 (1966).

19. U. Brall, et al., Nuovo Cimento 41, 270 (1966).

20. L. J. Fretwell and J. H. Mullins, Phys. Rev. 148, 1542 (1966).

21. M. G. Hauser and R. L. Walker, Phys. Rev. (to be published).

22. Cambridge Bubble Chamber Group, Phys. Rev. 146, 994 (1966).

23. U. Brall, et al., "Photoproduction of Meson and Baryon Resonances at Energies up to 5.8 BeV", DESY report 66/32, November 1966.

24. R. E. Cutkosky and F. Zachariasen, Phys. Rev. 103, 1108 (1956).

25. A. R. Erwin, R. March, W. D. Walker, and E. West, Phys. Rev. Letters 6, 628 (1961).

26. S. D. Drell, Phys. Rev. 110, 1212 (1958).

27. P. Stichel and M. Scholz, Nuovo Cimento 34, 1381 (1964).

28. E. Ferrari and F. Selleri, Suppl. Nuovo Cimento 24, 453 (1962).

29. S. M. Berman and S. D. Drell, Phys. Rev. 133 B 791 (1964).

30. U. Moar and P. C. M. Yock, Phys. Rev. 148, 1542 (1966).

31. F. Selleri, Phys. Letters 3, 76 (1962).

32. K. Gottfried and J. D. Jackson, Nuovo Cimento 34, 735 (1964).

33. L. Durand and Y. T. Chiu, Phys. Rev. Letters 12, 399 (1964).

34. D. Amati, A. Stanghellini and S. Fubini, Nuovo Cimento 26, 896 (1962).

35. D. Amati, A. Stanghellini, S. Fubini, and M. Tonin, Nuovo Cimento 22, 569 (1961).

36. C. Clinesmith, Ph.D. Thesis, California Institute of Technology (1967).

37. E. D. Bloom, Ph.D. Thesis, California Institute of Technology (1967).

38. C. Y. Prescott, Ph.D. Thesis, California Institute of Technology (1966).

39. W. C. Davidon, ANL-5900 Rev. (1959), unpublished.

40. S. B. Triman and C. N. Yang, Phys. Rev. Letters **8**, 140 (1962).

41. J. D. Jackson, Nuovo Cimento **34**, 1644 (1964).

42. F. B. Wolverton, "Thick Radiator Bremsstrahlung. Angular Dependence of the Spectrum for Electron Energies Greater than 300 MeV", unpublished (1966).

43. J. G. Asbury, et al., DESY report.

44. Lanzerotti, et al., Phys. Rev. Letters **15**, 210 (1965).

45. B. Rossi, *High Energy Particles* (Prentice-Hall, Inc., New York, 1952), p. 22-37.

46. R. M. Sternheimer, Phys. Rev. **118**, 1045 (1960).

47. D. E. Groom and M. G. Hauser, Nucl Inst. and Methods **46**, 301 (1967).

48. M. G. Hauser, "YNT/A Polynomial Interpolation Routine". This program is in the Synchrotron Program Library.

49. A. H. Rosenfeld, A. Barbaro-Galtieri, J. King, W. J. Podolski, M. Roos, W. J. Willis, C. G. Wohl, UCRL **8030**, (August 1966).

50. M. Ross and L. Stodolsky, Phys. Rev. **149**, 1172 (1966).

51. J. D. Jackson and H. Pilkuhn, Nuovo Cimento **33**, 906 (1964).

52. H. A. Thiessen, "A Recalibration of the Beam Energy Meter", CTSL Internal Report No. 21, unpublished (1966).